# EFFECT OF SURFACE ROUGHNESS IN MICROCHANNELS ON HEAT TRANSFER

A THESIS SUBMITTED TO
THE GRADUATE SCHOOL OF NATURAL AND APPLIED SCIENCES
OF
MIDDLE EAST TECHNICAL UNIVERSITY

BY

METİN BİLGEHAN TURGAY

IN PARTIAL FULFILLMENT OF THE REQUIREMENTS
FOR
THE DEGREE OF MASTER OF SCIENCE
IN
MECHANICAL ENGINEERING

DECEMBER 2008

Approval of the thesis:

**EFFECT OF SURFACE ROUGHNESS IN MICROCHANNELS ON HEAT TRANSFER**

submitted by **METİN BİLGEHAN TURGAY** in partial fulfillment of the requirements for the degree of **Master of Science in Mechanical Engineering Department, Middle East Technical University** by,

Prof. Dr. Canan Özgen _____
Dean, Graduate School of **Natural and Applied Sciences**

Prof. Dr. Süha Oral _____
Head of Department, **Mechanical Engineering**

Asst. Prof. Dr. Almıla Güvenç Yazıcıoğlu _____
Supervisor, **Mechanical Engineering Dept., METU**

Prof. Dr. Sadık Kakaç _____
Co-Supervisor, **Mechanical Engineering Dept., TOBB-ETU**

**Examining Committee Members:**

Assoc. Prof. Dr. Cemil Yamalı _____
Mechanical Engineering Dept., METU

Asst. Prof. Dr. Almıla Güvenç Yazıcıoğlu _____
Mechanical Engineering Dept., METU

Prof. Dr. Sadık Kakaç _____
Mechanical Engineering Dept., TOBB-ETU

Asst. Prof. Dr. Merve Erdal Erdoğmuş _____
Mechanical Engineering Dept., METU

Asst. Prof. Dr. Cüneyt Sert _____
Mechanical Engineering Dept., METU

**Date:** 01.12.2008

**I hereby declare that all information in this document has been obtained and presented in accordance with academic rules and ethical conduct. I also declare that, as required by these rules and conduct, I have fully cited and referenced all material and results that are not original to this work.**

Name, Last Name : Metin Bilgehan TURGAY

Signature :

## ABSTRACT

EFFECT OF SURFACE ROUGHNESS IN MICROCHANNELS ON HEAT TRANSFER

Turgay, Metin Bilgehan

M.Sc., Department of Mechanical Engineering

Supervisor : Asst. Prof. Dr. Almıla Güvenç Yazıcıoğlu

Co-Supervisor : Prof. Dr. Sadık Kakaç

December 2008, 118 pages

In this study, effect of surface roughness on convective heat transfer and fluid flow in two dimensional parallel plate microchannels is analyzed by numerically. For this purpose, single-phase, developing, laminar fluid flow at steady state and in the slip flow regime is considered. The continuity, momentum, and energy equations for Newtonian fluids are solved numerically for constant wall temperature boundary condition. Slip velocity and temperature jump at wall boundaries are imposed to observe the rarefaction effect. Effect of axial conduction inside the fluid and viscous dissipation also considered separately. Roughness elements on the surfaces are simulated by triangular geometrical obstructions. Then, the effect of these roughness elements on the velocity field and Nusselt number are compared to the results obtained from the analyses of flows in microchannels with smooth surfaces. It is found that increasing surface roughness reduces the heat transfer at continuum conditions. However in slip flow

regime, increase in Nusselt number with increasing roughness height is observed. Moreover, this increase is found to be more obvious at low rarefied flows. It is also found that presence of axial conduction and viscous dissipation has increasing effect on heat transfer in smooth and rough channels.

Key words: microchannel, slip flow, temperature jump, surface roughness, heat transfer.

# ÖZ

MİKROKANALLARDA YÜZEY PÜRÜZLÜLÜĞÜNÜN ISI TRANSFERİNE ETKİSİ

Turgay, Metin Bilgehan

Yüksek Lisans, Makine Mühendisliği Bölümü

Tez Yöneticisi : Asst. Prof. Dr. Almıla Güvenç Yazıcıoğlu

Ortak Tez Yöneticisi : Prof. Dr. Sadık Kakaç

Aralık 2008, 118 sayfa

Bu çalışmada, iki boyutlu parallel plakalardan oluşan mikrokanallardaki yüzey pürüzlülüğünün konveksiyonla ısı transferine ve akışa etkisi numerik olarak incelenmiştirtir. Bunun için tek fazlı, ısıl ve hidrodinamik olarak gelişmekte olan kararlı rejimdeki kaygan akış ele alınmıştır. Newtonien akışkanlar için süreklilik, momentum ve enerji denklemleri sabit duvar sıcaklığı sınır şartı için numerik olarak çözülmüştür. Seyrelme etkisini incelemek için duvardaki hız kayması ve sıcaklık sıçraması göz önüne alınmıştır. Ayrıca akışkan içindeki eksenel ısı iletimi ve sürtünme kaybı da değerlendirilmiştir. Yüzey pürüzlülüğü üçgen geometrik elemanlar olarak simüle edilmiştir. Daha sonra pürüzlü kanal için elde edilen hız profili ve Nusselt sayıları, pürüzsüz kanal için elde edilen değerlerle karşılaştırılmıştır. Süreklilik şartlarında yüzey pürüzlülüğündeki artışın ısı tranferini azalttığı bulunmuştur. Fakat, kaygan akış şartlarında yüzey pürüzlülüğündeki artışın Nusselt sayısını da arttırdığı gözlemlenmiştir. Bu artışın az seyrelmiş akışlarde daha fazla olduğu saptanmıştır. Ayrıca, eksenel ısı

iletiminin ve sürtünme ısınmasının, pürüzlü kanallarda da düzgün yüzeyli kanallarda da ısı transferini arttırıcı etkisi olduğu bulunmuştur.

Anahtar Kelimeler: mikrokanallar, kaygan akış, sıcaklık sıçraması, yüzey pürüzlülüğü, ısı transferi.

*for my father and my family...*

## ACKNOWLEDGEMENTS

First of all, I would like to thank to my supervisor, Asst. Prof. Dr. Almıla G. Yazıcıoğlu, for her guidance, patience, trust and encouragement. I also would like to thank to my co-supervisor, Prof. Dr. Sadık Kakaç for introducing me to this area of science and opportunities. Working with my supervisor and co-supervisor is priceless and enjoyable.

I would like to thank to Asst. Prof. Dr. Cüneyt Sert for his contributions and valuable ideas during preparing the numerical code.

I also would like to thank my colleagues Başar Bulut, Barbaros Çetin, and Murat Barışık, for their support, help and friendship.

Finally, my family and my relatives, there is not any word that I can explain how I can thank to them and how I am grateful to being a part of this family. I hope they will understand.

## TABLE OF CONTENTS

## LIST OF TABLES

## LIST OF FIGURES

## NOMENCLATURE

| | |
|---|---|
| $Br$ | Brinkman number, $Br = \mu U_m / k\,(T_i - T_w)$ |
| $c_p$ | constant pressure specific heat, J/kgK |
| $D_h$ | hydraulic diameter |
| $e$ | average height of the roughness elements |
| $F_M$ | tangential momentum accommodation coefficient |
| $F_T$ | thermal accommodation coefficient |
| $H$ | channel height, m |
| $h$ | convective heat transfer coefficient |
| $k$ | thermal conductivity, W/mK |
| $Kn$ | Knudsen number, $Kn = \lambda / L_c$ |
| $L$ | length of channel, m |
| $L_c$ | characteristic length, m |
| $Ma$ | Mach number |
| $Nu$ | Nusselt number |
| $p$ | pressure, kPa |
| $Pe$ | Peclet number, $Pe = Re \cdot Pr$ |
| $Pr$ | Prandtl number, $Pr = \vartheta / \alpha$ |

| | |
|---|---|
| $R$ | gas constant, J/kgK |
| $Re$ | Reynolds number, $Re = (U_c L_c) / \vartheta$ |
| $T$ | temperature, K |
| $u$ | velocity in axial direction, m/s |
| $U_c$ | characteristic fluid velocity |
| $u_s$ | slip velocity, m/s |
| $v$ | velocity in vertical direction, m/s |
| $x$ | axial coordinate |
| $y$ | vertical coordinate |

Greek Symbols

| | |
|---|---|
| $\alpha$ | thermal diffusivity, $m^2/s$ |
| $\gamma$ | specific heat ratio |
| $\varepsilon$ | relative roughness of surface, $\varepsilon = e / D_h$ |
| $\varepsilon_p$ | penalty parameter |
| $\theta$ | dimensionless temperature |
| $\lambda$ | mean free path, m |
| $\mu$ | dynamic viscosity, kg/ms |
| $\rho$ | density, $kg/m^3$ |
| $\vartheta$ | kinematic viscosity, $kg/m^3$ |
| $\psi$ | shape (approximation) function |

Subscripts

| | |
|---|---|
| *Av* | Average values |
| *i* | inlet values |
| *m* | mean values |
| *s* | fluid properties at the surface |
| *w* | wall values |
| *x* | local values |

# CHAPTER 1

# INTRODUCTION

With the rapid development of micro and nano fabrication in the last two decades, devices in micro- ($1x10^{-6}$ m) and nano- ($1x10^{-9}$ m) scale, which can be named as MEMS (Microelectromechanical Systems), NEMS (Nanoelectromechanical Systems), MFD (Micro flow devices), etc., became very popular for scientists, researchers, engineers, and various industrial companies. As a result, micro devices and systems such as micro actuators, micro motors, micro heat sinks, micro heat exchangers, micro pumps, lab-on-a-chip devices, micro total analysis systems (μTAS), micro propulsion devices, micro reactors, micro gears, micro valves, and micro sensors have been fabricated and used successfully [1].

Most of these micro devices and systems include fluid flow and heat transfer in micro-scale, which is an open and new field in scientific literature. This new and intriguing area of science and engineering brought very important advantages and developments, such as high efficiency in production, low costs per samples, very small dimensions of the resulting product, which improves portability and transport, much better accuracy and reliability, and in heat transfer area, increased convective and radiative heat transfer rates due to high surface area to volume ratios of heat sinks or heat exchangers. This development also brought its own unique problems, such as deviations from well known conventional theories.

Studies in micro flow started with Poiseuille, in 1846. He investigated the liquid flow in tubes with diameters ranging from 30 μm to 150 μm. Then, in 1909, Knudsen studied the rarefied gas flow in glass capillary tubes in transition and free molecular flow regimes [2]. Since then, various scientists performed research in this field and tried to understand the fundamentals of the micro-scale. Famous scientist Dr. Richard P. Feynman delivered two lectures in this area [3]. The first was in 1959 at the annual meeting of the American Physical Society, and named *"There's Plenty of Room at the Bottom: An Invitation to Enter a New Field of Physics"* [4]. In this lecture, he proposed a vision of miniaturization. The second lecture was in 1983 at the Jet Propulsion Laboratory, and named *"Infinitesimal Machinery"* [5], in which he revisited his first lecture and anticipated some of today's micro technologies [1, 2]. These two lectures were accepted as a touchstone in micro engineering.

With the developing technology, many micro-scale devices became available for scientists, in late 1980s and early 1990s. Since then, experiments have been conducted systematically to better understand the flow and heat transfer behavior in micro-scale. It was seen from the experimental data that conventional continuum approach is not always valid in micro-scale, i.e., friction factors, Nusselt numbers, Poiseuille numbers differ from classical values, and early transition from laminar to turbulent flow can be observed. These differences were mainly addressed by the rarefaction effect. Furthermore, additional factors that can be negligible in macro gas flows, such as compressibility, viscous dissipation, and thermal creep become important in gas micro flows, due to extremely small dimensions. However, when the fluid is liquid, wetting of the solid boundaries, adsorption and electrokinetic effects near the solid-fluid interface become very important as well [2].

In the macro world, the fluid is treated as a continuum (infinitely divisible substance). Related problems are solved using conservation of mass, momentum,

and energy equations with appropriate boundary conditions, which lead to a set of nonlinear partial differential equations called Navier-Stokes equations. The boundary conditions are mostly the "no-slip", in which the velocity of the fluid molecules adjacent to the solid boundary is equal to zero, and the "no-temperature jump", in which the temperature of the fluid molecules adjacent to the solid boundary is equal to the temperature to the solid boundary [6]. Also, in macro flow systems, flow regimes are mostly characterized by Reynolds number, Re, defined as

$$Re = \frac{U_c L_c}{\vartheta} \tag{1.1}$$

where $U_c$ is the characteristic fluid velocity, $L_c$ is the characteristic length, and $\vartheta$ is kinematic viscosity.

However, continuum model fails as the characteristic length becomes comparable to the mean free path, $\lambda$, which is defined as the average distance traveled by the molecules without colliding with each other. This should be the case if the gas is at very low pressure (rarefied) or the characteristic length is very small as in micro- or nanochannels [7]. The ratio of the mean free path to the characteristic length, gives an important non-dimensional parameter known as the Knudsen number, *Kn*, which is a measure of the rarefaction,

$$Kn = \frac{\lambda}{L_c} \tag{1.2}$$

Also, the relationship between *Kn*, *Re* and Mach (*Ma*) numbers is given as,

$$Kn = \sqrt{\frac{\gamma\pi}{2}}\frac{Ma}{Re} \tag{1.3}$$

where $\gamma$ is specific heat ratio of the fluid. In micro flow systems, flow regimes are characterized by the Knudsen number. Most commonly, when Knudsen number is

below 0.001, flow is considered as continuum and the Navier-Stokes and energy equations are valid with no-slip and no-temperature jump boundary conditions. When Knudsen number is between 0.001 and 0.1, flow is considered as in slip-flow regime. From Knudsen 0.1 to 10 is the transition regime and above 10, flow becomes free molecular. This classification is shown in Figure (1.1) graphically. It should be noted that, this classification is not solid; it is based on empirical data and regime limits may depend on the problem geometry [2].

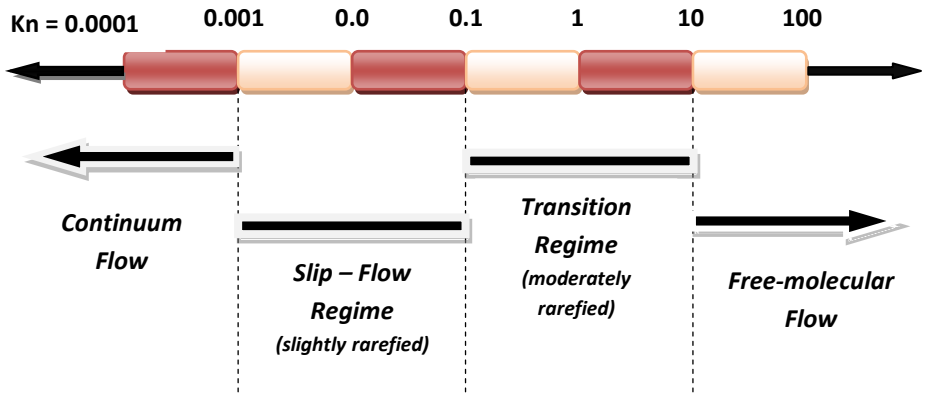


Figure 1.1: Knudsen number regimes.

Slip-flow regime is important in micro-scale gas flows, because most micro fluidic devices operate in this regime. In slip-flow regime, the continuum based Navier-Stokes and energy equations are still valid with appropriate boundary conditions at the solid boundaries, which are tangential velocity slip and temperature jump boundary conditions. One of the most commonly used pair of slip/jump boundary conditions is the Maxwellian boundary conditions, which are first order in accuracy. The tangential velocity slip boundary condition is given as,

$$u_s = \frac{2 - F_M}{F_M} \lambda \left(\frac{\partial u}{\partial n}\right)_w + 3\sqrt{\frac{RT}{8\pi}} \frac{\lambda}{T} \left(\frac{\partial T}{\partial n}\right)_w \tag{1.3}$$

and the temperature jump boundary condition is given as,

$$T_s - T_w = \frac{2 - F_T}{F_T} \frac{2\gamma}{\gamma + 1} \frac{\lambda}{Pr} \left(\frac{\partial T}{\partial n}\right)_w \tag{1.4}$$

In these equations, $F_M$ is the tangential momentum accommodation coefficient, $F_T$ is the thermal accommodation coefficient, $R$ is the gas constant, $Pr$ is the gas Prandtl number, $\gamma$ is the ratio of the specific heats, $n$ is the coordinate normal to the wall [1, 7]. Additional slip boundary conditions such as, second and higher order accurate ones, can be found in Ref. [2]. The second term on the right hand side of Eq. (1.3) reflects the thermal creep effect, which is the fluid flow induced by the temperature gradient along the channel.

The momentum accommodation coefficient $F_M$ represents the fraction of the molecules undergoing diffuse reflection. It is equal to zero for ideally smooth surfaces, where specular reflection occurs and molecules conserve their tangential momentum. It is equal to one for diffuse reflection where the tangential momentum is lost at the wall. It depends on fluid, solid and surface roughness of the channel. Experimental results show that its value is between 0.5 and 1.0, and in most of the engineering applications it is close to 1.0. Meanwhile, the thermal accommodation coefficient $F_T$ represents the fraction of the molecules reflected diffusively by the wall and accommodated their energy to the wall temperature. Its value varies between 0 and 1.0 [6].

When the gas micro flow is in slip-flow and early transition regime, continuum based solution methods are sufficient, that is governing Navier-Stokes and energy equations are solved with slip and jump boundary conditions, using one of the numerical methods such as finite element, finite volume, or finite difference,

when analytical solution is not possible. However when the flow is in late transition or free-molecular regime, an atomistic solution method, such as direct simulation Monte Carlo (DSMC), Boltzmann, Lattice Boltzmann, is required. When it comes to liquid micro flows, solution method mostly depends on the dimensions of the system. In mesoscopic scales, continuum approach with no-slip boundary condition suffices. However, in submicron dimensions, an atomistic solution method like molecular dynamics (MD), lattice Boltzmann, dissipative particle dynamics, is required [1, 2]. These conditions are summarized in Table (1.1).

Table 1.1: Summary of flow regimes and solution methods [1, 5].

| ***Regime*** | ***Solution Method*** | ***Kn Range*** |
|---|---|---|
| *Continuum* | Navier-Stokes and energy equations with no-slip / no-jump boundary conditions | $Kn < 0.001$ |
| *Slip – Flow* | Navier-Stokes and energy equations with slip / jump boundary conditions, (MD, DSMC… may be used for liquids) | $0.001 \leq Kn < 0.1$ |
| *Transition* | BTE (Boltzmann transport equation), DSMC | $0.1 \leq Kn < 10$ |
| *Free molecular* | BTE, DSMC | $Kn \geq 10$ |

As stated before, experiments conducted in micro fluidic systems give different results than similar experiments conducted in macro size systems. These

differences are the results of neglected parameters and conditions described above. It is also possible that, some discrepancies belong to the experimental measurement uncertainties and other errors which might be expected when dealing with such small scales. In all circumstances, these anomalies between the results show the insufficient fundamental understanding and knowledge in this area. One of the problems faced in the understanding of these phenomena is the effect of the surface conditions of the microchannels, more specifically the surface roughness effect.

Roughness characteristics of microchannels are strictly dependent on the manufacturing processes of these channels. Manufacturing methods can be classified as micromechanical machining, X-ray micromachining, surface and surface-proximity-micromachining, and photolithographic-based processes [8]. Since the photolithographic process is the most common method, there are several experiments in open literature conducted with such microchannels. These are mostly related to the silicon wafers that are widely used in micro systems such as in electronics as semiconductors. When the chemical (wet) etching is applied on the silicon substrate by using a KOH solution, specific cross-sectional shapes are obtained. These cross-sectional shapes of the microchannels depend on the crystallographic morphology of the silicon used. These are rectangular on <110> silicon, trapezoidal with an apex angle of 54.74° on <100> silicon, and triangular on <111> silicon, where the numbers between the "<…>" sign show the Miller indices of silicon morphology. In photolithographic process, surface roughness depends on the crystallographic morphology of the silicon used, the concentration and temperature of the etching solution, and the duration that the solution is applied. For example, when a silicon micro channel with trapezoidal cross-section is obtained by wet etching, it has smooth lateral faces while the base face has randomly distributed roughness elements that look like conical or triangular prism obstructions, which can be seen in Fig. (1.2). However, when the process is continued, the channel has a triangular cross-section.

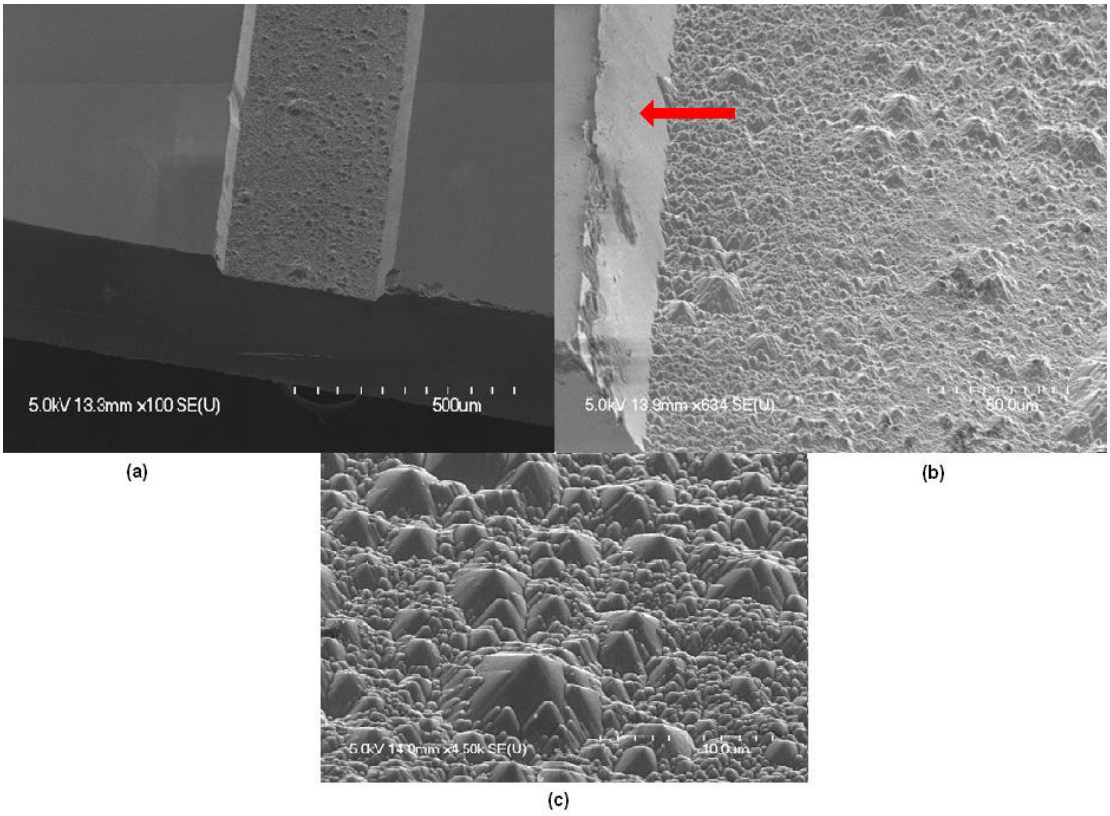


Figure 1.2: Scanning electron microscopy images of a silicon trapezoidal microchannel produced by photolithography (a) channel at a distance (b) smooth sidewall (c) closer look at roughness elements at base [69].

Defining the roughness characteristics in micro-scale is very difficult. Its extremely small size and random distribution of peaks along the surface make the investigation of roughness effect very difficult among the other parameters. Thus, most of the investigators neglect this effect in their studies. Furthermore, when an unexpected deviation occurs, most researchers refer to the roughness effect, whether it is true or not. During the last decade, special attention has been paid to this effect due to its somewhat mystic and unresolved nature. However, there are still a limited numbers of publications, relative to other effects, in open literature.

This study focuses on the effect of roughness on convective heat transfer and fluid flow in microchannels with uniform inlet fluid velocity and constant wall temperature boundary condition. For this purpose, single-phase, incompressible, laminar and constant property fluid flows, at steady state and in the slip-flow regime, in parallel plate channel, is considered. Roughness effect is simulated by adding triangular obstructions along the channel wall. Since the flow is in slip-flow regime, the Navier-Stokes and energy equations are solved numerically by imposing the velocity slip and temperature jump to boundary conditions. Also, since the fluid is assumed to have constant thermo-physical properties, Navier-Stokes and energy equations can be decoupled. Therefore, Navier-Stokes equations are first solved along the channel, and then the velocities found are used in the energy equation to obtain the temperature profile and local Nusselt numbers along the channel. Numerical calculations are carried out both by taking the axial conduction and the viscous dissipation effects into account, and by neglecting their effects. Reduced integration penalty finite element method is chosen as the numerical method and the computer code is written in MATLAB by the author. The written code is verified by comparing the results obtained from analytical solutions for simplified smooth channel cases.

In Chapter 2, review of the studies about micro-scale heat transfer and fluid flow in literature is given. Single phase flow and convective heat transfer in microchannels, especially with surface roughness, is considered. In Chapter 3, the case problem in is defined and governing equations are given. Then, numerical method, formulation, and solution procedure are described. Mesh convergence studies and results for both smooth and rough cases are given in Chapter 4 with a discussion. Then, the study is concluded with a summary and conclusion which forms Chapter 5. Also, further possible developments about this area are suggested in this chapter.

# CHAPTER 2

# LITERATURE SURVEY

Parallel to the technological development in micro engineering, especially in micro machining and construction, scientific research in the micro scale flow and heat transfer area has increased in last two decades. Thus, numerous studies have been conducted to understand the fundamentals; such as flow characteristics and heat transfer rates in simple geometries, as well as specific effects like rarefaction, viscous dissipation, channel geometries, electrokinetic effects, and surface roughness, and published in open literature. However, in this chapter, studies on single-phase flow and convective heat transfer in microchannels are reviewed. In particular, special interest is given to studies dealing with surface roughness effect, and they are taken into consideration in more detail.

Yener et al. [9] described the fundamentals of single-phase forced convection in microchannels and presented an extensive review in this area. Bayazitoglu and Kakac [10] explained the flow regimes of single phase gaseous fluid flows in microchannels with different cross-sections, by giving the theoretical base and reviewing the analytical, experimental, and numerical studies. Bayazitoglu et al. [11] reviewed some analytical solutions of temperature distribution and leading *Nu* values of gaseous slip-flows in microchannels for different geometries. The reader is encouraged to refer to these reviews to construct a basic knowledge about micro scale flow and heat transfer phenomena.

Obot [12] reviewed the experimental results on pressure drop, heat and mass transfer studies, and laminar to turbulent transition of single phase flows, up to year 1998. The causes of inconsistencies in the results have been mostly related to the measurement errors by the author. Also, Sobhan and Garimella [13] reviewed the experimental results and theoretical predictions of fluid flow and heat transfer studies in micro- and mini-channels and microtubes, up to year 2000. They also presented them in tabular form and compared the single phase friction factor and *Nu* correlations with the correlations of conventional size channels. The authors stated that there is little agreement between the results of each investigator. The possible reasons of deviations are referred to entrance and exit effects, surface roughness, which is generally not considered, and uncertainties and errors in experimental setups and measurements. Both Refs. [12] and [13] stated the need for additional systematic studies with carefully chosen and measured parameters.

Morini [8] reviewed the experimental studies on single phase convective heat transfer through microchannels chronologically, and tabulated and analyzed the results obtained for friction factor, laminar to turbulent transition, and *Nu* values. The author also stated that the results obtained from experiments deviate from conventional theories and are inconsistent with each other. The inconsistency in the experimental correlations for *Nu* for gas and liquid flows was shown graphically as well by the author in their work. These deviations are caused by rarefaction, compressibility, viscous dissipation, property variations, electro-osmotic effects, surface conditions of microchannels, and experimental uncertainties. Furthermore, the author also stated that the deviations are decreasing as the reliability and accuracy of the experimental and measurement devices increase with the improvement in micro technology, but also expressed the need of further studies for fundamental understanding of micro flows and heat transfer.

More recently, Hestroni et al. [14] reviewed the experimental studies of laminar incompressible flows in microchannels with circular, rectangular, triangular, and trapezoidal cross-sections, and having hydraulic diameters from 1.01 μm to 4010 μm. The authors compared the experimental data on pressure drop, Poiseuille number, friction factor, laminar to turbulent transition, and the effect of the viscous energy dissipation on flow parameters, of the flows in $0.001 \leq Re \leq Re_{cr}$ and $0.001 \leq Re \leq 0.4$ region. In a subsequent study, Hestroni et al. [15] reviewed the experimental and theoretical studies of single phase heat transfer in circular, triangular, rectangular, and trapezoidal microchannels with hydraulic diameters of 60 to 2000 μm. This time, the authors compared the experimental data on the effects of energy dissipation, axial conduction in the fluid and wall, geometrical properties and surface conditions of microchannels on heat transfer, to conventional theories.

From all these reviews, several conflicting conclusions can be drawn. Some investigators reported laminar fully developed friction factors and Poiseuille numbers lower than the conventional values, some reported higher values, while some investigators reported agreement with conventional values. A similar conflict occurs in laminar to turbulent transition *Re* values. Reported *Re* values vary between 300 and 6000. Similar conclusions can be made about the laminar regime *Nu* and the effect of energy dissipation on heat transfer. However, it should also be noted that, as the precision and reliability of the experimental setups and measurement devices increase, the deviation margin of theoretical and experimental results obtained from similar experiments conducted by different investigators reduces. Nevertheless, as pointed out in Refs. [8-15], future research is still needed for fundamental understanding.

Kavehpour et al. [16] investigated the effects of rarefaction and compressibility on the heat transfer and fluid flow characteristics in the entrance and fully developed regions for both uniform wall temperature and uniform wall heat flux thermal

boundary conditions. For this purpose the authors modeled a 2-D flow through a parallel plate in the slip-flow regime, $0.001< Kn <0.1$, and then solved the compressible form of conservation of momentum and energy equations, and the equation of state for an ideal gas, by imposing slip velocity and temperature jump into the boundary conditions. After non-dimensionalization, they used a numerical method based on control volume finite difference scheme (SIMPLE algorithm, power law scheme) to solve the equations. They compared their results with the continuum flows and found that *Nu* and friction coefficients were decreased. Furthermore, they showed that the compressibility effect is important for flows with higher *Re*, and the rarefaction effect is important for flows with lower *Re*. The entrance region was found to be longer for higher *Kn* values, the velocity and the temperature profile became flattened, and the axial pressure variation became nonlinear, compared to continuum flows.

Hadjiconstantinou and Simek [17, 18] investigated the convective heat transfer characteristics of a hydrodynamically and thermally fully developed gaseous flow, between micro- and nano-scale parallel plates and in circular tubes, under the constant wall temperature boundary condition. The authors used the slip flow theory, with axial conduction, to calculate the *Nu* in the $0 \leq Kn \leq 0.2$ range, and the DSMC method in the $0.02 < Kn < 2$ range. Results were obtained for different *Kn*, *Pe*, and thermal accommodation coefficients. They found that the axial heat conduction increased the *Nu* in the slip-flow regime. However, the effect of axial conduction decreased as the *Kn* increased. They also found that the *Nu* decreased with increasing *Kn*.

Aydın and Avcı [19] investigated the effect of *Br* and *Kn* values on *Nu* by solving the energy equation, analytically. For this purpose the authors considered a steady, hydrodynamically and thermally fully developed, laminar flow of a Newtonian fluid with constant properties, flowing in a parallel plate microchannel. Unlike Refs. [17, 18], they included viscous dissipation, but neglected axial conduction,

since *Pe* was large enough to neglect the axial conduction. They conducted their analysis for constant wall temperature and constant heat flux thermal boundary conditions separately, by imposing slip velocity and temperature jump effects at the wall. They observed singularities at the *Br* for each *Kn*, which was explained as the points where the heat supplied to the fluid is balanced with internal heat generation due to viscous heating. Similar to Refs. [17, 18], they found that as *Kn* increases, *Nu* decreases due to the increase in the temperature jump at the wall.

Asako et al. [20] investigated the compressibility effect on gaseous flows in parallel plate microchannels. For this purpose, they modeled a two dimensional compressible steady flow of an ideal gas. Then, they solved the compressible form of momentum equations with uniform inlet velocity and no-slip boundary condition, and the energy equation by neglecting the heat conduction terms. After non-dimensionalization, they solved the equations numerically, in which the numerical methodology was based on the arbitrary-Lagrangian-Eulerian (ALE) method. They also obtained correlations for Darcy's and Fanning's friction factors, $f_d$ and $f_f$ respectively, which are functions of *Re* and Mach number. They found that $(f \cdot Re)$ is a function of Mach number and different from incompressible flow values for the parallel plate channel. Also the effect of stagnation pressure and temperature on $(f \cdot Re)$ is found to be small.

Jeong and Jeong [21] solved the Graetz problem, which is hydrodynamically developed at the entrance and thermally developing, in a parallel plate microchannel with uniform temperature and uniform heat flux boundary conditions, analytically. The authors included the rarefaction effects, which are slip velocity and temperature jump on the channel wall, axial conduction in the fluid, and viscous dissipation into their analysis. They solved the governing energy equation for various *Kn* and *Br* values, and for air as the working fluid, with the method of separation-of-variables, and used the eigenfunction series expansion for the temperature distribution. They found that *Nu* decreases as *Kn* or

*Br* increases and as *Pe* decreases. They also stated that, similar to Refs. [17, 18], which are hydrodynamically and thermally fully developed flow analyses, axial conduction increases the *Nu* compared to the solutions of Graetz problem without axial conduction.

Tunc and Bayazitoglu [22] solved the same problem for microtubes analytically by using integral transform technique. They considered the fluid properties constant, included viscous dissipation, and also took the temperature jump and velocity slip at the wall into account. They analyzed both the uniform temperature and uniform heat flux boundary condition cases. The effect of viscous dissipation was studied for fluid heating and cooling, both. They showed the variation of *Nu* with *Kn*, *Pr*, and *Br*, and presented their results in tabular form for $0.6 \leq Pr \leq 1.0$, $0.0 \leq Kn \leq 0.12$, and $Br = 0.0, \pm 0.01$.

Larrodé et al. [23] also studied the Graetz problem, which is extended to the slip-flow region, to define the effect of rarefaction on heat transfer in microtubes. They solved the energy equation considering temperature jump and velocity slip at the wall. By introducing a spatial rescaling factor, slip radius, which is a function of *Kn* and momentum accommodation factor, they reduced the slip-flow Graetz problem to a classical Graetz problem with a mixed boundary condition. They developed a uniform asymptotic approximation for the solution of the eigenfunction of the problem. They found that heat transfer is decreased when they considered the temperature jump compared to the continuum case.

Cetin et al. [24] studied a two-dimensional, incompressible, constant property, hydrodynamically developed, thermally developing, single-phase laminar flow in microtubes and microchannels, and in the slip-flow regime at steady state. The authors neglected the axial conduction in the fluid, but included viscous dissipation and velocity slip and temperature jump conditions at the walls, into their analysis. They solved the energy equation for constant wall temperature and constant wall heat flux boundary conditions, numerically. They used a finite

difference scheme as the numerical method, and a fine mesh in their simulations. They verified the numerical method by comparing it with the continuum flow simulation results. They found that for the constant wall temperature case, *Nu* decreases as the *Kn* increases, as a result of increasing temperature jump, which reduces the heat transfer when *Br* is greater than zero. Also, *Nu* had greater values in the presence of viscous heating, compared to otherwise.

In a subsequent study, Cetin et al. [25] solved the same Graetz problem in slip-flow regime by considering the axial conduction, viscous dissipation, and rarefaction effects, for uniform wall temperature boundary condition in a microtube. They used a coordinate transformation for the energy equation and then solved it numerically by a finite difference scheme. They showed the variation of local *Nu* values with *Kn*, *Pe*, and *Br* along the channel. For this case, they found an increase in the thermal entrance length and fully developed *Nu*.

Sun et al. [26] investigated the Graetz problem in slip-flow regime for constant wall heat flux, constant wall temperature and linear variation of wall temperature boundary conditions in a microtube. They considered viscous heating, but neglected axial conduction. Also, rarefaction effects, velocity slip and the temperature jump, were taken into account at boundaries. They solved the governing equations numerically by a finite volume-finite difference scheme. They obtained similar results as Ref. [24]. They stated that, the velocity slip and the temperature jump have inverse effects on heat transfer; while slip velocity increases convection along the surface, temperature jump reduces the temperature gradient and thus the heat transfer along the wall.

Aydin and Avci [27] studied the forced convective heat transfer of hydrodynamically and thermally fully developed laminar, steady state gas flow in micropipes. They included viscous dissipation, velocity slip and temperature jump to their analysis. They solved the governing equations for constant heat flux and constant wall temperature boundary conditions, analytically. They showed the

combined effect of *Kn* and *Br* on *Nu* and temperature distribution. They also discussed the singularities on *Br* and *Nu* variations, and the modified *Br*.

Koo and Kleinstreuer [28] investigated the viscous dissipation effect on temperature distribution and on the friction factor, by scale analysis and numerical simulations. They assumed steady laminar hydrodynamically fully developed incompressible flow in microchannels with circular and rectangular cross-sections. In their analysis, they used water, methanol and iso-propanol as the working fluid, and assumed constant properties except viscosity, which varies with mean flow temperature. They found that viscous dissipation increases as the channel size decreases and the effect of viscous dissipation on friction factor also increase with the reduction of channel size. They concluded their analysis by stating that the viscous dissipation strongly depends on the *Re*, *Pr*, Eckert number, microchannel aspect ratio and the hydraulic diameter.

Yu and Ameel [29] solved the energy equation for hydrodynamically fully developed, incompressible laminar flow of a constant property fluid flowing in a rectangular microchannel with constant wall temperature thermal boundary condition, analytically. They implemented the slip velocity and temperature jump at the wall and neglected the energy dissipation. Analytical method was a modified generalized integral transform technique due to the non-separable nature of the resulting eigenvalue problem. They found that, for a given aspect ratio, heat transfer is reduced always with increasing temperature jump. Also, increasing temperature jump reduced the thermal entrance length. Furthermore, fully developed normalized *Nu* decreased with increasing aspect ratio.

Tunc and Bayazitoglu [30] analyzed thermally and hydrodynamically fully developed flow of a gas at steady-state in rectangular microchannels with axially and peripherally constant heat flux boundary conditions at the walls. They also included the slip velocity and temperature jump at the wall into their analysis, but neglected viscous dissipation. They obtained temperature profile and *Nu* for

varying values of the aspect ratio. They applied the integral transform technique to the incompressible momentum equation in axial direction, to obtain the fully developed velocity profile that includes the slip velocity at the walls. Then they used this velocity profile to solve the energy equation. To solve the energy equation they also used the integral transform technique. They verified their method by comparing the results obtained for the continuum solution. For high *Re* the effect of compressibility, for low *Re* the effect of rarefaction is found to be important. They found that when *Kn* increases, *Nu* decreases due to the increase in temperature jump. Also, the decrease in *Nu* is more significant for smaller aspect ratios, since as the channel size decreases, rarefaction effect increases. When temperature jump is not considered, *Nu* increases as *Kn* increases. This increment is larger for smaller channels due to the increase in the magnitude of the slip velocity.

Hsieh et al. [31] investigated Nitrogen gas flow in a rectangular microchannel with an aspect ratio of 0.25 (50 μm D x 200 μm W x 24,000 μm L) and hydraulic diameter of 80 μm for low *Re*, experimentally and theoretically. The *Re* range was $2.6 \leq Re \leq 89.4$ and the *Kn* range was $0.001 \leq Kn \leq 0.02$. The flow was considered isothermal. They compared their experimental results with analytical results, which were based on a two dimensional continuous flows with first order slip boundary condition. In this analytical solution, they solved the 2D Navier-Stokes and continuity equations and the equation of state for ideal gas with the assumptions of steady-state, isothermal, compressible slip flow, by a perturbation method. They also proposed a new complete momentum accommodation coefficient in terms of *Kn*, which was used in slip velocity equation. They found that the pressure drop has an unusual nonlinear behavior compared to larger channels, which was due to compressibility effect. Analytical results, with slip flow boundary condition, were in good agreement with experimental results and the flow seemed to never reach the fully developed condition under the

experimental conditions. Finally, it was found that the pressure drop is smaller than that for a conventional sized channel.

Lee et al. [32] conducted experiments of single phase flow of deionized water, through rectangular microchannels, made of copper and having hydraulic diameters of 318 to 903 μm. The flow *Re* was ranging from 300 to 3500. The authors carried out the experiments over a range of flow rates. They found that, at a given flow rate, the heat transfer coefficient increased with decreasing channel size. They also made numerical simulations, which model the experimental setup, by commercial software package FLUENT, and compared the numerical results with the experimental ones. Their simulations both include the three dimensional conjugate heat transfer and simplified thin wall case, in which axial conduction was neglected. They obtained a good agreement with the experimental results. They stated that, when the boundary conditions and the entrance effects are coupled carefully with conventional theories, heat transfer in microchannels can be predicted satisfactorily, in the dimensional range of this experiment.

Renksizbulut et al. [33] investigated the slip flow and heat transfer of a constant property gas flow in rectangular microchannels of various aspect ratios. They solved the incompressible form of three dimensional Navier-Stokes equations and energy equations with velocity slip and temperature jump boundary conditions, by using a numerical method based on control volume. They considered the axial conduction effect but neglected viscous dissipation. They considered $0.1 \leq Re \leq 10$ and $Kn \leq 0.1$ range, and $Pr = 1$ case. They found large reductions in the friction factor and *Nu* in the entrance region of the channel, which they attributed to the rarefaction effects. They stated that the entrance lengths were only slightly affected by the rarefaction effects for the range of considered *Re*, but they displayed a highly nonlinear dependence on the channel aspect ratio. They also proposed friction factor and *Nu* correlations, which were functions of *Re*, *Kn*, and the side angle of the channel. The proposed correlations were approximately valid

for rectangular and trapezoidal channels. When the results obtained from these correlations were compared with experimental results, it was seen that correlations deviates about 6% at most from experimental results.

Morini et al. [34] investigated the rarefaction effects on the pressure drop for an incompressible fully developed laminar flow in the slip flow regime $0.001 \leq Kn \leq 0.1$ with an average Mach number less than 0.3, through silicon microchannels having rectangular, trapezoidal and double-trapezoidal cross-sections and various aspect ratios. They treated the flow as steady state and two dimensional, and assumed that the fluid is Newtonian with constant physical properties. They also assumed that all channel walls were rigid and non-porous. They solved the conservation of momentum equation for the fluid by using first-order Maxwell slip boundary condition at the wall, numerically by a code written with the software package FlexPDE. According to the authors this software solves systems of partial differential equations by a Rayleigh-Ritz-Galerkin finite element method. As a result, they stated that for trapezoidal and double-trapezoidal microchannels, the effect of the aspect ratio on the friction factor reduction was strong only if the aspect ratio is less than 0.5. Additionally, for gas flows, the effect of gas rarefaction can be decoupled from the compressibility effects if the average Mach number is less than 0.3 and then, the flow can be analyzed by using the Navier-Stokes equation for incompressible fluids with a slip flow boundary condition at the channel wall if the $Kn$ ranges between 0.001 and 0.1.

Cao et al. [35] investigated the fully developed laminar flow and heat transfer in the slip-flow regime in trapezoidal microchannels. They also assumed the flow as laminar and steady-state, and neglected the viscous dissipation effect. To solve the governing equations, they first converted the physical trapezoidal cross-section to a computational plane of square cross-section via a coordinate transformation; then solved the resulting equations numerically by a finite difference scheme for uniform wall heat flux boundary condition. They discussed rarefaction and

geometrical effects on friction coefficient and *Nu*. They found that the friction coefficient was reduced in the slip-flow region and the effect of aspect ratio and base angle became less obvious at high *Kn*. They also stated that the influences of aspect ratio and base angle on heat transfer were negligible for large temperature jump.

Kuddusi and Çetegen [36] studied the incompressible, hydrodynamically developed, thermally developing gaseous flow in trapezoidal microchannels with hydraulic diameters ranging from 1 to 100 μm, with various aspect ratios. To solve the Navier-Stokes and the energy equations, they used a coordinate transformation, in which the trapezoidal cross-section converted to a unit square cross-section. Then the resulting equations were solved by a finite difference scheme. They validated their method by comparing the obtained thermally developing and fully developed *Nu* values, and friction factors for various channels, with the existing data in the literature. They discussed the effects of aspect ratio and rarefaction and found that when rarefaction increases, friction factor decreases. A similar situation also occurs when aspect ratio increases. They also observed that at low rarefaction values the high heat transfer rate at the entrance diminished rapidly as the developing flow approached the fully developed condition, but at high rarefaction heat transfer did not exhibit considerable change along the channel.

Barber et al. [37] considered the low *Kn* isothermal flows over curved surfaces and questioned the validity of the conventional Maxwell's first order slip velocity equation, which is given in Eq. (1.3). They showed that, this equation is unable to capture important physical properties over curved or rotating surfaces, and demonstrated the limitations with some rarefied flow problems. They also reformulated the slip velocity boundary condition, with the use of the local wall shear stress, to make it suitable for generalized curved surfaces. For a two-dimensional surface, the equation becomes;

$$u_{slip} = \frac{2 - F_M}{F_M} \lambda \left( \frac{\partial u}{\partial y} + \frac{\partial v}{\partial x} \right) \Big|_{y=0} \tag{2.1}$$

Dongari et al. [38] investigated the gaseous slip-flow in a long, parallel plate microchannel. They assumed that the flow was steady, isothermal, two dimensional and locally fully developed with negligible viscous dissipation. They chose the channel long, so the entry and exit effects became negligible. Then, they solved the integral from of Navier-Stokes equations analytically by assuming a second order slip velocity. They also considered the change in axial momentum in their analysis. They validated their theory with the available experimental data and showed that second-order slip velocity gives better results in slip-flow region.

Interest in the effect of surface roughness in micro fluidic systems increased in the last decade. Mala and Li [39] investigated water flow through fused silica and stainless steel microtubes with various diameters between 50 μm and 254 μm experimentally up to *Re* = 2500. The mean surface roughness heights of both tubes were ± 1.75 μm, but shapes and distributions of roughness elements were not known. They observed deviations from the predictions of conventional theories as higher friction factor and friction constant, and a possible early transition from laminar to turbulent flow. For a fixed volume flow rate, the pressure gradient was higher than that predicted by the conventional theory. For small *Re*, the conventional theory and the experimental data were in a rough agreement. However as the *Re* increases, deviation from the conventional theory was observed. The deviation increases as the diameter of the microtubes decreases. They also introduced a *roughness-viscosity model* (RVM) to explain the effects of surface roughness, which depends on the idea of increasing momentum near the wall (around the roughness elements) and zero at the center of the channel. This additional momentum was accounted for by an additional viscosity term in the momentum formulation, similar to eddy-viscosity in turbulent flow. Then the modified momentum equation was solved by a numerical

method. However, this formulation includes a constant that depends on experimental data and geometry of the channel, which makes its use limited. They also proposed an empirical formula for this constant depending on their experimental data, thus a good agreement was obtained between the numerical results and experimental results. Moreover, this model does not include the velocity slip at the wall, since it was developed for liquid flow in microchannel where no-slip condition holds, and its use for gas flows is questionable.

Qu et al. [40] conducted experiments of deionized water flowing through trapezoidal silicon microchannels with hydraulic diameters ranging from 51 μm to 169 μm and measured the flow rate and pressure drop along the channel at steady state. These microchannels were manufactured by anisotropic chemical etching, and have 0.8 μm and 2.0 μm average roughness heights. The physical properties of water involved in the calculations, such as density and dynamic viscosity, were determined from the measured water temperature and assumed to be independent of the pressure. They also modelled the experimental setup and solved with conventional theories. For this purpose, they transformed the two dimensional trapezoidal cross-section to a square computational cross-section by a coordinate transformation, and solved the governing equations with a finite difference scheme. They observed higher pressure gradient and flow friction than the conventional theories and *Re* dependent friction coefficient. They concluded their analysis by applying the RVM proposed by Ref. [39] with a new formula for the previously mentioned constant, and found good agreement for relatively low *Re* values.

In a proceeding work, Qu et al. [41] investigated the heat transfer characteristics of deionized water flowing through trapezoidal silicon microchannels, which were also produced by anisotropic chemical etching. These microchannels had hydraulic diameters ranging from 62 μm to 169 μm and average roughness heights of 0.8 μm and 2.0 μm. The temperatures, flow rate and the pressure drop

along the microchannel were measured. They also solved the conjugate heat transfer problem, which combines heat conduction in the solid region and heat convection in the fluid region, numerically. They neglected the entrance effects, viscous dissipation and axial heat conduction, and assumed a laminar, fully developed flow at steady state in the trapezoidal microchannels. Then, momentum and energy equations were solved for no-slip and no temperature jump boundary conditions with a finite difference scheme. They observed smaller *Nu* values than the conventional theory, which was a result of surface roughness. They also applied the RVM that was modified for the trapezoidal microchannels [40] and proposed new modified *Nu* relationship. Good agreement between experimental *Nu* and modified *Nu* was obtained.

Kandlikar et al. [42] experimentally investigated the effect of surface roughness on pressure drop and heat transfer by using stainless steel mini tubes having 1.032 mm and 0.62 mm diameters, and distilled water as the working fluid. The roughness of the tubes was changed by etching them with an acid solution. Thus, they obtained relative roughness values of 0.00178 to 0.00281 for the tube having 1.067 mm diameter, and 0.00161 to 0.00355 for the tube of 0.62 mm diameter. They conducted the experiments for a *Re* range of 500 to 2600 for the 1.067 mm tube and 900 to 3000 for 0.62 mm tube. They compared the experimental local *Nu* values with theoretical ones and showed that the agreement is within the experimental uncertainties. They found that the effect of surface roughness on pressure drop and heat transfer for the larger tube were negligible, but for the 0.62 mm tube heat transfer and pressure drop showed dependence on the surface roughness, namely highest heat transfer and pressure drop occurred in the tube with highest relative roughness value. They concluded with the recommendation of further research on tubes with much smaller diameters.

Sun and Faghri [43] numerically investigated the effects of relative surface roughness, roughness distribution, and gas rarefaction on nitrogen flow in a

parallel plate channel where the roughness was modeled by an array of rectangular obstructions placed on sides of channel. They used the DSMC method in slip-flow regime. They found that the friction coefficient increased as the roughness height increased, and also when the distance between the roughness modules decreased. They stated that the effect of surface roughness was more pronounced at low *Kn*, which was the result of reduced interaction between the gas molecules and channel walls at high *Kn* values.

Hu et al. [44] investigated the effect of surface roughness, mainly effects of the roughness elements' height, size, spacing and channel height, on velocity distribution and pressure drop. They considered a steady state pressure driven fully developed water flow in low *Re* regime ($0.001 < Re < 10$) in a microchannel formed by two parallel plates, and modeled the roughness elements as rectangular prisms on the surfaces. For simplicity, they neglected the turbulence and the wake between roughness elements, and the channel side wall effects. Then, they solved the three dimensional Navier-Stokes equations numerically with no-slip boundary condition for different heights, sizes and arrangements of roughness elements. The numerical method used was the finite volume method. They found that the pressure drop per unit length increases when roughness height increases or when the roughness size increases while keeping the spacing between the roughness elements constant. When the spacing increased or the channel height increased, pressure drop per unit length decreased.

Later, Baviére et al. [45] studied the same geometry, properties and boundary conditions of Ref. [44] only by extending the *Re* range to $1 < Re < 200$, both analytically and numerically. For numerical simulation they used the commercial CFD software FLUENT. Their analytical model was based on the method for predicting the rough-wall skin friction in turbulent flows. They found that the flow was independent of the *Re* in the considered range.

Another experimental work was proposed by Wu and Cheng [46]. They conducted experiments of laminar deionized water flow in 13 trapezoidal silicon microchannels, which had different geometric parameters, surface roughness and surface hydrophilic properties. Trapezoidal microchannels were formed by wet etching of the <100> silicon wafers in a solution of KOH. To study the effect of surface hydrophilic property on the flow and heat transfer, some of the channels were deposited by a thermal oxide layer to increase their surface hydrophilic capacity. They found that the *Nu* and the friction constant increased with increasing surface roughness and surface hydrophilic property, especially at high *Re* values. Heat transfer in microchannels having strong hydrophilic surfaces was enhanced, especially at high *Re*, with increase in pressure drop. However, they also stated that the geometric parameters have more effect on the performance of the microchannel than the surface roughness and surface hydrophilic property. Furthermore, they found sharp and almost linear increase in *Nu* with increasing *Re* for $Re < 100$ flows, but after that the increase was smooth. Moreover, they proposed two correlations for *Nu* for the *Re* ranges of $10 < Re < 100$ and $100 < Re < 1500$, and one for the apparent friction constant depending on their experimental results, as given below:

*For* $10 < Re < 100$:

$$Nu = C_1 Re^{0.946} Pr^{0.488} \left(1 - \frac{W_b}{W_t}\right)^{3.547} \left(\frac{W_t}{H}\right)^{3.577} \left(\frac{k}{D_h}\right)^{0.041} \left(\frac{D_h}{L}\right)^{1.369} \quad (2.2)$$

*For* $100 < Re < 1500$:

$$Nu = C_2 Re^{0.148} Pr^{0.163} \left(1 - \frac{W_b}{W_t}\right)^{0.908} \left(\frac{W_t}{H}\right)^{1.001} \left(\frac{k}{D_h}\right)^{0.033} \left(\frac{D_h}{L}\right)^{0.798} \quad (2.3)$$

*For* $10 < Re < 1500$:

$$f_{app} Re = C_3 Re^{0.089} \left(1 - \frac{W_b}{W_t}\right)^{4.359} \left(\frac{W_t}{H}\right)^{4.444} \left(\frac{k}{D_h}\right)^{0.028} \left(\frac{D_h}{L}\right)^{1.023} \quad (2.4)$$

where $C_1 = 6.7$, $C_2 = 47.8$, and $C_3 = 508.7$ for silicon surfaces, and $C_1 = 6.6$, $C_2 = 54.4$, and $C_3 = 540.5$ for thermal oxide surfaces. Also, $W_b$ is the bottom width of the channel, $W_t$ is the top width of the channel, $H$ is the height of the channel, $k$ is the surface absolute roughness, $D_h$ is the hydraulic diameter (thus $k / D_h$ gives the surface relative roughness), and $L$ is the length of the channel. These equations are valid for $0 \leq W_b / W_t \leq 0.934$, $0.038 \leq H / W_t \leq 0.648$, $3.26x10^{-4} \leq k / D_h \leq 1.09x10^{-2}$, $191.77 \leq L / D_h \leq 453.79$, and $4.05 \leq Pr \leq 5.79$ for Eq. (2.2) and $4.44 \leq Pr \leq 6.05$ for Eq. (2.3). According to the authors, range of deviations of these equations from experimental data is 20.3%, 19.8% and 19.3% for Eqns. (2.2), (2.3), and (2.4), respectively.

Kleinstreuer and Koo [47] proposed the *porous medium layer* (PML) model to investigate the effects of surface roughness on the friction factor for liquid flows in micro-conduits. Roughness on the wall is considered as a porous medium and its effect is modeled by the resistance offered by this porous layer. They showed the application of this model for steady, laminar, fully developed liquid flows in two dimensional microchannels, microtubes, and micro-journal bearings. They stated that the model predicts the friction factor well compared with the experimental data in literature, where the relative roughness was significant. Koo and Kleinstreuer [48] extend their work by analyzing the effect of surface roughness on heat transfer in such conduits. They found that the surface roughness effect on heat transfer was less significant than on momentum transfer. Furthermore, the effect of *Re* on *Nu* was found to be negligible compared to its effect on friction factor.

Turner et al. [49] conducted experiments to investigate laminar gas flow in microchannels. They used five smooth microchannels (relative roughness values were between 0.001 to 0.006) that were etched into <100> silicon wafers and had hydraulic diameters in the range $4.7 < D_h < 95$ μm, and three rough microchannel etched into <110> silicon wafers with hydraulic diameters in the range $10 < D_h <$

*96* μm and relative roughness values of 0.02, 0.03, and 0.06. When relative roughness and Mach number were kept small, agreement between the measured friction factor and theoretical incompressible value was good for $Kn < 0.01$. Above this, friction factor decreased. When *Kn* reached a value of 0.15, the reduction in the friction factor was 50%. Also, for laminar gas flow they did not observe any significant effect of relative surface roughness on friction factor and obtained similar results to those obtained from Moody's chart. However, this observation is different from the other studies and needed to be verified. Moreover, they found that the friction factor was independent of surface roughness for rarefied gas flow, had minor influence in compressible flow, in the experimental surface roughness range.

Croce and D'Agaro [50] performed numerical simulations of heat transfer and pressure loss in rough microtubes and microchannels, having diameters ranging from 50 μm to 150 μm and relative roughness height ranging from 0.0% to 5.3%, with a finite element CFD code. They assumed laminar incompressible fully developed flow of liquid R-114 at steady state and neglected viscous dissipation. They modeled the surface roughness as randomly generated rectangular and triangular peaks on the smooth surface. They found an increase in Poiseuille number relative to a smooth surface. They also stated that the effect of surface roughness on heat transfer depends on the roughness elements and channel geometry. In a proceeding work [51], they compared their results with the RVM by Mala and Li [39] and the PML by Koo and Kleinstreuer [47], and obtained reasonably good agreement.

Wang et al. [52] introduced the method of regular perturbation to study the effect of wall roughness on Poiseuille flow in parallel plate microchannels. They considered a steady state laminar fully developed flow of a Newtonian fluid and solved the Navier-Stokes equation by introducing the stream function, with no-slip boundary condition. The wall roughness was modeled by superimposing a

series of harmonic functions. They stated that the effect of roughness on friction factor depends on the energy dissipation of the fluid while the effect of the roughness on flow pattern depends on the kinetic energy of the main flow.

To extend the understanding of the roughness effect and to characterize it, Kandlikar et al. [53] proposed three new roughness characterization parameters, namely the maximum profile peak height $R_p$, mean spacing of profile irregularities $R_{Sm}$, and floor distance to mean line $F_p$, which are shown in Fig. (2.1).

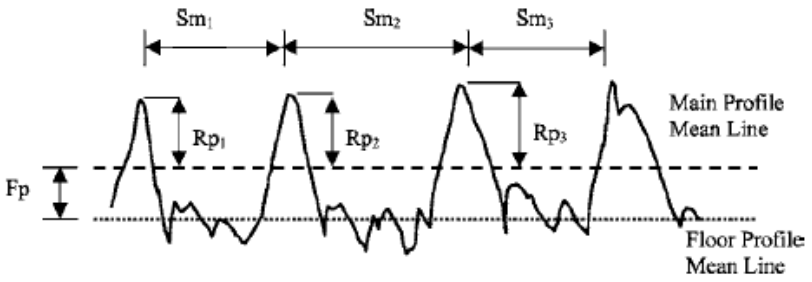


Figure 2.1: Graphical representation of maximum profile peak height $R_p$, mean spacing of profile irregularities $R_{Sm}$, and floor distance to mean line $F_p$ [53].

The authors also presented three additional parameters to consider the local hydraulic diameter variation: maximum, minimum, and average. With these new parameters, they defined the roughness height $\varepsilon$, constricted flow diameter $D_{cf}$, and related modified $Re$ and friction factor as;

$$\varepsilon = R_p + F_p \tag{2.5}$$

$$D_{cf} = D_t - 2\varepsilon \tag{2.6}$$

$$Re_{cf} = \frac{4\dot{m}}{\pi D_{cf}\mu} \tag{2.7}$$

$$f_{Darcy,cf} = \frac{64}{Re_{cf}} \tag{2.8}$$

where $\dot{m}$ is the mass flow rate in kg/s, and μ is the dynamic viscosity in Ns/m$^2$. Later, they modified the Moody's diagram with these new parameters, as given in Fig (2.2). They also conducted some experiments with air and water in rectangular channels with hydraulic diameters ranging from 325 to 1819 μm, relative roughness values based on constricted flow diameter from 1% to 14%, *Re* values from 200 to 7200 for air and 200 to 5700 for water. They observed early laminar to turbulent transition with increasing relative roughness. This is a still-developing method and they stated that understanding the 3D effects of roughness is needed for future work. In a following study, Taylor et al. [54] discussed these new parameters as well as the historical development of surface roughness investigations. They also discussed the future work, standardization, and needs of this field.

Celata et al. [55] investigated the effect of channel wall roughness and wall hydrophobicity in circular microchannels having diameters of 70 to 326 μm with relative roughness less than 1%, experimentally, as well as experiments conducted in smooth tubes with diameters of 31 to 259 μm. Test microtubes were made of fused silica, glass and Teflon. Rough tubes were obtained from smooth glass tubes by using fine-grain abrasive powder and liquid silicon oil. The working fluid was demineralised and degassed water. They did not observe any deviation from classical laws for the smooth cases. Moreover, they did not encounter any effect of slip flow due to hydrophobic channel walls and the cause of liquid slip flow observed in some researches was attributed to local desorption of dissolved gases. They did not observe any early transition to turbulent flow either.

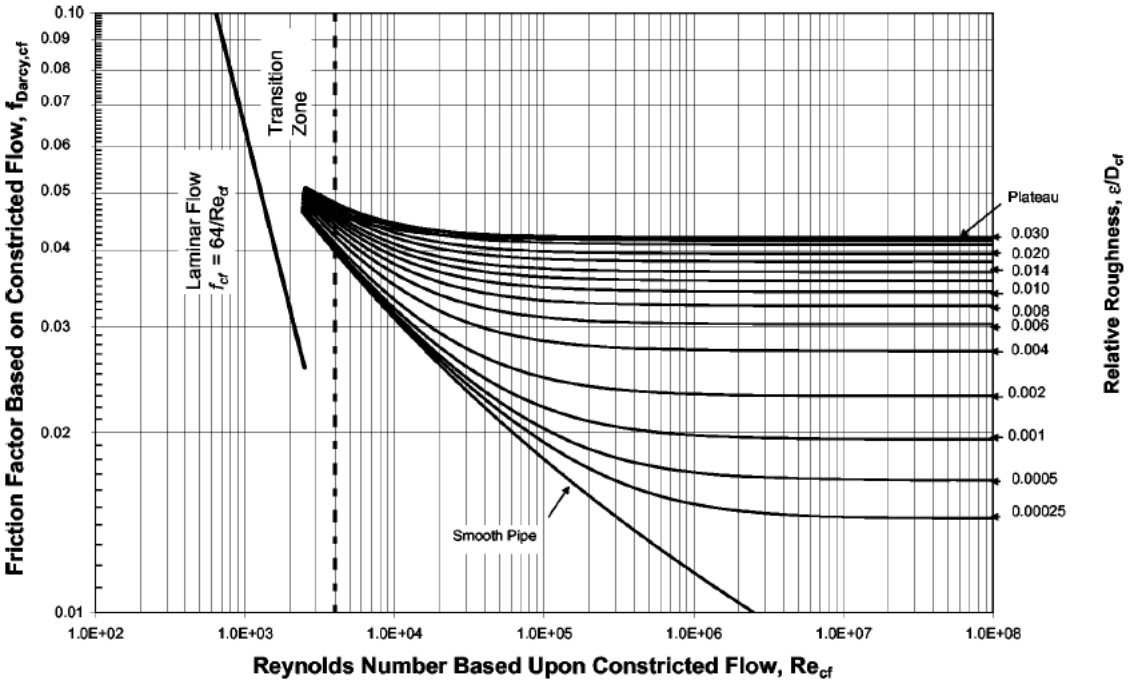


Figure 2.2: Modified Moody's friction factor chart [53].

Rawool et al. [56] performed a three-dimensional numerical simulation of air flow through a serpentine microchannel having square cross-section with designed roughness. Roughness elements were modeled as trapezoidal, rectangular and triangular obstructions placed along the channel wall. They used the commercial CFD software CFD-ACE+ for the simulation and solved the steady state Navier-Stokes equations with no-slip boundary conditions for the *Re* range $40 < Re < 200$. They found that the friction factor was bigger for the rectangular and triangular obstruction cases than the trapezoidal obstruction case, and it increased as the obstruction heights increased. They also found that the pressure drop decreases as the obstruction pitch increases.

Shen et al. [57] investigated single phase convective heat transfer in a compact heat sink consisting of 26 rectangular microchannels each having dimensions of 300 μm width and 800 μm depth. Microchannels were made of copper and

relative roughness was 4-6%. They used deionized water as the working fluid in the experiments and conducted the test for the *Re* range of $162 < Re < 1257$ with different water inlet temperatures and heating powers. They found higher Poiseuille numbers than the conventional values in high *Re* regimes, and an increase with increasing *Re* values. They also found significantly low local and average *Nu* and observed increase both in local and average *Nu* with increasing *Re* and *Pr*, which was attributed to surface roughness effect. Furthermore, they did not observe any early transition from laminar to turbulent flow.

Ji et al. [58] investigated the effect of surface roughness on two dimensional, rarefied, compressible gas flow through a parallel plate microchannel, numerically. Simulated gas was nitrogen having constant thermophysical properties with inlet Mach number ranging from 0.0055 to 0.202 and *Re* ranging from 0.001 to 100. Roughness was modeled by rectangular slabs which were uniformly and symmetrically distributed on the plates. They solved the compressible form of the Navier-Stokes and the energy equations for constant wall temperature boundary condition with second order velocity slip and temperature jump at the walls. The numerical method was based on finite volume method. Numerical simulations were carried out for relative roughness heights from 0.1% to 6% where they defined the relative roughness height as the ratio of roughness height over channel height. They found that the effect of surface roughness on the flow was stronger for low *Kn* values. They also stated that the reduction in average *Nu* was more significant for rarefied flow compared to compressible flow, and the roughness affects the Poiseuille number more than the average heat transfer rate.

Cao et al. [59] performed non-equilibrium molecular dynamics simulations to investigate the effect of surface roughness on rarefied gas flows. In their simulations, they assumed locally fully developed flow of gaseous argon flowing through submicron platinum channels with roughness. The roughness elements

were modeled as triangular, rectangular, sinusoidal, and randomly generated triangular waves. They found smaller slip length than the Maxwell model's prediction, and higher friction coefficient compared to smooth channels. They also stated that the roughness geometry had great influence on the friction characteristics.

Tang et al. [60] reviewed the experimental studies on friction factor and then conducted experiments to investigate the effects of compressibility, rarefaction and surface roughness on the friction factor of gaseous nitrogen and helium flow in microchannels. To investigate the surface roughness effect, they used fused silica microtubes, stainless steel microtubes and fused silica square microchannels with diameters ranging from 50 to 201 μm, 119 to 300 μm and hydraulic diameters from 52 to 100 μm, respectively. To investigate the rarefaction effect, they used fused silica microtubes with diameters from 10 to 20 μm. They observed much higher friction factors than the conventional theories in stainless steel tubes, which had the most dense roughness elements among the tested micro conduits. Friction factor for the fused silica tubes and channels agreed with the theoretical values. Tests with small diameter tubes showed reduction in friction factor that was attributed to the rarefaction effect.

Wang and Wang [61, 62] studied the roughness effect by a regular perturbation method in two separate cases. In the first case [61], the flow was in microtubes where roughness was modeled by a two dimensional simple harmonic function. The relative roughness was from 0 to 0.05 and the flow *Re* range was $1 < Re < 500$. They included the effects of viscous dissipation, but neglected the velocity slip. They found an increase in pressure drop with the increase of relative roughness. In the second case [62], the flow was between parallel plates where they defined the roughness as a wave on the surfaces. They considered up to 10% relative roughness and *Re* range of $1 < Re < 200$ in their computations. They solved the incompressible two dimensional Navier-Stokes equations with no-slip

boundary condition. For this purpose, they transformed the domain into a smooth one by coordinate transformation. Then, related equations were solved by a perturbation method. They found that the flows were viscous dominant for low *Re* flows and separation from surface occurred for large relative roughness values at high *Re* values.

Recently, Croce et al. [63] extended their previous work [50] to three dimensions. They defined the roughness elements as three dimensional conical peaks on a plane microchannel that result the relative roughness ranging from 0.05% to 2.65%. They considered laminar flow of an incompressible fluid with constant properties and neglected the viscous dissipation. They solved the related equations numerically with no-slip and constant wall temperature boundary conditions for different peak heights and different peak arrangements. The numerical simulation was based on a finite element method. They found that roughness had an important effect on pressure drop and less on heat transfer. Also, they stated the importance of the roughness elements' geometrical properties on microchannel performance.

Later, Croce et al. [64] performed a numerical analysis of compressibility and rarefaction effects on pressure drop in parallel plate microchannels with relative surface roughness from 0% to 2.65%. They modeled the roughness as triangular obstructions in a portion of the channel. They considered viscous dissipation in their analysis and assumed constant fluid physical properties. They solved the compressible form of the Navier-Stokes and energy equations with generalized Maxwell slip and constant temperature boundary conditions, but neglected the temperature jump at the walls. Resulting equations were solved with a hybrid finite volume-finite difference solver. They found great effect of rarefaction on Poiseuille number; however roughness geometry reduces this effect. Also, roughness effect was found to be stronger at high *Kn*.

In the light of above literature search, it was seen that most of the studies dealing with surface roughness effect were done with the continuum assumptions, which were no-slip and/or no temperature jump. Moreover, studies of gas flows in slip-flow regime in rough microchannels are rare, especially for heat transfer analysis. As a result, very little data exists in the open literature, and studies considering roughness and channel geometrical properties as well as different flow conditions are still needed. Thus, in this study gas flow in the slip-flow regime in a rough microchannel is considered with laminar incompressible flow and constant fluid thermophysical properties assumptions. Then, Navier-Stokes and energy equations are solved with appropriate boundary conditions for two dimensional geometries.

# CHAPTER – 3

## PROBLEM DEFINITION AND NUMERICAL METHOD

For the 2D case, a laminar, viscous, incompressible, single-phase Newtonian flow at steady state between parallel plates with constant wall temperatures is considered. The fluid is assumed to have constant thermo-physical properties. The flow is assumed to have uniform velocity and temperature at the channel inlet and the flow is in slip-flow regime inside the channel. This slip effect is accounted for by imposing the slip velocity and temperature jump boundary conditions at the wall. The roughness is modeled by adding triangular obstructions along one of the channel walls. Then, the Navier-Stokes and energy equations are solved with appropriate boundary conditions, numerically. Since the fluid is assumed to have constant thermo-physical properties, Navier-Stokes and energy equations are solved separately. The numerical method is the Galerkin based reduced integration penalty finite element method for the Navier-Stokes equations, and standard Galerkin finite element method for the energy equation, which are explained in the following sections. Also, numerical calculations are carried out in an equivalent parallel plate channel with smooth surfaces to test the numerical code and to compare the results with those obtained from the rough channel.

### 3.1 – Problem Geometry and Boundary Conditions:

Geometry of the smooth channel is given in Fig. (3.1), and the rough channel in Fig. (3.2), schematically. Also, the applied boundary conditions are shown on the figures.

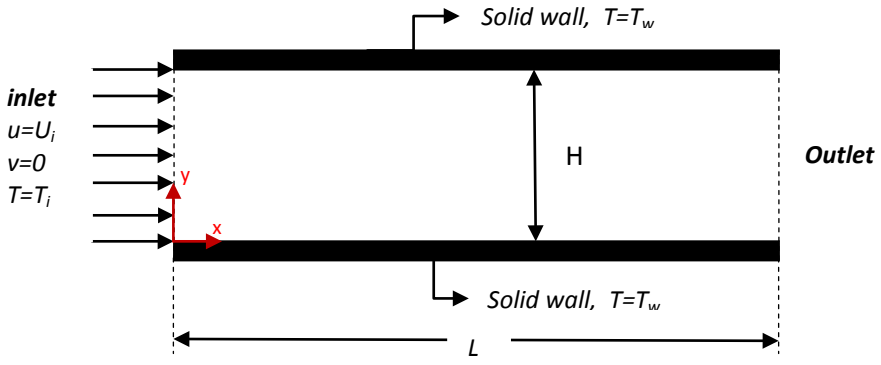


Figure 3.1: Schematic of the smooth channel.

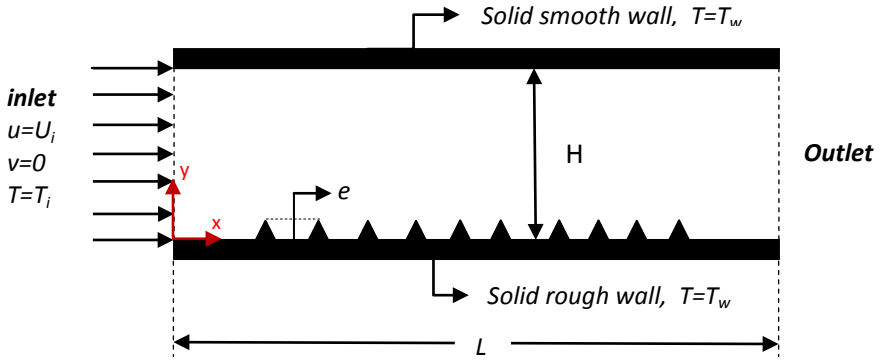


Figure 3.2: Schematic of the rough channel.

Boundary conditions can be summarized as follows:

*Inlet:* $u = U_i, \quad v = 0, \quad T = T_i$

*Solid walls:* $v = 0$

$$u_s = \frac{2 - F_M}{F_M} \lambda \left( \frac{\partial u_t}{\partial n} + \frac{\partial u_n}{\partial t} \right)_w \tag{3.1}$$

$$T_s - T_w = \frac{2\gamma}{\gamma + 1} \frac{2 - F_T}{F_T} \frac{\lambda}{Pr} \left( \frac{\partial T}{\partial n} \right)_w$$

*Outlet:* traction free

Since the tangential momentum accommodation coefficient, $F_M$ and the thermal accommodation coefficient, $F_T$ is close to unity in most of the engineering applications, many of the numerical simulations in literature are carried out by selecting them as 1, if no special interest on their value is sought. Thus, in this study, they are selected as 1 to better compare the results.

Relative roughness, $\varepsilon$, of the channel surface is defined as

$$\varepsilon = \frac{e}{D_h} \tag{3.2}$$

where $e$ is the average height of the roughness elements, and $D_h$ is the hydraulic diameter of the channel. In most of the studies in literature, it is stated that silicon micro-channels generally have a relative roughness value between 0 – 4%. Thus, in this study, relative roughnesses of 1.325%, 2.0% and 2.65% are considered. The 2.65% relative roughness value is considered only in continuum regime to compare with literature. Geometrical properties of the roughness elements are shown in Fig. (3.3). Base angles of the triangular roughness elements are 45 degrees and spacing between the peaks of roughness elements is 5 times of their height. Such kind of geometrical properties and spacing of roughness element is used in a case in Ref. [50] where incompressible flow with no-slip boundary conditions is investigated and in Ref. [64] where compressible flow is

investigated. These elements are replaced in the middle of the channel. There are a total of 30, 20, and 15 elements along the channel for the cases of 1.325%, 2.0% and 2.65% relative roughness, respectively.

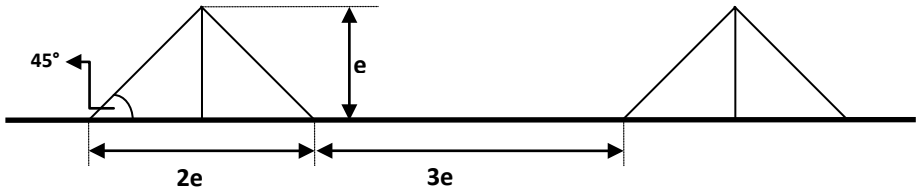


Figure 3.3: Geometrical properties of the roughness elements on the channel surface.

### 3.2 – Governing Equations:

Governing equations for two dimensional, steady, viscous flow of a Newtonian fluid with constant properties are the continuity, momentum, and energy equations. By neglecting the body forces, the continuity and momentum equations, and the energy equation with axial conduction and viscous dissipation, can be written in vectorial form in Cartesian coordinates as;

*Continuity:* $$\nabla . \vec{\boldsymbol{u}} = 0 \tag{3.3}$$

*Momentum:* $$\rho(\vec{\boldsymbol{u}}.\nabla\vec{\boldsymbol{u}}) = -\nabla p + \nabla \cdot (\mu[(\nabla\vec{\boldsymbol{u}}) + (\nabla\vec{\boldsymbol{u}})^T]) \tag{3.4}$$

*Energy:* $$\rho C_P(\vec{\boldsymbol{u}} \cdot \nabla T) = \nabla \cdot (k\nabla T) + \Phi \tag{3.5}$$

These equations can be written in non-dimensional form by using the following non-dimensional parameters;

$$\bar{u} = \frac{u}{U_m} \qquad \bar{v} = \frac{v}{U_m} \qquad \overline{x} = \frac{x}{D_h} \qquad \overline{y} = \frac{y}{D_h}$$
$$\bar{P} = \frac{P}{\rho U_m^2} \qquad \theta = \frac{T - T_w}{T_i - T_w} \qquad Kn = \frac{\lambda}{H} \qquad Re = \frac{\rho U_m D_h}{\mu} \tag{3.6}$$
$$\vartheta = \frac{\mu}{\rho} \qquad \alpha = \frac{k}{\rho c_p} \qquad Pr = \frac{\vartheta}{\alpha} \qquad Br = \frac{\mu U_m^2}{k(T_i - T_w)}$$
$$Pe = RePr$$

where $U_m$ is the mean velocity, $H$ is the channel height, $\rho$ is the fluid density, $\mu$ is the fluid dynamic viscosity, $\vartheta$ is the fluid kinematic viscosity, $\alpha$ is the fluid thermal diffusivity, $k$ is the fluid thermal conductivity, $c_p$ is the specific heat of the fluid at constant pressure, $\theta$ is the non-dimensional temperature, $T_w$ is the constant channel wall temperature, $T_i$ is the constant fluid inlet velocity, $Kn$ is the Knudsen number, $Re$ is the Reynolds number, $Pr$ is the Prandtl number, $Pe$ is the Peclet number, and $Br$ is the Brinkman number. After substituting the non-dimensional parameters given in Eq. (3.6) into Eqs. (3.3) through (3.5) and the boundary condition set given in Eq. (3.1), and removing the bar signs over the non-dimensional parameters for simplicity, the governing equations became:

*Continuity:*
$$\nabla .\ \vec{\boldsymbol{u}} = 0 \tag{3.7}$$

*Momentum:*
$$(\vec{\boldsymbol{u}}.\nabla\vec{\boldsymbol{u}}) = -\nabla p + \frac{1}{Re}\nabla \cdot [(\nabla\vec{\boldsymbol{u}}) + (\nabla\vec{\boldsymbol{u}})^T] \tag{3.8}$$

*Energy:*
$$(\vec{\boldsymbol{u}} \cdot \nabla\theta) = \frac{1}{Pe}\{\nabla \cdot (\nabla\theta) + \Phi\} \tag{3.9}$$

and

$$\begin{aligned} &x = 0: && u = 1, \quad v = 0, \quad \theta = 1 \\ &y = 0,\ y = H: && u_s = \frac{2 - F_M}{F_M}(Kn)\left(\frac{\partial u_t}{\partial n} + \frac{\partial u_n}{\partial t}\right)_w \\ & && \theta_s = \frac{2\gamma}{\gamma + 1}\frac{2 - F_T}{F_T}\frac{(Kn)}{Pr}\left(\frac{\partial \theta}{\partial n}\right)_w \end{aligned} \tag{3.10}$$

The local Nusselt number is defined as,

$$Nu_x = \frac{h_x D_h}{k} \tag{3.11}$$

where $h_x$ is the local heat transfer coefficient and written as,

$$h_x = \frac{k}{(T_m - T_w)}\left(\frac{\partial T}{\partial n}\right)_w \tag{3.12}$$

When the non-dimensional parameters given in Eq. (3.6) are used, Eq. (3.11) become,

$$Nu_x = \frac{D_h}{\theta_m}\left(\frac{\partial \theta}{\partial n}\right)_w \tag{3.13}$$

where $\theta_m$ is the non-dimensional mean temperature and can be calculated by,

$$\theta_m = \frac{\int_A u\,\theta\,dA}{\int_A u\,dA} \tag{3.14}$$

Also, the mean velocity along the channel can be calculated by,

$$u_m = \frac{\int_A u\, dA}{\int_A dA} \tag{3.15}$$

### 3.3 – Numerical Method:

Governing equations are solved numerically by a Galerkin based Finite Element Method (FEM), explicitly the reduced integration penalty finite element method for the hydraulic part and standard Galerkin FEM for the energy part. FEM is a powerful method in comparison with the other methods such as finite volume or finite differences for problems involving complex geometries and boundary conditions [65]. Briefly, in FEM, first the computational domain is discretized into finite elements, which is also called mesh (or grid) generation. Mesh generation can be done by using either triangular or quadrilateral elements in two-dimensional geometries, and tetrahedral, prism, or hexahedral (brick) elements in three-dimensional geometries. Then, the governing equations of the problem in interest are written in weighted integral sense (weak formulation) and by using this weak form, finite element model of the problem is developed. After the model development, elements used in the domain are assembled to obtain the global system of algebraic equations that define the problem. Finally, the equation set is solved after implementing the boundary conditions [66]. These steps will be shown in reasonable detail for the momentum and energy equations in the following subsections. Additional information can be obtained from Refs. [65] and [66].

### 3.3.1 – Formulation of the Momentum Equations:

Considering the momentum equations in open form, all nonzero expressions are taken to one side of the equality sign. Then, the resulting equations are multiplied with a weight (test) function $\delta u_i$, and integrated over the element domain $\Omega^e$ to obtain the needed weighted integral statements (weak forms of the equations).

*x-momentum:*

$$\int_{\Omega^e} \delta u_i \left[ \left( u\frac{\partial u}{\partial x} + v\frac{\partial u}{\partial y} \right) - \frac{2}{Re}\left( \frac{\partial^2 u}{\partial x^2} \right) - \frac{1}{Re}\frac{\partial}{\partial y}\left( \frac{\partial u}{\partial y} + \frac{\partial v}{\partial x} \right) + \frac{\partial P}{\partial x} \right] dx\, dy = 0 \qquad (3.16)$$

*y-momentum:*

$$\int_{\Omega^e} \delta u_i \left[ \left( u\frac{\partial v}{\partial x} + v\frac{\partial v}{\partial y} \right) - \frac{2}{Re}\left( \frac{\partial^2 v}{\partial y^2} \right) - \frac{1}{Re}\frac{\partial}{\partial x}\left( \frac{\partial u}{\partial y} + \frac{\partial v}{\partial x} \right) + \frac{\partial P}{\partial y} \right] dx\, dy = 0 \qquad (3.17)$$

Also, it is necessary to equally distribute the integration between the dependent variables and weight functions in the second order partial derivatives of these equations. For this purpose, one should use the integration by parts (Green-Gauss Theorem) in two dimensions. Resulting weak statements of these equations forms the variational problem subjected to a constrained which is continuity equation. In penalty function method, problem is reformulated as an unconstrained one. Since the velocity field constrained to satisfy the continuity equation, the weight functions of velocity components also satisfy the continuity equation,

$$\frac{\partial \delta u_x}{\partial x} + \frac{\partial \delta u_y}{\partial y} = 0 \qquad (3.18)$$

As a result of this formulation, pressure does not appear explicitly in variational problem. Details of the formulation can be found in Ref. [66]. At last, weak forms are given as for x-momentum;

$$\int_{\Omega^e} \delta u_i \left(u\frac{\partial u}{\partial x} + v\frac{\partial u}{\partial y}\right) dx\, dy$$

$$+ \frac{1}{Re}\int_{\Omega^e} \left[2\frac{\partial \delta u_i}{\partial x}\frac{\partial u}{\partial x} + \frac{\partial \delta u_i}{\partial y}\left(\frac{\partial u}{\partial y} + \frac{\partial v}{\partial x}\right)\right] dx\, dy \tag{3.19}$$

$$+ \int_{\Omega^e} \epsilon_p \frac{\partial \delta u_i}{\partial x}\left(\frac{\partial u}{\partial x} + \frac{\partial v}{\partial y}\right) dx\, dy = \oint_{\Gamma^e} \delta u_i t_x d\Gamma$$

where

$$t_x = \left[\frac{2}{Re}\frac{\partial u}{\partial x} + \epsilon_p\left(\frac{\partial u}{\partial x} + \frac{\partial v}{\partial y}\right)\right] n_x + \frac{1}{Re}\left(\frac{\partial u}{\partial y} + \frac{\partial v}{\partial x}\right) n_y \tag{3.20}$$

and for y-momentum;

$$\int_{\Omega^e} \delta u_i \left(u\frac{\partial v}{\partial x} + v\frac{\partial v}{\partial y}\right) dx\, dy$$

$$+ \frac{1}{Re}\int_{\Omega^e} \left[2\frac{\partial \delta u_i}{\partial y}\frac{\partial u}{\partial y} + \frac{\partial \delta u_i}{\partial x}\left(\frac{\partial u}{\partial y} + \frac{\partial v}{\partial x}\right)\right] dx\, dy \tag{3.21}$$

$$+ \int_{\Omega^e} \epsilon_p \frac{\partial \delta u_i}{\partial y}\left(\frac{\partial u}{\partial x} + \frac{\partial v}{\partial y}\right) dx\, dy = \oint_{\Gamma^e} \delta u_i t_y d\Gamma$$

where

$$t_y = \frac{1}{Re}\left(\frac{\partial u}{\partial y} + \frac{\partial v}{\partial x}\right) n_x + \left[\frac{2}{Re}\frac{\partial v}{\partial y} + \epsilon_p\left(\frac{\partial u}{\partial x} + \frac{\partial v}{\partial y}\right)\right] n_y \tag{3.22}$$

Since the pressure term does not appear in momentum equations, it can be computed by the relation

$$P = -\epsilon_p \left( \frac{\partial u}{\partial x} + \frac{\partial v}{\partial y} \right) \tag{3.23}$$

In Eqs. (3.19-3.23), $\epsilon_p$ is the penalty parameter, which should be between $10^4$ to $10^{12}$ according to Ref. [66]. It is also stated that, magnitude of the penalty parameter depends on many other parameters such as mesh, computer capacity, and *Re*. When penalty parameter is too high, system matrix become singular and locking occurs. In this study, when penalty parameter was chosen as $10^{12}$, system matrix became singular. When it was chosen as $10^{10}$ and $10^{11}$, convergence problems occurred. Also, when it was selected as $10^9$, convergence took an unnecessarily long time. Thus, penalty parameter is chosen as $10^8$ in this study. As a result, pressure and continuity equation drop out from the system equation set. After solving the velocity field, pressure can be computed if needed with known velocities using Eq. (3.23) or by pressure Poisson equation, which can be obtained by differentiating *x*- and *y*-momentum equations with respect to x and y, respectively, and summing the resulting equations.

In Eqs. (3.19-3.22), *u* and *v* are primary variables; $t_x$ and $t_y$ are secondary variables which define the total boundary stress. The line integrals in Eqs. (3.19) and (3.21) containing the secondary variables are called the boundary integrals and their solution procedure depends on the boundary conditions of the problem. Integrals in these equations will be evaluated numerically using 2x2 or 3x3 Gauss – Legendre quadrature, depending on the elements used in the finite element mesh. It is necessary to use at least 2x2 quadrature for bilinear elements (i.e., 4-node quadrilateral element), and 3x3 quadrature for quadratic elements (i.e., 9-node quadrilateral element).

Substituting the shape (approximation) functions, $\psi_i$, for the non-dimensional velocity components and the weight function,

$$u = \sum_{j=1}^{n} u_j \Psi_j(x,y) \qquad v = \sum_{j=1}^{n} v_j \Psi_j(x,y) \qquad \delta u_i = \Psi_i \tag{3.24}$$

where $n$ is the total node number used in the computational element, into the Eqs. (3.19-3.22), gives for the $x$-momentum:

$$\begin{aligned}
&\sum_{j=1}^{n} \int_{\Omega^e} \Psi_i \left[ \bar{u} \frac{\partial \Psi_j}{\partial x} + \bar{v} \frac{\partial \Psi_j}{\partial y} \right] u_j \, dx \, dy \\
&\quad + \sum_{j=1}^{n} \int_{\Omega^e} \frac{1}{Re} \left( 2 \frac{\partial \Psi_i}{\partial x} \frac{\partial \Psi_j}{\partial x} + \frac{\partial \Psi_i}{\partial y} \frac{\partial \Psi_j}{\partial y} \right) u_j \, dx \, dy \\
&\quad + \sum_{j=1}^{n} \int_{\Omega^e} \frac{1}{Re} \left( \frac{\partial \Psi_i}{\partial y} \frac{\partial \Psi_j}{\partial x} \right) v_j \, dx \, dy \\
&\quad + \sum_{j=1}^{n} \int_{\Omega^e} \epsilon_p \left( \frac{\partial \Psi_i}{\partial x} \frac{\partial \Psi_j}{\partial x} \right) u_j \, dx \, dy \\
&\quad + \sum_{j=1}^{n} \int_{\Omega^e} \epsilon_p \left( \frac{\partial \Psi_i}{\partial x} \frac{\partial \Psi_j}{\partial y} \right) v_j \, dx \, dy = \oint_{\Gamma^e} \Psi_i t_x d\Gamma
\end{aligned} \tag{3.25}$$

and for the *y*-momentum,

$$\sum_{j=1}^{n} \int_{\Omega^e} \Psi_i \left[ \bar{u} \frac{\partial \Psi_j}{\partial x} + \bar{v} \frac{\partial \Psi_j}{\partial y} \right] v_j \, dx \, dy + \sum_{j=1}^{n} \int_{\Omega^e} \frac{1}{Re} \left( 2 \frac{\partial \Psi_i}{\partial y} \frac{\partial \Psi_j}{\partial y} + \frac{\partial \Psi_i}{\partial x} \frac{\partial \Psi_j}{\partial x} \right) v_j \, dx \, dy + \sum_{j=1}^{n} \int_{\Omega^e} \frac{1}{Re} \left( \frac{\partial \Psi_i}{\partial x} \frac{\partial \Psi_j}{\partial y} \right) u_j \, dx \, dy + \sum_{j=1}^{n} \int_{\Omega^e} \epsilon_p \left( \frac{\partial \Psi_i}{\partial y} \frac{\partial \Psi_j}{\partial x} \right) u_j \, dx \, dy + \sum_{j=1}^{n} \int_{\Omega^e} \epsilon_p \left( \frac{\partial \Psi_i}{\partial y} \frac{\partial \Psi_j}{\partial y} \right) v_j \, dx \, dy = \oint_{\Gamma^e} \Psi_i t_y d\Gamma \tag{3.26}$$

Eqs. (3.28) and (3.29) can be written in matrix form as

$$\begin{bmatrix} [C11] & [0] \\ [0] & [C11] \end{bmatrix} \begin{Bmatrix} \{u\} \\ \{v\} \end{Bmatrix} + \begin{bmatrix} [K11] & [K12] \\ [K21] & [K22] \end{bmatrix} \begin{Bmatrix} \{u\} \\ \{v\} \end{Bmatrix} + \begin{bmatrix} [L11] & [L12] \\ [L21] & [L22] \end{bmatrix} \begin{Bmatrix} \{u\} \\ \{v\} \end{Bmatrix} = \begin{Bmatrix} \{Ru\} \\ \{Rv\} \end{Bmatrix} \tag{3.27}$$

where the matrix entries are defined as

$$[C11]_{ij} = \int_{\Omega^e} \Psi_i \left[ \bar{u} \frac{\partial \Psi_j}{\partial x} + \bar{v} \frac{\partial \Psi_j}{\partial y} \right] dx \, dy \tag{3.28}$$

$$[K11]_{ij} = \int_{\Omega^e} \frac{1}{Re}\left(2\frac{\partial \Psi_i}{\partial x}\frac{\partial \Psi_j}{\partial x} + \frac{\partial \Psi_i}{\partial y}\frac{\partial \Psi_j}{\partial y}\right) dx\, dy \tag{3.29}$$

$$[K12]_{ij} = \int_{\Omega^e} \frac{1}{Re}\left(\frac{\partial \Psi_i}{\partial y}\frac{\partial \Psi_j}{\partial x}\right) dx\, dy \tag{3.30}$$

$$[K21]_{ij} = \int_{\Omega^e} \frac{1}{Re}\left(\frac{\partial \Psi_i}{\partial x}\frac{\partial \Psi_j}{\partial y}\right) dx\, dy \tag{3.31}$$

$$[K22]_{ij} = \int_{\Omega^e} \frac{1}{Re}\left(2\frac{\partial \Psi_i}{\partial y}\frac{\partial \Psi_j}{\partial y} + \frac{\partial \Psi_i}{\partial x}\frac{\partial \Psi_j}{\partial x}\right) dx\, dy \tag{3.32}$$

$$[L11]_{ij} = \int_{\Omega^e} \left(\epsilon_p \frac{\partial \Psi_i}{\partial x}\frac{\partial \Psi_j}{\partial x}\right) dx\, dy \tag{3.33}$$

$$[L12]_{ij} = \int_{\Omega^e} \left(\epsilon_p \frac{\partial \Psi_i}{\partial x}\frac{\partial \Psi_j}{\partial y}\right) dx\, dy \tag{3.34}$$

$$[L21]_{ij} = \int_{\Omega^e} \left(\epsilon_p \frac{\partial \Psi_i}{\partial y}\frac{\partial \Psi_j}{\partial x}\right) dx\, dy \tag{3.35}$$

$$[L22]_{ij} = \int_{\Omega^e} \left(\epsilon_p \frac{\partial \Psi_i}{\partial y}\frac{\partial \Psi_j}{\partial y}\right) dx\, dy \tag{3.36}$$

$$\{Ru\} = \oint_{\Gamma^e} \Psi_i t_x \, d\Gamma \tag{3.37}$$

$$\{Rv\} = \oint_{\Gamma^e} \Psi_i t_y \, d\Gamma \tag{3.38}$$

According to the reduced integration penalty finite element method, the [L] matrices, which are related to the penalty term, are calculated with one order less Gauss quadrature points than other matrices. For example, if 3x3 Gauss quadrature points are used to calculate the [C] and [K] matrices, then 2x2 Gauss quadrature points are used to calculate the [L] matrices.

### 3.3.2 – Formulation of the Energy Equation:

A similar procedure like the formulation of momentum equations should be followed for the formulation of energy equation. First, all nonzero expressions in the open form of the energy equation are taken to one side of the equality sign and the resulting equation is multiplied with a weight function $\delta T_i$. Then the equation is integrated over the element domain $\Omega^e$ to obtain the weighted integral statement of the equation.

$$\int_{\Omega^e} \delta T_i \left[ \left( u\frac{\partial \theta}{\partial x} + v\frac{\partial \theta}{\partial y} \right) - \frac{1}{Pe}\left( \frac{\partial^2 \theta}{\partial x^2} + \frac{\partial^2 \theta}{\partial y^2} \right) - 2\frac{Br}{Pe}\left[ \left( \frac{\partial u}{\partial x} \right)^2 + \left( \frac{\partial v}{\partial y} \right)^2 + \frac{1}{2}\left( \frac{\partial v}{\partial x} + \frac{\partial u}{\partial y} \right)^2 - \frac{1}{3}\left( \frac{\partial u}{\partial x} + \frac{\partial v}{\partial y} \right)^2 \right] \right] dx\, dy = 0 \tag{3.39}$$

Next, integration by parts is applied to the second order derivatives to equally distribute the integration between the dependent variable and weight function in the second order partial derivatives which yields,

$$\int_{\Omega^e} \delta T_i \left[ u\frac{\partial \theta}{\partial x} + v\frac{\partial \theta}{\partial y} \right] dx\, dy$$

$$+ \frac{1}{Pe}\left\{ \int_{\Omega^e} \left( \frac{\partial \delta T_i}{\partial x}\frac{\partial \theta}{\partial x} + \frac{\partial \delta T_i}{\partial y}\frac{\partial \theta}{\partial y} \right) dx\, dy \right.$$

$$\left. - \oint_{\Gamma^e} \delta T_i \left( \frac{\partial \theta}{\partial x} n_x + \frac{\partial \theta}{\partial y} n_y \right) d\Gamma \right\} \qquad (3.40)$$

$$- 2\frac{Br}{Pe}\left\{ \int_{\Omega^e} \delta T_i \left[ \left( \frac{\partial u}{\partial x} \right)^2 + \left( \frac{\partial v}{\partial y} \right)^2 + \frac{1}{2}\left( \frac{\partial v}{\partial x} + \frac{\partial u}{\partial y} \right)^2 \right. \right.$$

$$\left. \left. - \frac{1}{3}\left( \frac{\partial u}{\partial x} + \frac{\partial v}{\partial y} \right)^2 \right] dx\, dy \right\} = 0$$

Substituting the shape (approximation) functions, $\psi_i$, for the non-dimensional velocity components, temperature, and the weight function, $\delta T_i$,

$$u = \sum_{j=1}^{n} u_j \Psi_j(x,y) \quad , \qquad v = \sum_{j=1}^{n} v_j \Psi_j(x,y)$$

$$\theta = \sum_{j=1}^{n} \theta_j \Psi_j(x,y) \quad , \qquad \delta T_i = \Psi_i \qquad (3.41)$$

where $n$ is the total node number used in the computational element, into the Eq. (3.40), gives for the energy equation,

$$\sum_{j=1}^{n} \int_{\Omega^e} \Psi_i \left[ \left(\Psi_j u_j\right) \frac{\partial \Psi_j}{\partial x} + \left(\Psi_j v_j\right) \frac{\partial \Psi_j}{\partial y} \right] \theta_j \, dx \, dy$$

$$+ \sum_{j=1}^{n} \int_{\Omega^e} \frac{1}{Pe} \left( \frac{\partial \Psi_i}{\partial x} \frac{\partial \Psi_j}{\partial x} + \frac{\partial \Psi_i}{\partial y} \frac{\partial \Psi_j}{\partial y} \right) \theta_j \, dx \, dy$$

$$- \sum_{j=1}^{n} \int_{\Omega^e} 2 \frac{Br}{Pe} \Psi_i \left[ \left( \frac{\partial \Psi_j}{\partial x} u_j \right)^2 + \left( \frac{\partial \Psi_j}{\partial y} v_j \right)^2 \right. \tag{3.42}$$

$$\left. + \frac{1}{2} \left( \frac{\partial \Psi_j}{\partial x} v_j + \frac{\partial \Psi_j}{\partial y} u_j \right)^2 - \frac{1}{3} \left( \frac{\partial \Psi_j}{\partial x} u_j + \frac{\partial \Psi_j}{\partial y} v_j \right)^2 \right]$$

$$= \oint_{\Gamma^e} \frac{1}{Pe} \Psi_i q_n \, d\Gamma$$

where

$$q_n = \frac{\partial \theta}{\partial x} n_x + \frac{\partial \theta}{\partial y} n_y \tag{3.43}$$

Eq. (3.42) can also be written in matrix form as,

$$[KT1]\{\theta\} - \{KT2\} = \{Rt\} \tag{3.44}$$

where

$$[KT1]_{ij} = \int_{\Omega^e} \left( \Psi_i \left[ \left(\Psi_j u_j\right) \frac{\partial \Psi_j}{\partial x} + \left(\Psi_j v_j\right) \frac{\partial \Psi_j}{\partial y} \right] \right. \tag{3.45}$$

$$\left. + \frac{1}{Pe} \left[ \frac{\partial \Psi_i}{\partial x} \frac{\partial \Psi_j}{\partial x} + \frac{\partial \Psi_i}{\partial y} \frac{\partial \Psi_j}{\partial y} \right] \right) dx \, dy$$

$$\{KT2\}_i = \int_{\Omega^e} 2\frac{Br}{Pe}\Psi_i \left[\left(\frac{\partial \Psi_j}{\partial x}u_j\right)^2 + \left(\frac{\partial \Psi_j}{\partial y}v_j\right)^2 + \frac{1}{2}\left(\frac{\partial \Psi_j}{\partial x}v_j + \frac{\partial \Psi_j}{\partial y}u_j\right)^2 - \frac{1}{3}\left(\frac{\partial \Psi_j}{\partial x}u_j + \frac{\partial \Psi_j}{\partial y}v_j\right)^2\right] dx\, dy \tag{3.46}$$

$$\{Rt\} = \oint_{\Gamma^e} \frac{1}{Pe}\Psi_i q_n d\Gamma \tag{3.47}$$

### 3.3.3 – Numerical Integration:

In this study, numerical integrations are carried out by Gauss quadrature. Quadrilateral elements with 4 nodes (shown in Fig. 3.4) are used as the master computational element. In this element, elemental node numbering is in counterclockwise direction and node coordinates are defined by means of elemental local coordinate system, $\xi$ and $\eta$. The shape functions related to this computational element are tabulated in literature and also given here in Eq. (3.48).

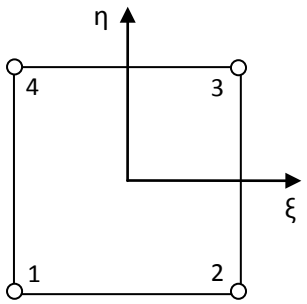


Figure 3.4: Quadrilateral element with 4 nodes as master computational element.

$$\Psi_1 = \frac{1}{4}(1-\xi)(1-\eta) \qquad \Psi_3 = \frac{1}{4}(1+\xi)(1+\eta)$$
$$\Psi_2 = \frac{1}{4}(1+\xi)(1-\eta) \qquad \Psi_4 = \frac{1}{4}(1-\xi)(1+\eta) \tag{3.48}$$

It is necessary to evaluate the derivatives of the shape functions with respect to global coordinates *x* and *y*, to numerically integrate these equations. Since shape functions are defined with local coordinates $(\xi, \eta)$, transformation of the geometry from global coordinates (*x, y*) to computational coordinates $(\xi, \eta)$ is needed. This is done by defining,

$$x = \sum_{j=1}^{n} x_j \Psi_j(\xi, \eta) \qquad y = \sum_{j=1}^{n} y_j \Psi_j(\xi, \eta) \tag{3.49}$$

Then, the derivatives of shape functions with respect to *x* and *y*, can be expressed in terms of local coordinates $(\xi, \eta)$ by means of this transformation. With the chain rule of partial differentiation, the first derivatives of the shape functions with respect to local coordinates can be written as in matrix form;

$$\begin{Bmatrix} \frac{\partial \Psi_j}{\partial \xi} \\ \frac{\partial \Psi_j}{\partial \eta} \end{Bmatrix} = \begin{bmatrix} \frac{\partial x}{\partial \xi} & \frac{\partial y}{\partial \xi} \\ \frac{\partial x}{\partial \eta} & \frac{\partial y}{\partial \eta} \end{bmatrix} \begin{Bmatrix} \frac{\partial \Psi_j}{\partial x} \\ \frac{\partial \Psi_j}{\partial y} \end{Bmatrix} = [\mathcal{J}] \begin{Bmatrix} \frac{\partial \Psi_j}{\partial x} \\ \frac{\partial \Psi_j}{\partial y} \end{Bmatrix}$$

$$\begin{Bmatrix} \frac{\partial \Psi_j}{\partial x} \\ \frac{\partial \Psi_j}{\partial y} \end{Bmatrix} = [\mathcal{J}]^{-1} \begin{Bmatrix} \frac{\partial \Psi_j}{\partial \xi} \\ \frac{\partial \Psi_j}{\partial \eta} \end{Bmatrix} \tag{3.50}$$

where $[\mathcal{J}]$ is the *Jacobian matrix* of the transformation and calculated by,

$$[\mathcal{J}] = \begin{bmatrix} \frac{\partial x}{\partial \xi} & \frac{\partial y}{\partial \xi} \\ \frac{\partial x}{\partial \eta} & \frac{\partial y}{\partial \eta} \end{bmatrix} = \begin{bmatrix} \sum_{j=1}^{n} x_j \frac{\partial \Psi_j}{\partial \xi} & \sum_{j=1}^{n} y_j \frac{\partial \Psi_j}{\partial \xi} \\ \sum_{j=1}^{n} x_j \frac{\partial \Psi_j}{\partial \eta} & \sum_{j=1}^{n} y_j \frac{\partial \Psi_j}{\partial \eta} \end{bmatrix}$$

$$[\mathcal{J}] = \begin{bmatrix} \frac{\partial \Psi_1}{\partial \xi} & \frac{\partial \Psi_2}{\partial \xi} \dots\dots \frac{\partial \Psi_n}{\partial \xi} \\ \frac{\partial \Psi_1}{\partial \eta} & \frac{\partial \Psi_2}{\partial \eta} \dots\dots \frac{\partial \Psi_n}{\partial \eta} \end{bmatrix} \begin{bmatrix} x_1 & y_1 \\ x_2 & y_2 \\ \vdots & \vdots \\ x_n & y_n \end{bmatrix} \tag{3.51}$$

### 3.3.4 – Imposing Boundary Conditions and Solution of the System Equation:

Evaluation of boundary integrals (line integrals) $\{Ru\}$, $\{Rv\}$, and $\{Rt\}$ in Eqs. (3.37), (3.38), and (3.47) respectively, depends on the boundary conditions of the problem. Three types of boundary conditions are generally used in numerical simulations. These are Dirichlet (essential), Neumann (natural), and mixed boundary conditions.

If a Dirichlet type boundary condition, that is specified primary variables (specified velocity for momentum equations and specified temperature for energy

equation), is defined on a boundary, then it is not necessary to calculate the boundary integral on that boundary node. When this type of a boundary condition is defined on a boundary, specified value of the variable is directly placed into the appropriate location of the unknown vector after assembling the system equations. For example, consider an arbitrary system of equations with unknown primary variables $\{u\}$ and secondary variables $\{Ru\}$.

$$\begin{bmatrix} k_{11} & k_{12} & \dots & k_{1j} & \dots & k_{1n} \\ k_{21} & k_{22} & \dots & k_{2j} & \dots & k_{2n} \\ \vdots & \vdots & & \vdots & & \vdots \\ k_{j1} & k_{j2} & \dots & k_{jj} & \dots & k_{jn} \\ \vdots & \vdots & & \vdots & & \vdots \\ k_{n1} & k_{n2} & \dots & k_{jj} & \dots & k_{nn} \end{bmatrix} \begin{Bmatrix} u_1 \\ u_2 \\ \vdots \\ u_j \\ \vdots \\ u_n \end{Bmatrix} = \begin{Bmatrix} Ru_1 \\ Ru_2 \\ \vdots \\ Ru_j \\ \vdots \\ Ru_n \end{Bmatrix}$$

If $u$ is specified as $U$ at global node $j$ ($u_j=U$), after the assembling of elemental equations are completed, the $j^{th}$ row of the unknown vector $\{u\}$ is replaced by $k$. Then, this system of equations can be solved by modifying the $\{Ru\}$ vector and reducing the system by deleting the $j^{th}$ row and column of $[k_{ij}]$ matrix as

$$\begin{bmatrix} k_{11} & k_{12} & \dots & 0 & \dots & k_{1n} \\ k_{21} & k_{22} & \dots & 0 & \dots & k_{2n} \\ \vdots & \vdots & & \vdots & & \vdots \\ 0 & 0 & \dots & 1 & \dots & 0 \\ \vdots & \vdots & & \vdots & & \vdots \\ k_{n1} & k_{n2} & \dots & 0 & \dots & k_{nn} \end{bmatrix} \begin{Bmatrix} u_1 \\ u_2 \\ \vdots \\ U \\ \vdots \\ u_n \end{Bmatrix} = \begin{Bmatrix} Ru_1 - Uk_{1j} \\ Ru_2 - Uk_{2j} \\ \vdots \\ Ru_j \\ \vdots \\ Ru_n - Uk_{nj} \end{Bmatrix}$$

When a Neumann type boundary condition, that is, specified secondary variables at the boundary, is defined, the solution depends on the specified value. In general, the boundary integral can be written as

$$\oint_{\Gamma} a_n \Psi^{\mathrm{T}} \frac{\partial \mathrm{u}}{\partial \mathrm{n}} \ell_{\mathrm{n}} \, \mathrm{d}\Gamma \tag{3.52}$$

where $\Gamma$ is the length of the boundary, $\ell_{\mathrm{n}}$ is the direction cosine of the surface normal and $a_n$ is a constant. If the secondary variable is zero at the boundary, i.e., zero heat flux or geometrical symmetry, that is $\frac{\partial u}{\partial n} = 0$ , then the boundary integral vanishes. If the secondary variable is given as a constant such as, $\frac{\partial u}{\partial n} = C$, it gives an extra vector,

$$\oint_{\Gamma} a_n \Psi^{\mathrm{T}} \mathrm{C} \ell_{\mathrm{n}} \, \mathrm{d}\Gamma \tag{3.53}$$

which must be added to the $\{Ru\}$ vector [67].

However, if a slip velocity, temperature jump, or another mixed type boundary condition, such as convection boundary condition, is defined on a boundary, then, this boundary integral needs some modification, which leads to a matrix associated to the unknown primary variable and a vector consisting of known parameters. For momentum equations, the boundary integrals are equivalent to

$$R_i = \oint_{\Gamma^e} \Psi_i \sigma_{ij} n_j \, d\Gamma \tag{3.54}$$

When slip velocity is defined at the boundary, tangential Dirichlet type boundary condition should be replaced by traction boundary conditions by setting

$$\sigma_{ij} n_j t_i = \frac{1}{\alpha}(u_i - u_i^s) t_i \tag{3.55}$$

where $t_i$ is the tangent vector to the surface, $\alpha$ is the slip coefficient, and $u_i^s$ is the velocity of the surface [66]. By doing this, a boundary matrix and a boundary vector arise, such that

$$R_i = \int_{\Omega^e} \frac{1}{\alpha} \Psi_i u_i \, t_i \, dx \, dy - \oint_{\Gamma^e} \frac{1}{\alpha} \Psi_i u_i^s t_i \, d\Gamma \tag{3.56}$$

When this modification is applied to Eq. (3.12) with zero surface velocity, a simpler boundary condition is obtained, which yields only a boundary matrix that can be expressed in general as

$$\frac{\partial u}{\partial n} = Cu \tag{3.57}$$

and

$$\oint_{\Gamma} a_n \Psi^{\mathrm{T}} \mathrm{C} \, \mathrm{u} \, \ell_{\mathrm{n}} \, \mathrm{d}\Gamma \tag{3.58}$$

A similar procedure should be applied to the temperature jump boundary condition. Since these boundary integrals are evaluated along the edge of the elements in two dimensional problems, they reduce to line integrals. Thus one dimensional shape functions should be used instead of two dimensional shape functions.

After assembling and imposing the boundary conditions, the system of equations can be solved. Since the Navier-Stokes equations are non-linear, an iterative solution procedure is needed. In this study Picard method, which is also known as the direct iteration method [65] is used. In this method, equation system is first

solved with an initial value assigned to the unknown primary variables. Then, the new values of the primary variables are compared with the old ones. If the difference between the new and old values is below the error (convergence) criterion, iteration stops. If not, iteration continues using the last found values until the error criterion satisfied. This algorithm can be given as,

$$\mathbf{K}(\Delta^r)\Delta^{r+1} = \mathbf{F} \tag{3.59}$$

where $\Delta$ is the unknown vector, $\boldsymbol{K}(\Delta)$ is the non-linear matrix, and the superscript $r$ indicates the iteration number. As the error criterion Euclidean norm is used in the form of

$$\frac{|\Delta^{r+1} - \Delta^r|}{|\Delta^{r+1}|} < \varepsilon \tag{3.60}$$

where $\varepsilon$ is error criterion and it is set to be $10^{-3}$ in this study.

# CHAPTER – 4

# RESULTS AND DISCUSSION

Results of numerical simulations for smooth and rough geometries are given in this chapter and findings are discussed. Additionally, information about mesh generation and mesh convergence studies are given in related subsections. Numerical simulations have been conducted for flow of air ($Pr$ = 0.7, $\gamma$ = 1.4) between two parallel plates having $Re$ of 5, 10, 20, 50, and 100, which leads the $Pe$ of 3.5, 7, 14, 35, and 70. Considered relative roughness values of the channel are 0%, 1.325%, 2.0% and 2.65%. However 2.65% relative roughness is considered only in continuum case. To simulate the rarefaction effects, velocity slip and temperature jump boundary conditions have been applied at channel solid boundaries as described in Chapter 3. While applying these boundary conditions, $Kn$ of 0.0 (continuum case), 0.02, 0.04, 0.06, 0.08, and 0.10 have been considered. Moreover, effect of viscous dissipation on heat transfer has been investigated by the change of $Br$, where considered $Br$ values are – 0.1, 0.0, and +0.1. Also, all the cases have been repeated for both considering and neglecting the axial conduction term in the energy equation.

## 4.1 – Code Validation and Mesh Convergence Studies:

The meshes used in the simulations of two-dimensional flow in smooth and rough parallel plate channels are generated by a mesh generator program written in

MATLAB by the author of this study. This program is capable of preparing different kinds of meshes, such as uniform mesh in whole geometry, dense mesh near boundaries or mesh with gradually increasing element size at inlet and gradually decreasing element size at outlet in *x*-direction, and the necessary boundary condition data for inlet, outlet, lower and upper walls in smooth and rough channels. Also, user can specify the roughness peak heights, distance between the peaks, base angle of the triangular peaks, and number of elements that should be used in one side of the triangles, and between two triangular peaks. Some examples of meshes generated by this program are given in Fig. (4.1).

Code validation and mesh convergence studies for hydraulic part have been conducted in smooth channels for the upper *Re* limit of this study by comparing the non-dimensional velocity profiles with the analytical results of hydrodynamically fully developed case. For the smooth channel and coordinate system considered in this study, the fully developed non-dimensional velocity profile can be obtained from momentum equation as

$$\frac{u(y)}{u_m} = 6\,\frac{\left[\left(\frac{y}{H}\right) - \left(\frac{y}{H}\right)^2 + Kn\right]}{[1 + 6\,Kn]} \tag{4.1}$$

For the energy part of the problem, obtained fully developed *Nu* values have been compared with the results of Refs. [6] and [24] for the cases where axial conduction in the fluid is neglected, and with the results of Refs. [17, 18] and [68] for the cases where axial conduction in the fluid is considered.

Detailed mesh convergence studies have been conducted with various mesh sizes and types, such as uniform mesh, dense mesh near boundaries with different dense region length and element number, and mesh with gradually increasing element size in $x$ – direction. During these studies, from 200 to 720 elements in $x$ – direction, and from 60 to 100 elements in $y$ – direction have been tried. Purpose of

this study is to obtain maximum accuracy with minimum element number as well as obtaining a mesh independent solution. It is observed that, *Nu* is more dependent to the mesh size and type than the non-dimensional velocity profile.

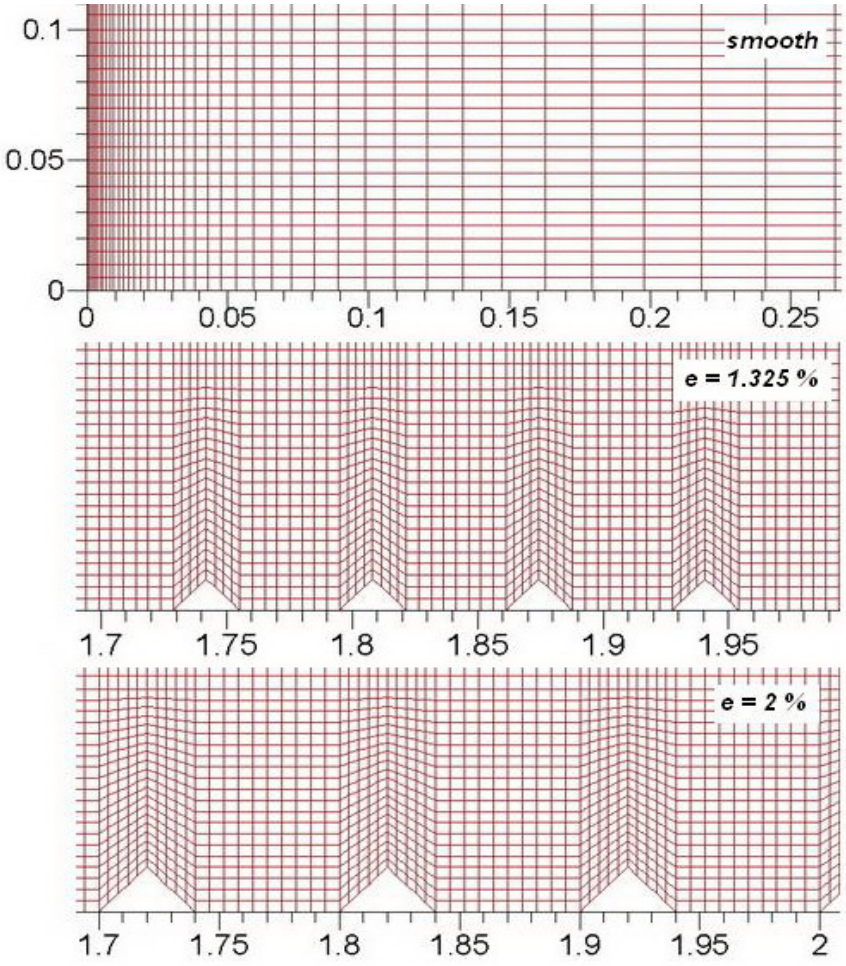


Figure 4.1: Mesh examples for smooth and rough channels with 1.325% and 2.0% relative roughness.

Although good results for the non-dimensional velocity can be obtained with a coarse mesh, a finer mesh is needed to obtain accurate *Nu*. Moreover, it is also observed that mesh type at inlet section affects the smoothness of the results at this section more, compared to other parts of the channel. Best results with minimum element number are obtained by using elements with gradually increasing sizes at inlet, and dense mesh near the solid boundaries and coarser mesh inside the channel. Finally, during the smooth channel simulations, 408 elements in $x$ – direction and 90 elements in $y$ – direction is used.

For the rough channel, mesh is also refined around the triangular peaks. Meshes with 2 to 10 elements on one side of the peaks and 2 to 20 elements between the peaks have been tried and change in *Nu* distribution is observed. Then, 4, 5, and 7 elements on one side of the peaks, and 8, 10, and 16 elements between the peaks are used in the rough channel simulations for relative roughnesses of 1.325%, 2.0%, and 2.65% respectively.

### 4.2 – Results for Smooth Channel:

As can be seen from Eq. (4.1), fully developed velocity profile depends on the *Kn* and is shown graphically in Fig. (4.2). *Re* only affects the development length and as it increases, flow reaches fully developed state at a distance far away from the inlet section. When $Kn = 0$, flow is in macro-scale and rarefaction effects are neglected. $Kn = 0.10$ is the upper limit of the slip flow regime and naturally, rarefaction effects are maximum in this regime. As *Kn* increases from 0 to 0.10, rarefaction effect increases as well as the slip velocity at the wall, which reduces the maximum velocity at the center line and velocity gradient at the wall. The reduction in velocity gradient at the wall also causes reduction in the friction factor. As *Kn* increases from 0 to 0.10, non-dimensional centerline velocity decreases from 1.5 to 1.3125, and non-dimensional velocity of the fluid particles

at the wall increases from 0 to 0.375. Analytical non-dimensional velocities at the wall and centerline are also tabulated in Table (4.1).

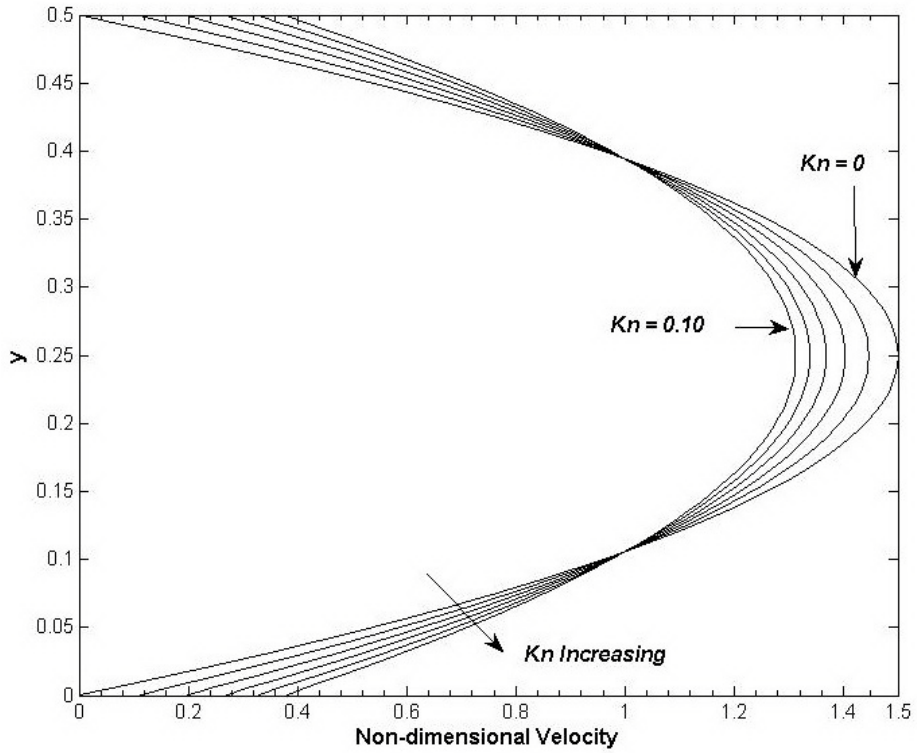


Figure 4.2: Non-dimensional fully developed velocity profile inside the parallel – plate microchannel.

Table 4.1: Analytical non-dimensional velocities at wall and centerline for various *Kn* values.

| ***Kn*** | **0.00** | **0.02** | **0.04** | **0.06** | **0.08** | **0.10** |
|---|---|---|---|---|---|---|
| **Velocity at Wall:** | 0 | 0.1071 | 0.1935 | 0.2647 | 0.3243 | 0.375 |
| **Centerline Velocity:** | 1.5 | 1.4464 | 1.4032 | 1.3676 | 1.3378 | 1.3125 |

As described in Chapter 3, energy equation is solved after obtaining the velocity profile from Navier-Stokes equations. When temperature distribution is obtained from the energy equation, local *Nu* values are obtained from Eq. (3.13). As *Kn* increases, temperature jump at the wall increases as well, which reduces the temperature gradient at the wall. This reduction should also cause a decrease in *Nu*. When axial conduction (AC) in the fluid is neglected non-dimensional centerline temperature decreases from 1.3191 to 1.2246, and non-dimensional wall temperature increases from 0 to 0.4216 as *Kn* increases from 0 to 0.10, regardless of *Re*. However, when axial conduction in the fluid is considered, non-dimensional wall and centerline temperatures show slight dependence on *Re*. For small *Re*, non-dimensional wall temperatures are slightly higher while non-dimensional centerline temperatures are slightly lower compared to cases where axial conduction is neglected. These are summarized in Table (4.2). It is observed that mean temperatures of cases where axial conduction is included are higher than cases where axial conduction is neglected, at the inlet section of the channel. This difference is more obvious for small *Re*, where axial conduction becomes important. Similar behavior is observed when viscous dissipation effect is considered. As a result, axial conduction should not be neglected for flows with small *Pe* in entrance region problems.

Figures (4.3) and (4.4) show the local *Nu* along the channel when viscous dissipation is neglected for various *Kn* and *Pe*, without and with axial conduction effect, respectively. When axial conduction is neglected, local *Nu* values show dependence on *Pe* at the inlet section of the channel, and increases with increasing *Pe*. However, *Nu* reaches the same fully developed value for each *Kn* regardless of *Pe*, that is 7.541 for $Kn = 0$ and 5.059 for $Kn = 0.10$. It is also observed that as *Kn* increases, rarefaction effect increases and this causes reduction on local and fully developed *Nu* values. Comparison of fully developed *Nu* values, when axial conduction effect is neglected, with Ref. [24] is given in Table (4.3).

Table 4.2: Dimensionless fully developed wall and centerline temperatures for various *Kn* and *Re* with and without axial conduction in the fluid (*Br* = 0).

| | ***Kn*** | **0.00** | **0.02** | **0.04** | **0.06** | **0.08** | **0.10** |
|---|---|---|---|---|---|---|---|
| **Wall Temperature** | | | | | | | |
| with AC: | Re = 5 | 0 | 0.1230 | 0.2254 | 0.3103 | 0.3808 | 0.4398 |
| | Re = 100 | 0 | 0.1161 | 0.2136 | 0.2955 | 0.3645 | 0.4230 |
| without AC: | Re = 5 | 0 | 0.1155 | 0.2125 | 0.2941 | 0.3631 | 0.4216 |
| | Re = 100 | 0 | 0.1155 | 0.2125 | 0.2941 | 0.3631 | 0.4216 |
| **Centerline Temperature** | | | | | | | |
| with AC: | Re = 5 | 1.2961 | 1.2766 | 1.2566 | 1.2376 | 1.2203 | 1.2048 |
| | Re = 100 | 1.3169 | 1.2978 | 1.2776 | 1.2580 | 1.2398 | 1.2231 |
| without AC: | Re = 5 | 1.3191 | 1.2999 | 1.2796 | 1.2599 | 1.2415 | 1.2246 |
| | Re = 100 | 1.3191 | 1.2999 | 1.2796 | 1.2599 | 1.2415 | 1.2246 |

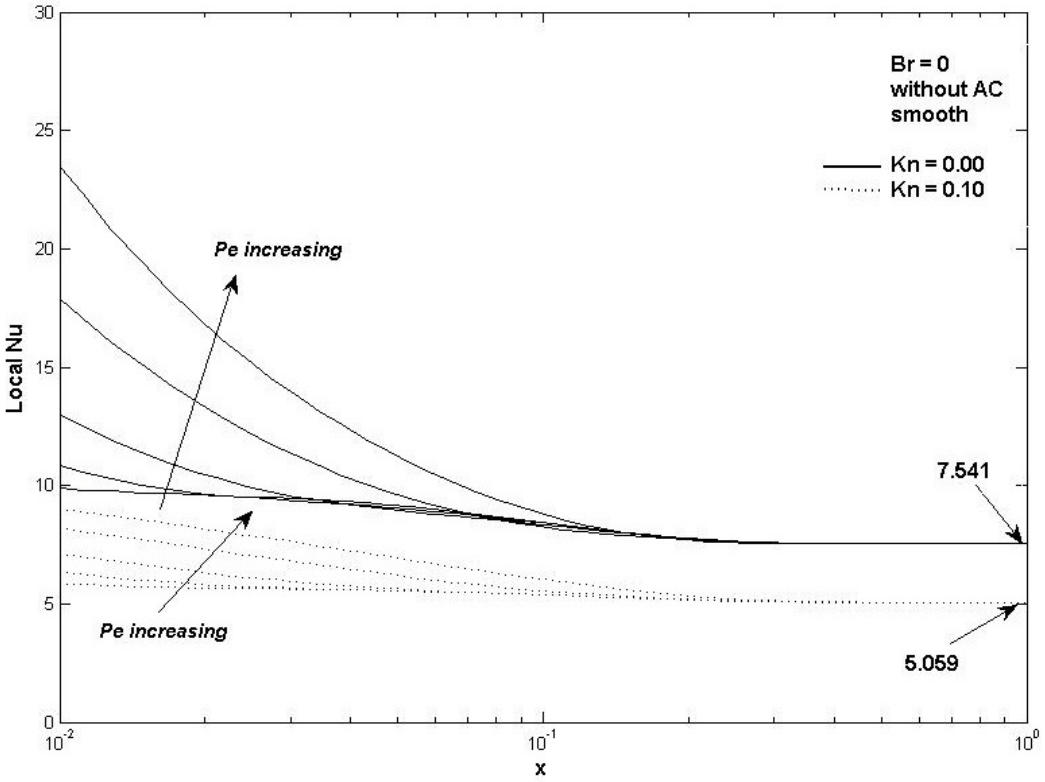


Figure 4.3: Local *Nu* along the channel for various *Kn* and *Pe* when axial conduction and viscous dissipation are neglected.

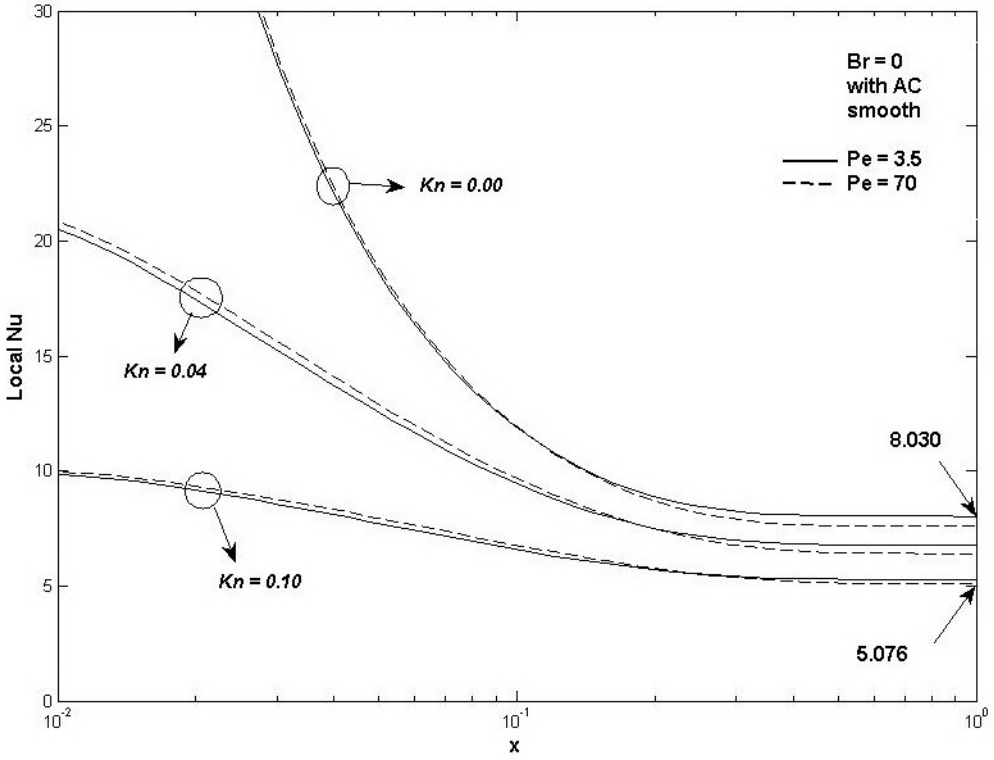


Figure 4.4: Local *Nu* along the channel for various *Kn* and *Pe* when axial conduction included and viscous dissipation neglected.

Table 4.3: Comparison of fully developed *Nu* values for smooth channel with Ref. [24] (axial conduction neglected).

| | **Without Viscous Dissipation ( Br = 0)** | | **Deviation (%)** | **With Viscous Dissipation (Br ≠ 0)** | | **Deviation (%)** |
|---|---|---|---|---|---|---|
| ***Kn*** | **Nu** | **Nu [24]** | | **Nu** | **Nu [24]** | |
| **0.00** | 7.541 | 7.541 | 0.000 | 17.485 | 17.497 | 0.068 |
| **0.02** | 6.926 | 6.925 | 0.014 | 13.679 | 13.688 | 0.066 |
| **0.04** | 6.374 | 6.374 | 0.000 | 11.215 | 11.222 | 0.062 |
| **0.06** | 5.883 | 5.882 | 0.017 | 9.493 | 9.499 | 0.063 |
| **0.08** | 5.446 | 5.445 | 0.018 | 8.224 | 8.229 | 0.061 |
| **0.10** | 5.059 | 5.058 | 0.020 | 7.251 | 7.256 | 0.069 |

When axial conduction is included, dependence of *Nu* on *Pe* is very small. Unlike the neglected axial conduction cases, local *Nu* does not change too much with *Pe* and takes higher values at the inlet section. Also, local *Nu* drop more sharply when axial conduction is considered. Moreover, fully developed *Nu* values show slight dependence on *Pe* and take different values for each *Pe* and *Kn*. Comparison of fully developed *Nu* values with Refs. [17] and [68] is given in Fig. (4.5). Also, fully developed *Nu* values are summarized in Table (4.4) for various *Pe* and *Kn* when axial conduction is included.

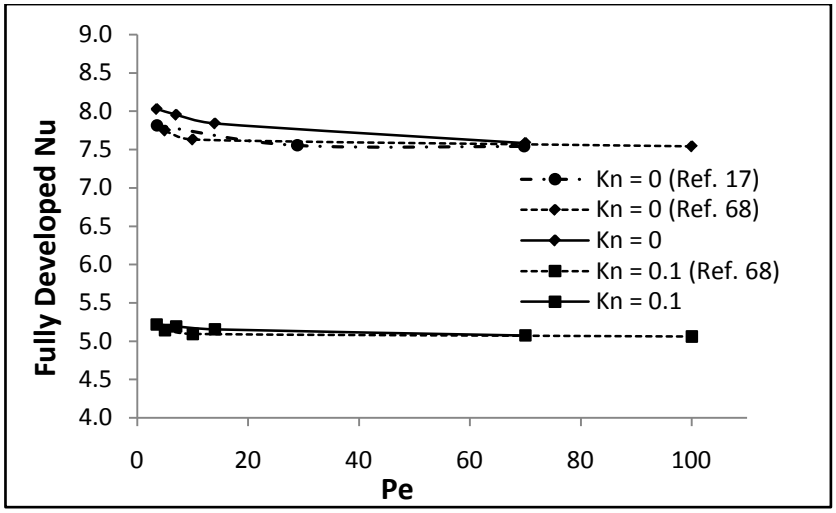


Figure 4.5: Comparison of fully developed *Nu* values for smooth channel with Refs. [17] and [68] (axial conduction included, *Br* = 0).

Table 4.4: Fully developed *Nu* for smooth channel for various *Re* and *Kn* (axial conduction included, *Br* = 0).

| ***Kn* \ *Pe*** | **3.5** | **7** | **14** | **35** | **70** |
|---|---|---|---|---|---|
| **0.00** | 8.030 | 7.955 | 7.841 | 7.668 | 7.586 |
| **0.02** | 7.378 | 7.307 | 7.200 | 7.041 | 6.966 |
| **0.04** | 6.762 | 6.701 | 6.607 | 6.470 | 6.408 |
| **0.06** | 6.206 | 6.154 | 6.075 | 5.961 | 5.909 |
| **0.08** | 5.713 | 5.669 | 5.603 | 5.509 | 5.467 |
| **0.10** | 5.278 | 5.241 | 5.186 | 5.109 | 5.076 |

Variation of local *Nu* along the channel for various *Kn* and *Br* is given in Fig. (4.6). When viscous dissipation effect is included, increase in fully developed *Nu* values is observed. *Nu* reaches the same values for each *Kn* regardless of *Pe* or the sign of *Br*. For *Br* = ± 0.1, fully developed *Nu* increases to 17.485 from 7.541 for *Kn* = 0, and to 7.251 from 5.059 for *Kn* = 0.10 when axial conduction is neglected. When axial conduction is included, no significant change is observed in fully developed *Nu* values. However, effect of axial conduction changes the local *Nu* variation at the inlet section similar to cases where viscous dissipation is neglected and is more obvious at small *Pe* as expected. Also, when *Br* = - 0.1, there exist some asymptotic local *Nu* inside the channel, which are generally referred in literature to points where direction of the heat transfer between wall and fluid changes. Location of these values along the channel depends on *Kn* and *Pe*.

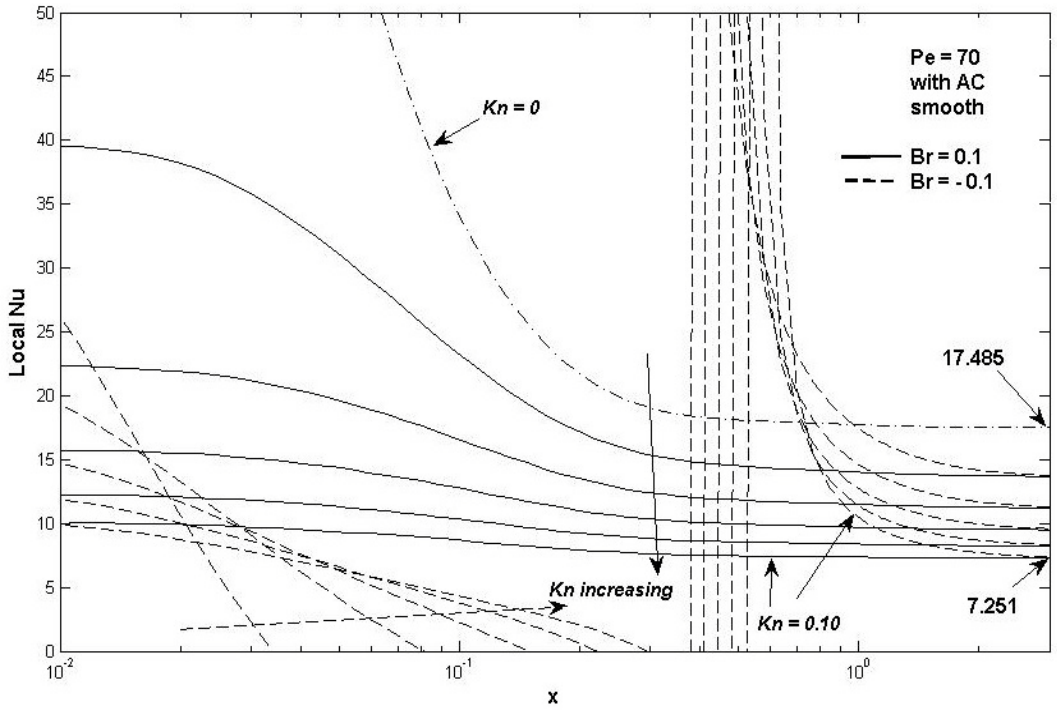


Figure 4.6: Local *Nu* along the channel for various *Kn* and *Br* values and *Pe* = 70.

### 4.3 – Results for Rough Channel:

For the rough channel, velocity contours are examined first, since the solution of the energy equation strictly depends on the velocity profile. Then, obtained *Nu* values are compared. In Fig. (4.7), contour plots for dimensionless *u*-velocity around roughness elements and smooth channel for *Kn* = 0 and *Re* = 100 are shown. Since rarefaction effects are neglected, it is observed that the increase in *Re* only affects the velocity contour at inlet section. Also, increase in roughness height reduces the low velocity layer thickness over the peaks of roughness elements. Theoretically, flow field should look like to the smooth channel flow case as the roughness height become smaller, and low velocity layer thickness over the roughness elements should decrease as the roughness height increases. To verify this, contour plots of dimensionless *u*-velocity around the roughness

elements for relative roughnesses of 0.1%, 0.5%, and 10% are also included to Fig. (4.7).

In literature, there are a few publications, which give the local *Nu* distribution in a rough microchannel with triangular roughness elements. In Ref. [50], Croce and D'Agaro conducted numerical simulations with randomly generated triangular and square roughness elements on the wall of tube and parallel plate channel with periodic boundary conditions. They do not consider the rarefaction effect. However, they showed the local *Nu* distribution over triangular roughness elements only for microtube with 2.65 % relative roughness, which is given in Fig. (4.8a), and stated that the general distribution of local *Nu* is similar, except it takes higher values for parallel plate channel. Local *Nu* distribution inside the rough channels considered in this study for $Kn = 0$ are shown in Fig. (4.8), along with the results of Croce and D'Agaro [50]. Obtained local *Nu* distribution have similar pattern of Ref. [50].

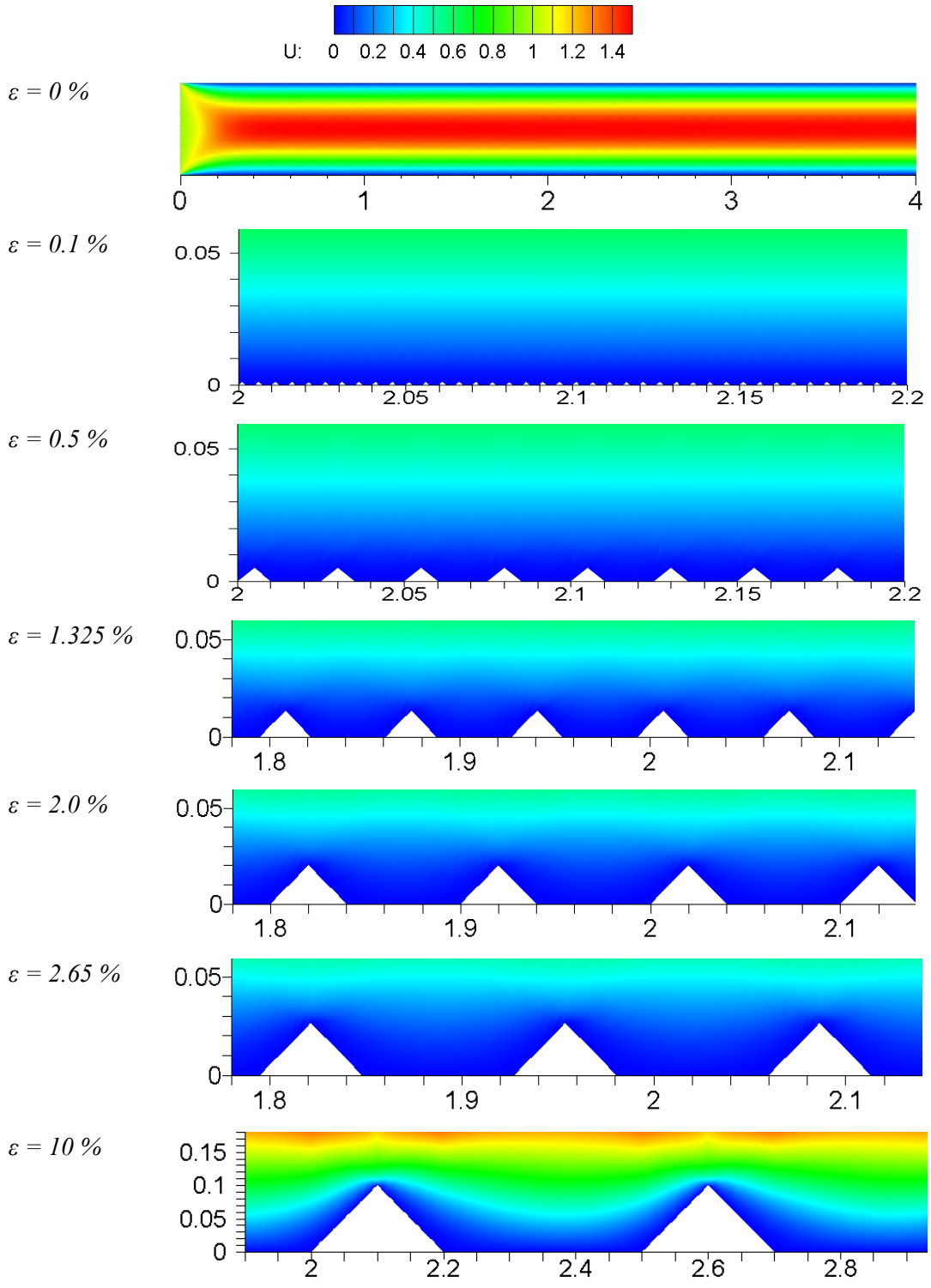


Figure 4.7: Dimensionless u-velocity contours along the smooth channel and between the roughness elements for $Kn = 0$ and $Re = 100$.

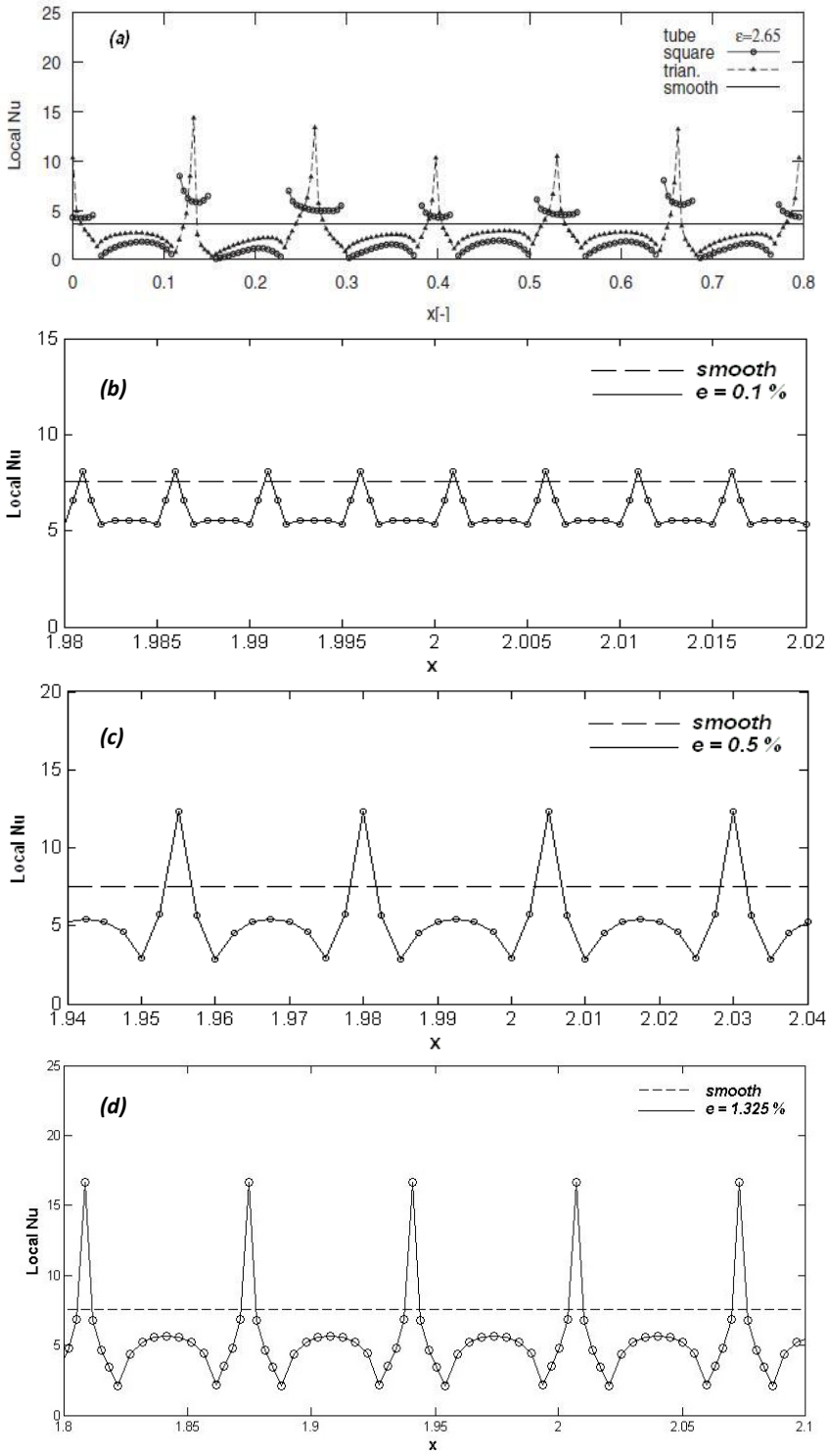


Figure 4.8: Local *Nu* distributions over the roughness elements (*Kn*=0) (a) Ref. [50] (b) ε=0.1% (c) ε=0.5% (d) ε=1.325% (e) ε=2.0% (f) ε=2.65% (g) ε=10%.

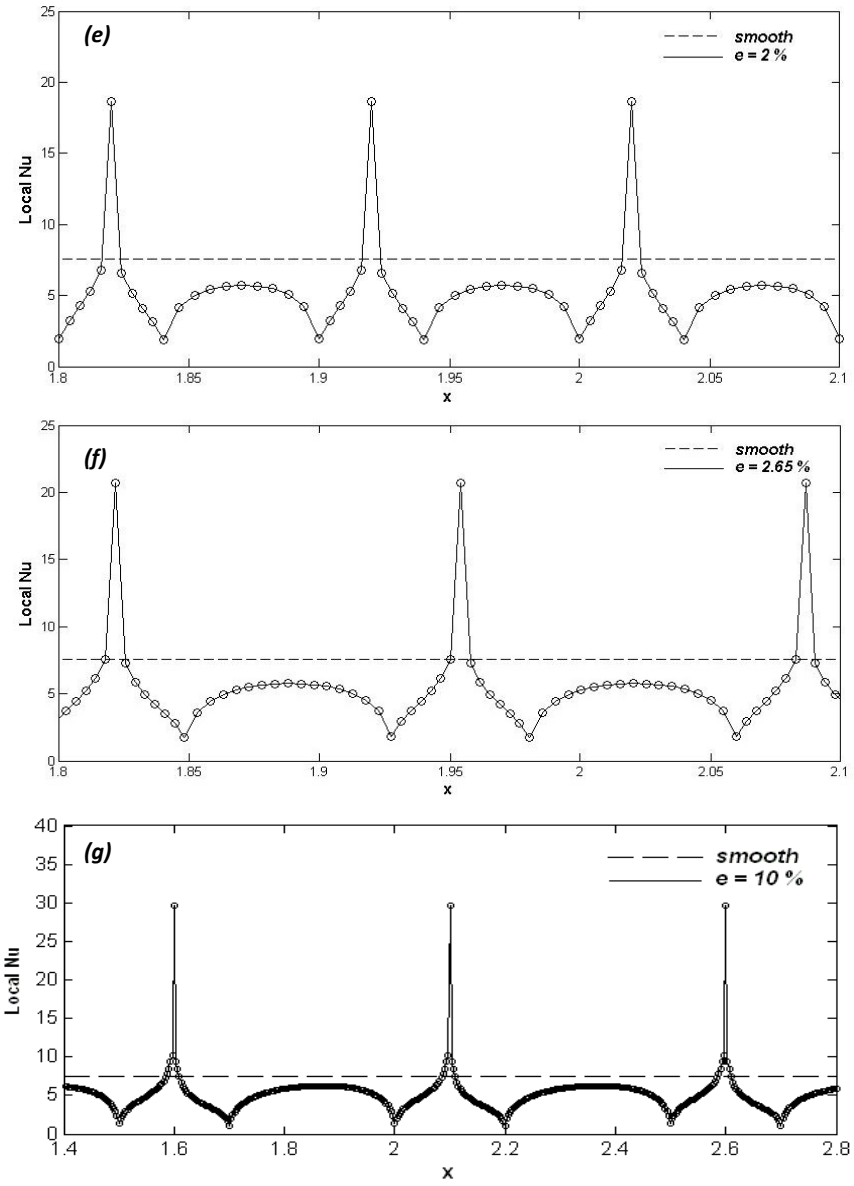


Figure 4.8: Continued.

Figure (4.9) shows the local *Nu* distribution along the channel with 1.325% relative roughness when axial conduction term is neglected and included for *Kn* = 0, *Br* = 0, and *Pe* = 3.5. Neglecting axial conduction term yields different local *Nu* values. This behavior also observed at high *Pe* which implies that neglecting axial conduction term will cause different results, similar to smooth case.

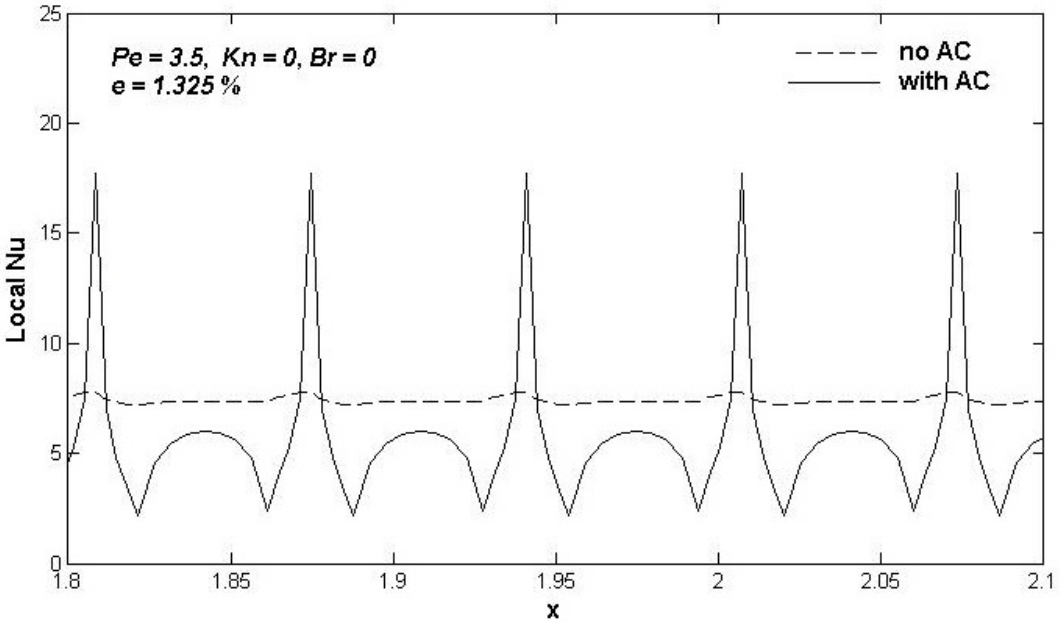


Figure 4.9: Local *Nu* distributions over the roughness elements when axial conduction term is included and neglected (*Kn* = 0, *Pe* = 3.5, *Br* = 0, ε = 1.325%).

When local *Nu* values along the channel are calculated, it is observed that it follows a wave like pattern along the rough section, different from smooth channel. Local *Nu* takes maximum value on the peak points of roughness elements and drops to a minimum value on the bottom corners of the elements, which is a property of triangular like roughness element. This behavior is

consistent with the similar studies in literature and can be explained better if the isothermal contour lines near the roughness elements are examined. Fig. (4.10) shows the isothermal contour lines near roughness elements for $Kn$ = 0, $Re$ = 100 and ε = 2.0 % case. Temperature gradient is higher at the peaks of the elements that cause a local increase in heat transfer.

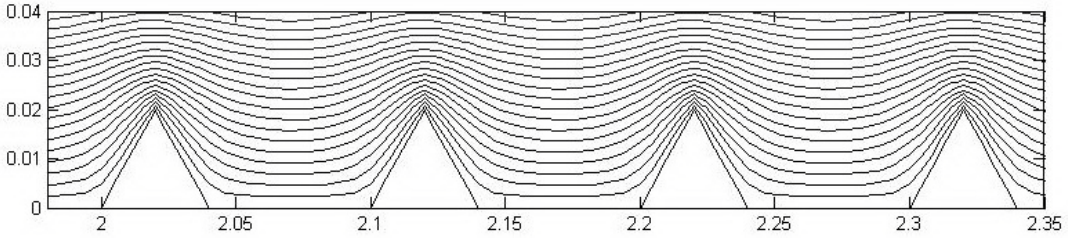


Figure 4.10: Isothermal contour lines near the roughness elements for case $Kn$ = 0, $Re$ = 100 and ε = 2.0 %.

In Figs. (4.11) and (4.12) velocity contour plots for various $Kn$ and $Re$ = 100 are given for channels having 1.325% and 2.0% relative roughness, respectively. When $Kn$ increases, rarefaction effect becomes noticeable and disturbs the velocity profile between the roughness elements. Fluid particles on the roughness element sides that face the flow have higher velocities than the particles on the other sides of the elements. As $Kn$ continues to increase, flow becomes more free and the degree of change in the velocity field around the roughness elements reduces. However, zones with lower velocities still exist after the roughness elements in downstream direction. When relative roughness height increased, disturbance in the velocity field also increases, as expected. These disturbances also affect the temperature distribution around the rough section. Velocity contour plots for $Kn$ = 0.10 for all of rough channels are given in Fig. (4.13) to show the effect of increasing roughness height on velocity field.

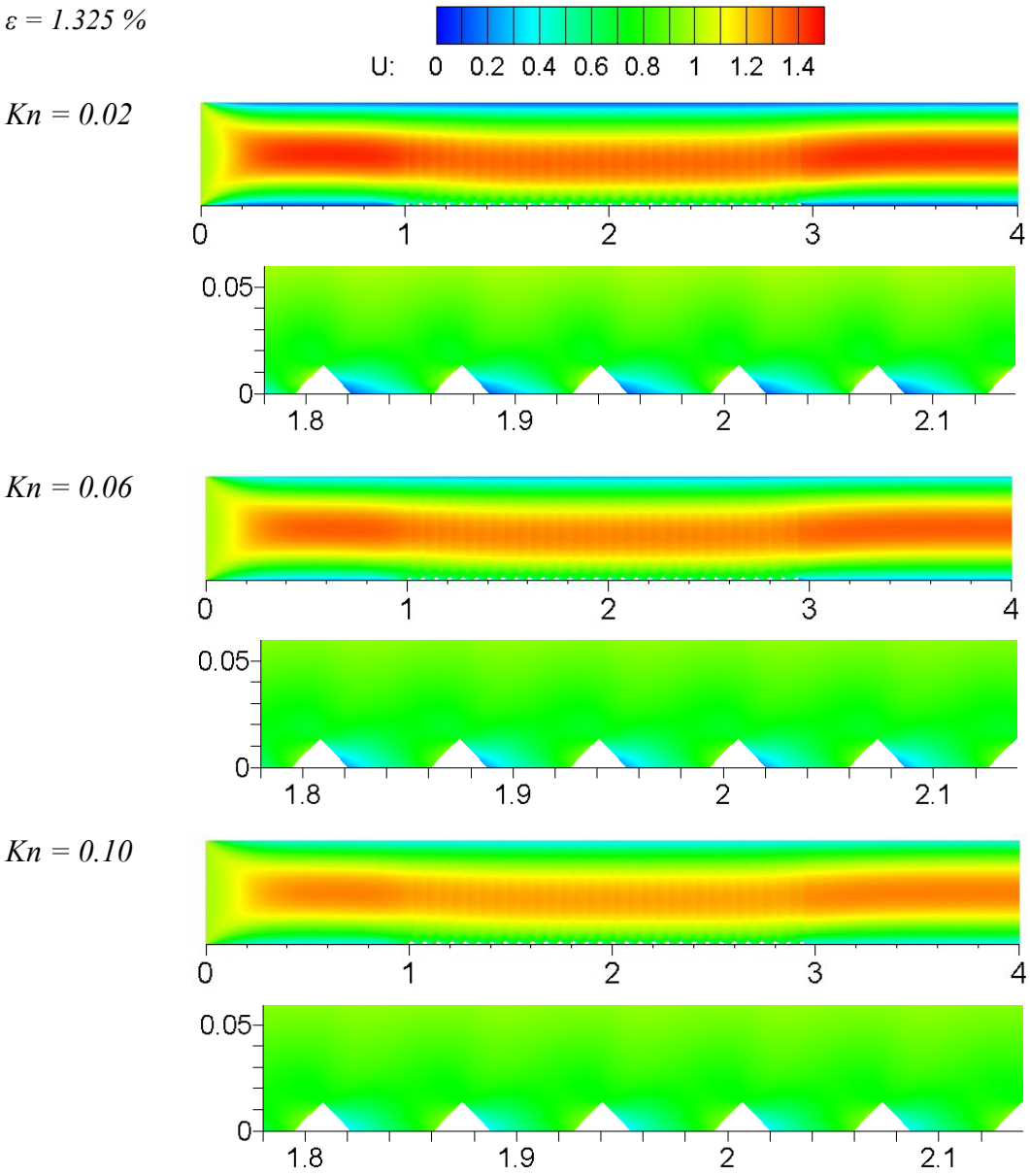


Figure 4.11: Velocity contour plots of channel with 1.325% relative roughness for various *Kn* and *Re* = 100.

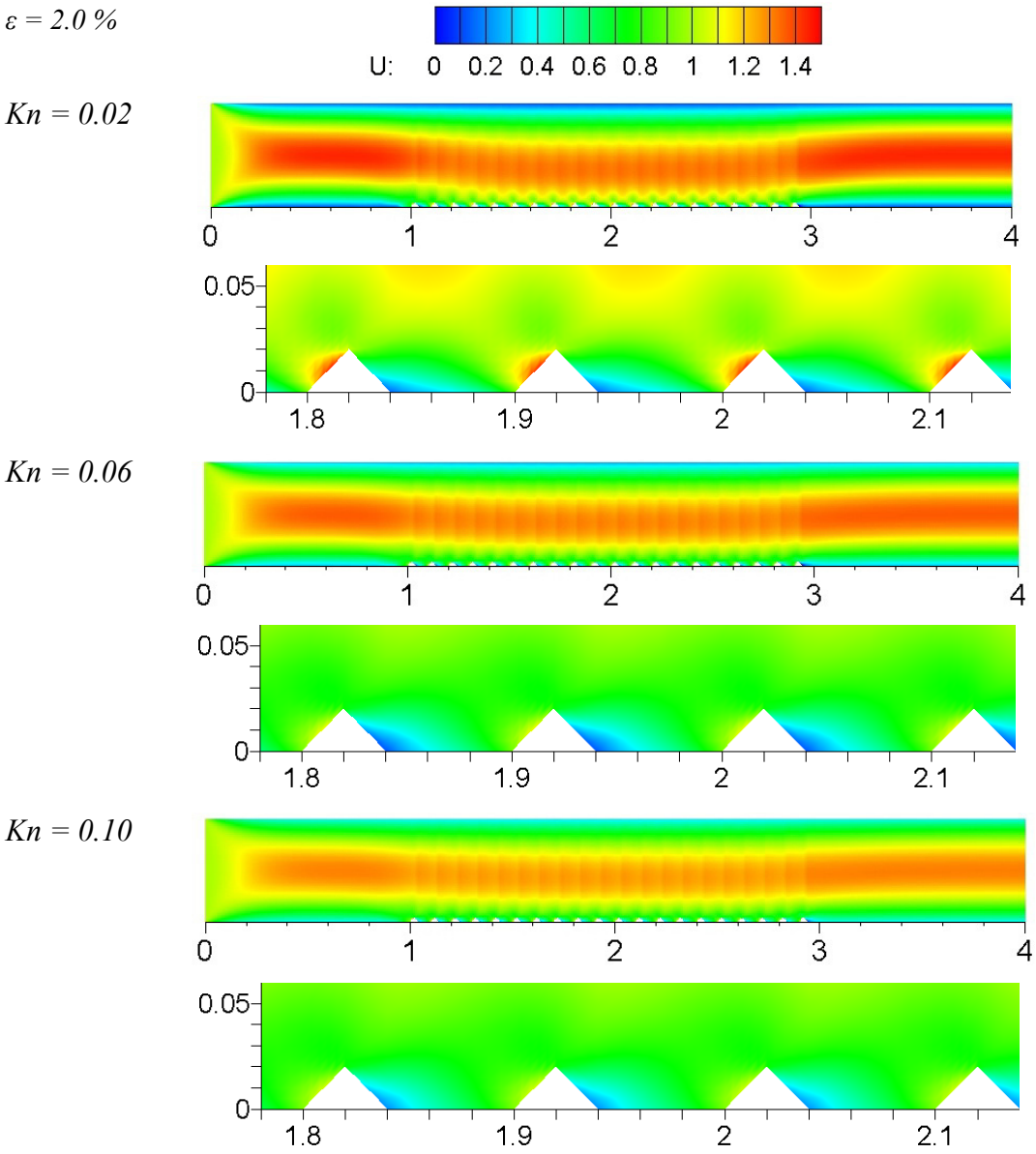


Figure 4.12: Velocity contour plots of channel with 2.0% relative roughness for various *Kn* and *Re* = 100.

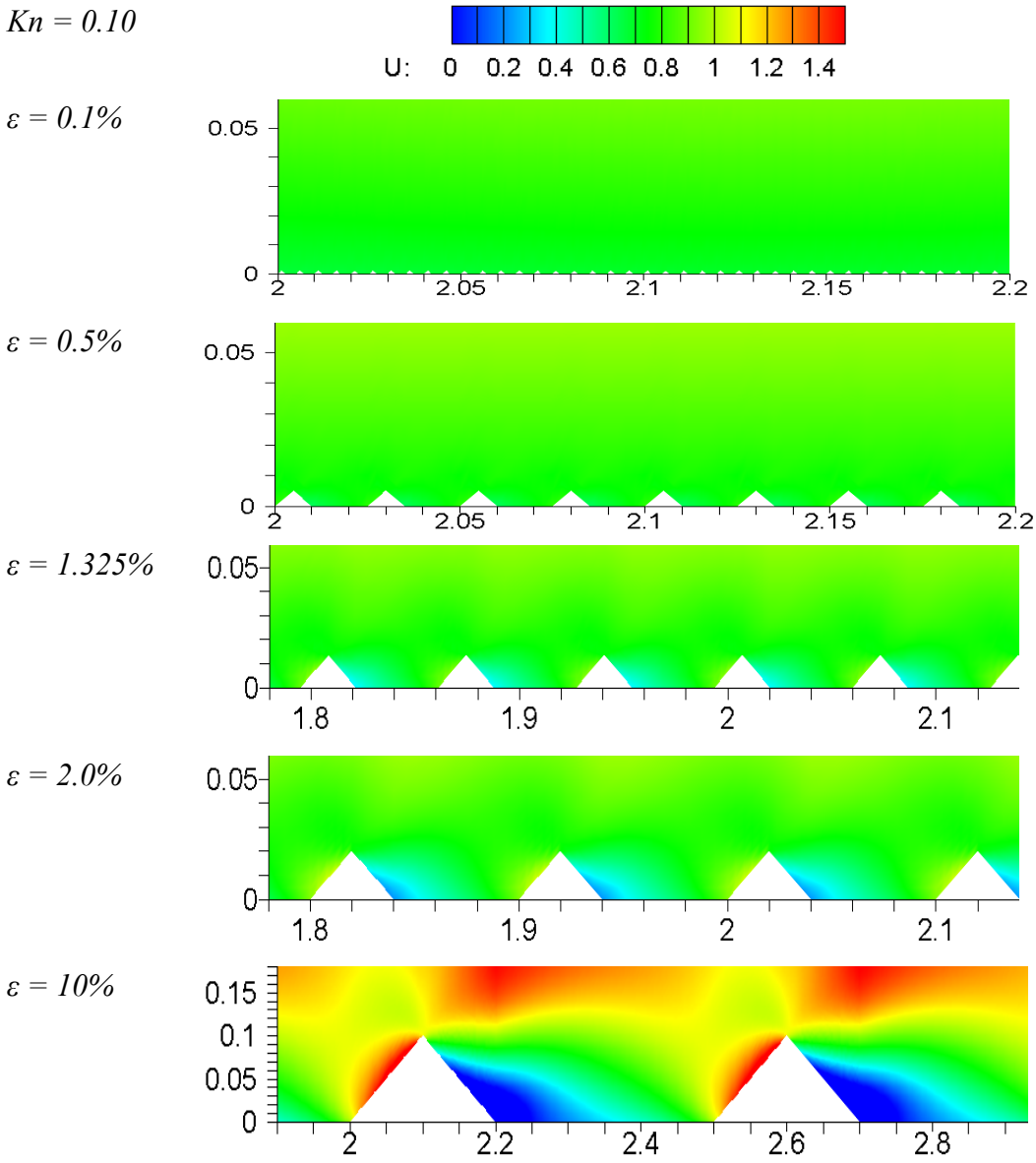


Figure 4.13: Velocity contour plots of rough channels for *Kn = 0.10* and *Re* = 100.

When rarefaction effect is considered only in the velocity field, that is slip velocity boundary condition at the wall is taken into account for momentum equations, but temperature jump boundary condition is not considered for the energy equation, temperature gradients at the top of the peaks and between the elements increased. This is shown in Fig. (4.14a), where local *Nu* values obtained with the similar pattern of no-slip / no-temperature jump case also increased. However, when temperature jump at the wall was considered, gradients right after the peaks of the elements become smaller than the other regions of the element, and heat transfer reduces in this region. Isothermal contour lines for this case are shown in Fig. (4.14b). Temperature jump is an apparent discontinuity in the temperature at the gas-wall interface, and defined as the difference between actual surface temperature and the temperature predicted by extrapolating the law of temperature variation in the gas. Thermal conductivity of the gas within a few mean free paths of the solid wall is not same as the interiors of the gas due to the effect of wall collisions. Scattered and reflected molecules at the surface have different energies which yields discontinuities in the temperature [70]. Since the temperature jump boundary condition is a mixed type boundary condition it consists of two parts, one is Dirichlet type and the other is Neumann type. Dirichlet type boundary condition, which is constant wall temperature in this case, yields isothermal contour lines that fallow the solid surface in a nearly parallel fashion. On the other hand Neumann type boundary condition yields contours normal to the surface. Thus, mixed boundary condition possesses both of these properties and yields isothermal contour lines as shown in Fig. (4.14b).

As roughness height increases, local *Nu* distribution begins to deviate from the smooth one due to increasing disturbance in velocity field and changing gradients which is shown in Fig. (4.15) for $Kn = 0.10$ and $Re = 100$. Figs. (4.16) and (4.17) show the change in local *Nu* distribution with *Kn* for channels having 1.325% and 2.0% relative roughnesses, respectively. Unlike the $Kn = 0$ cases, local *Nu* do not follow the roughness pattern. Due to the presence of temperature jump, *Nu* also

takes high values on the faces of roughness elements with high gradient. Similar to smooth cases, as *Kn* increases, increasing rarefaction effect reduces the *Nu* in both configuration. However, increasing *Pe* slightly increases the local *Nu* values at low *Kn* unlike the smooth channel cases. It is also observed that there is an increase in local *Nu* with increasing roughness heights.

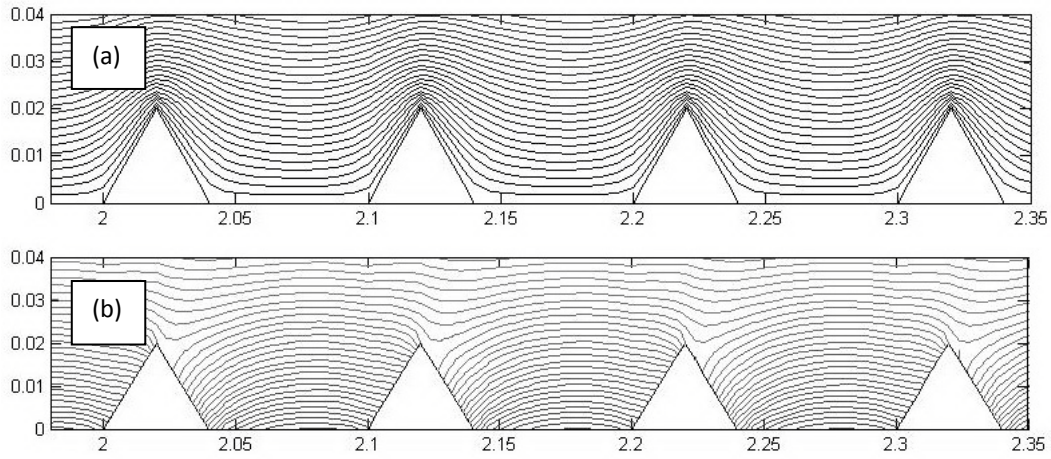


Figure 4.14: Isothermal contour lines for *Kn* = 0.10, *Re* = 100, and ε = 2.0 % (a) no temperature jump at wall, (b) temperature jump at wall.

When *Pe* increases, conduction in the fluid become less significant and convective effects dominate the heat transfer and result in enhanced heat transfer. However when convective effect is combined with the rarefaction effect, local *Nu* decreases with increasing rarefaction effect. For high *Kn*, where rarefaction effect becomes dominant, increasing relative surface roughness does not change the maximum value of local *Nu*, although for low *Kn*, increasing relative surface roughness yield higher local *Nu* values. This is shown in Figs. (4.17) and (4.18) where change of local *Nu* with *Pe* and relative roughness of the channel for *Kn* = 0.02 and *Kn* = 0.10 are displayed, respectively.

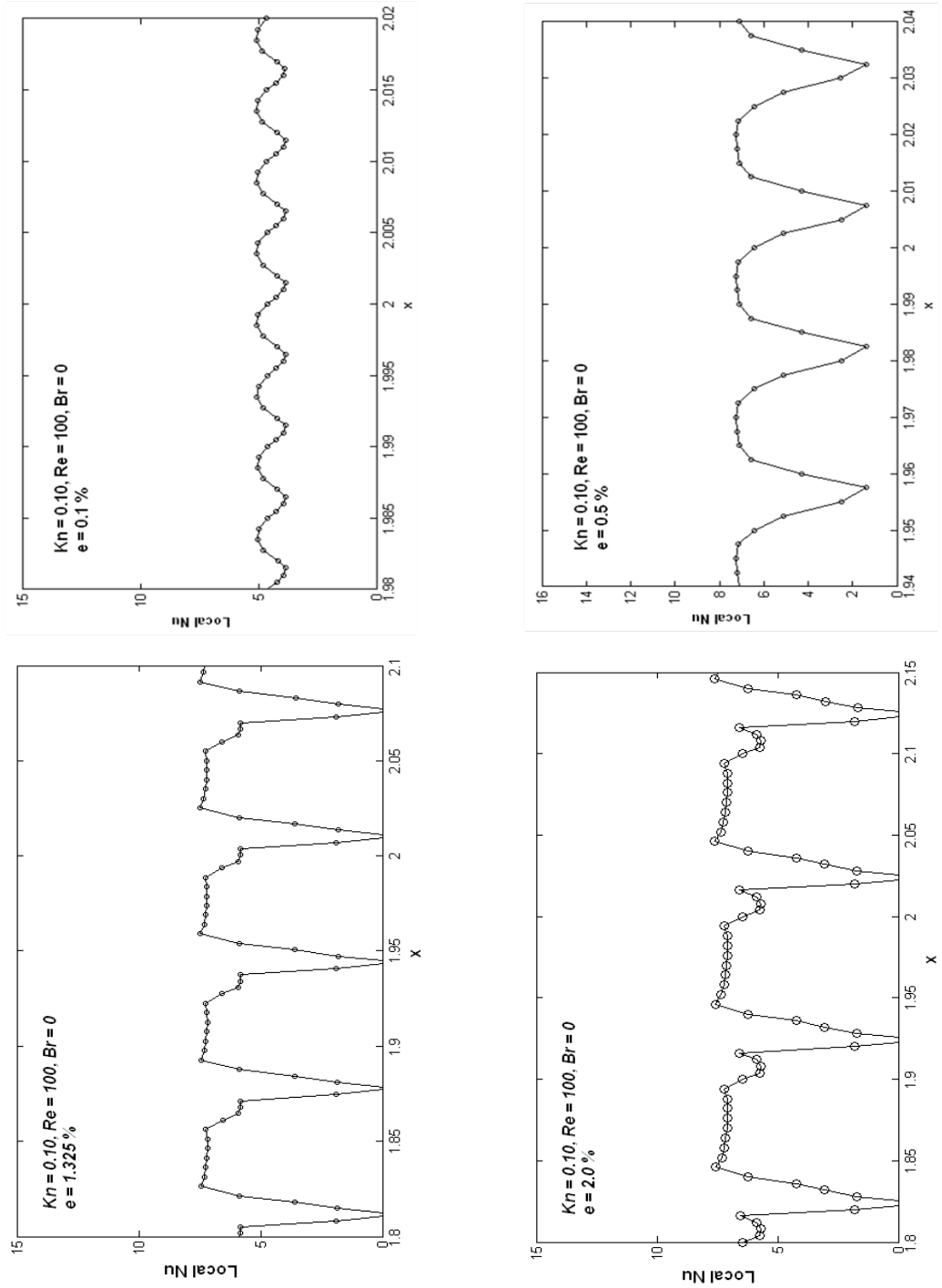


Figure 4.15: Local *Nu* distribution for channels with 0.1%, 0.5%, 1.325%, and 2.0% relative surface roughnesses and $Re = 100$, $Kn = 0.10$, $Br = 0$.

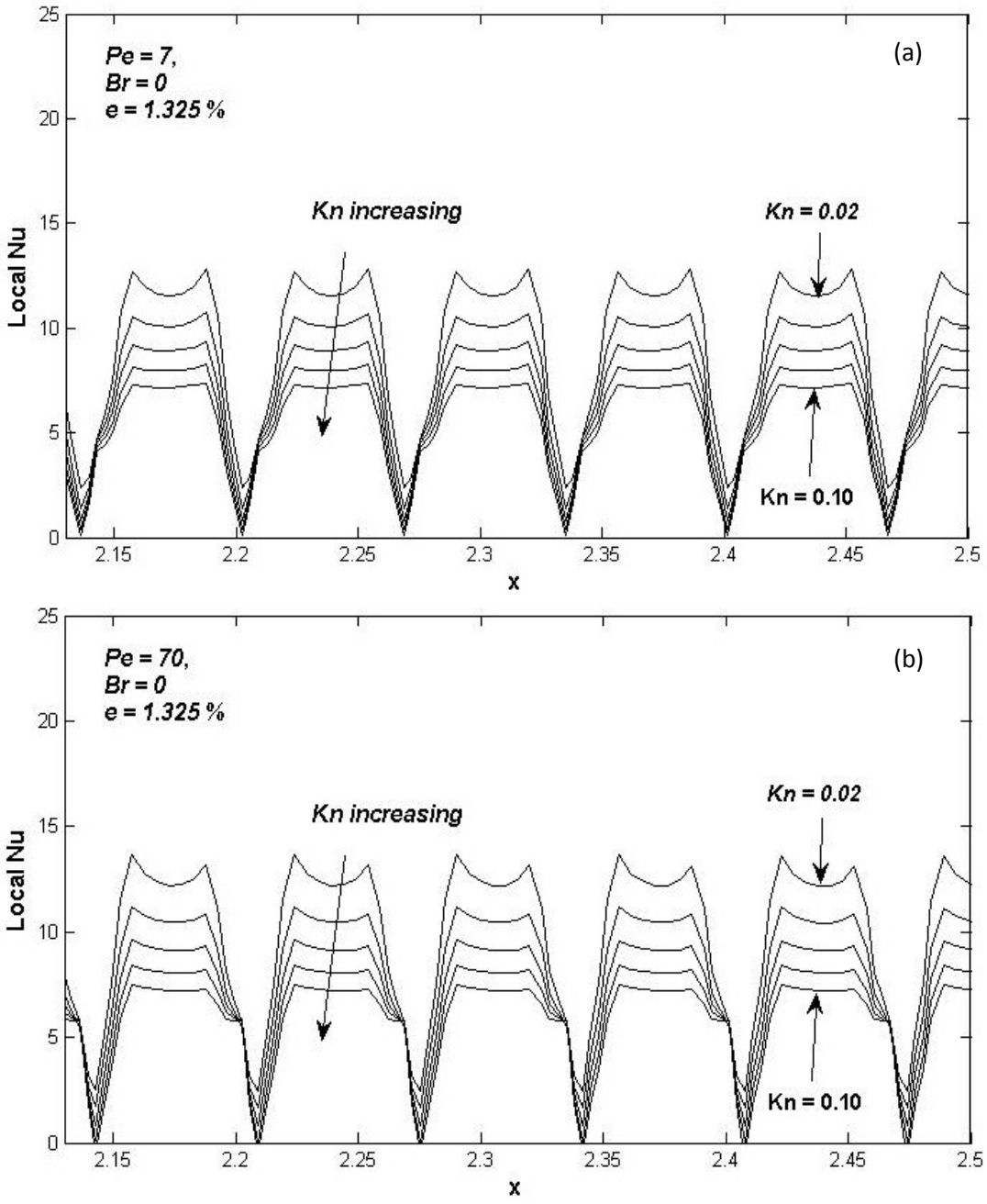


Figure 4.16: Change of local *Nu* with *Kn* for channel with ε = 1.325% relative roughness (a) *Pe* = 7, (b) *Pe* = 70.

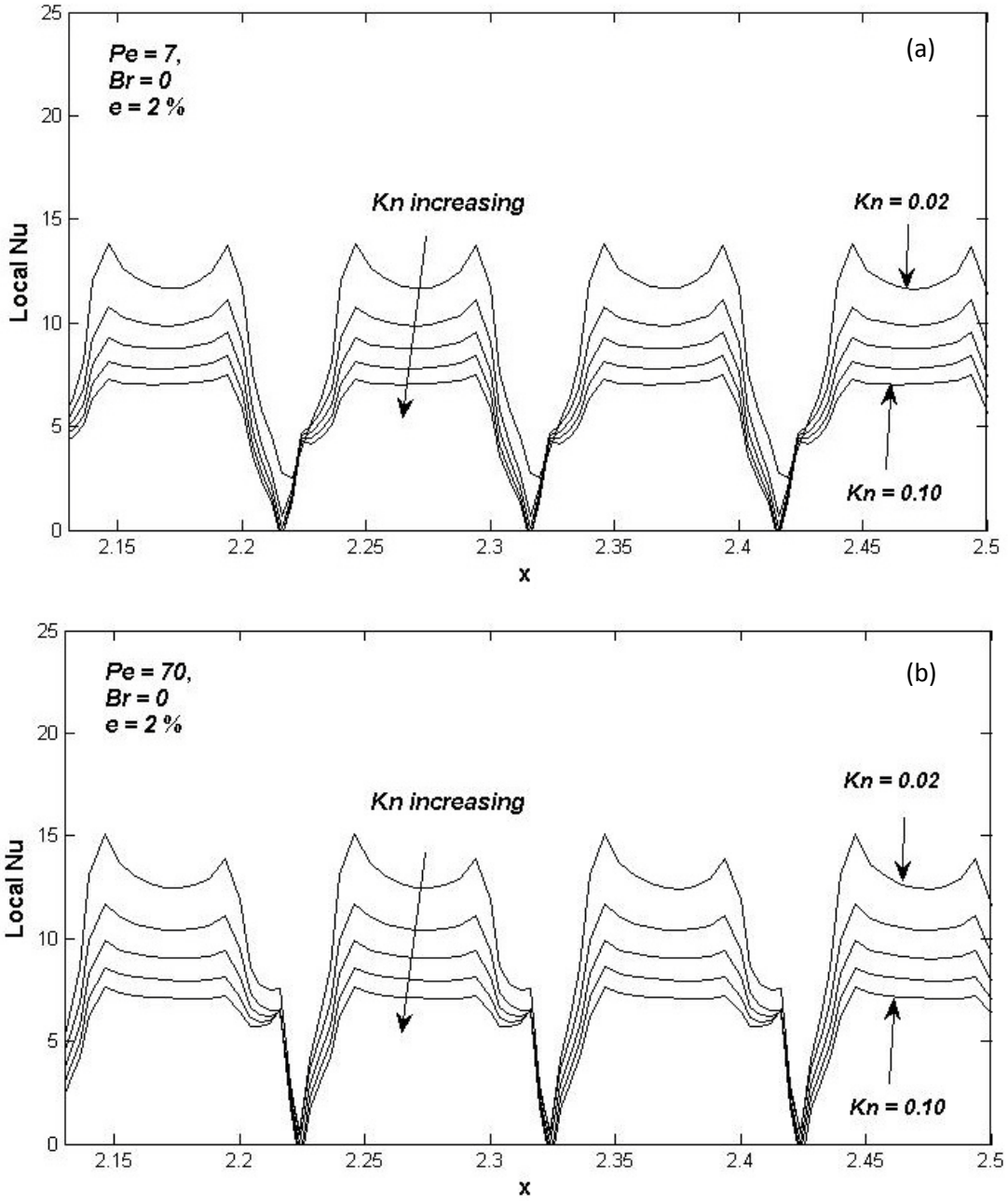


Figure 4.17: Change of local *Nu* with *Kn* for channel with ε = 2.0% relative roughness (a) *Pe* = 7, (b) *Pe* = 70.

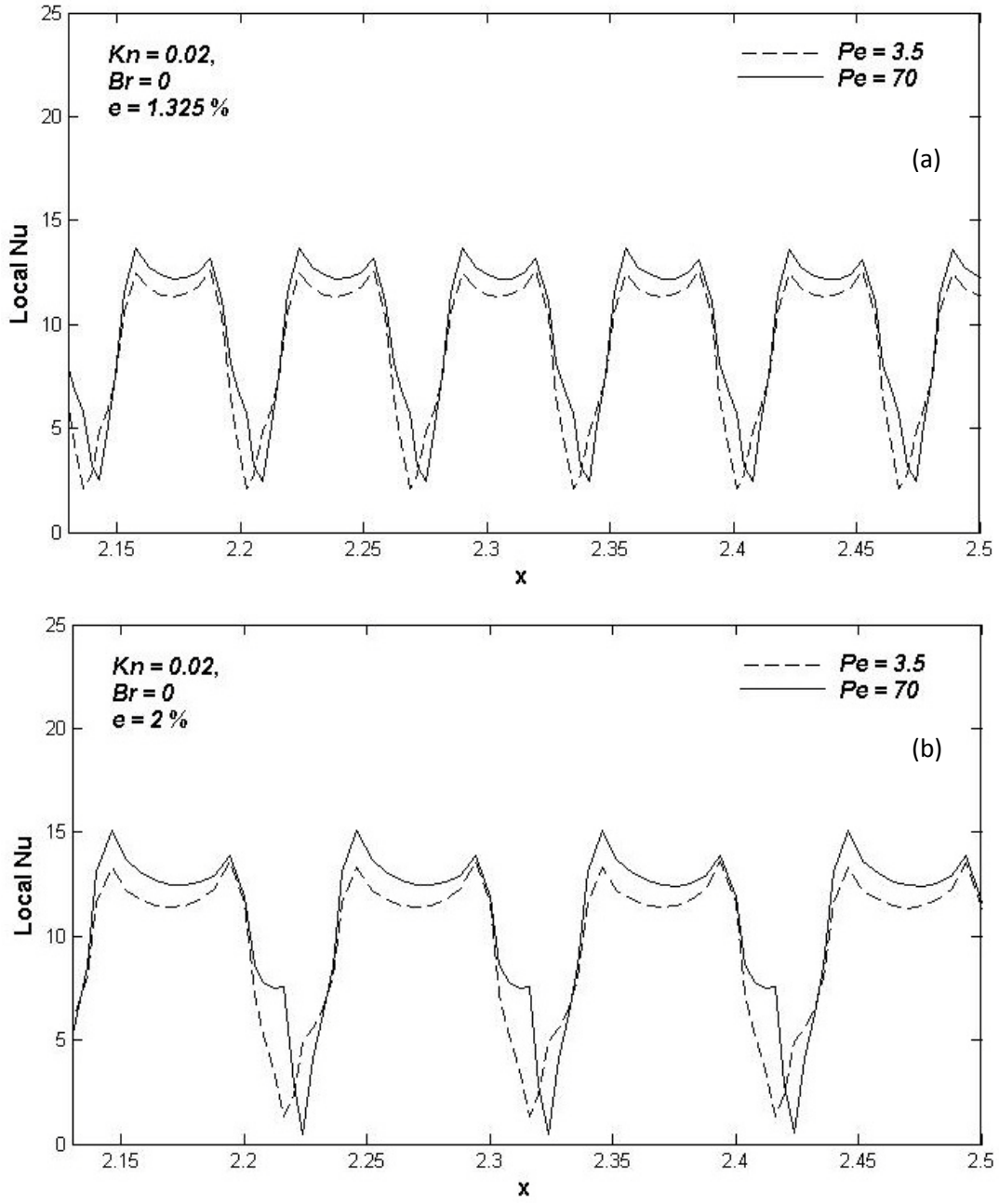


Figure 4.18: Change of local *Nu* with *Pe* and relative roughness of the channel for *Kn* = 0.02 (a) ε = 1.325 %, (b) ε = 2.0 %.

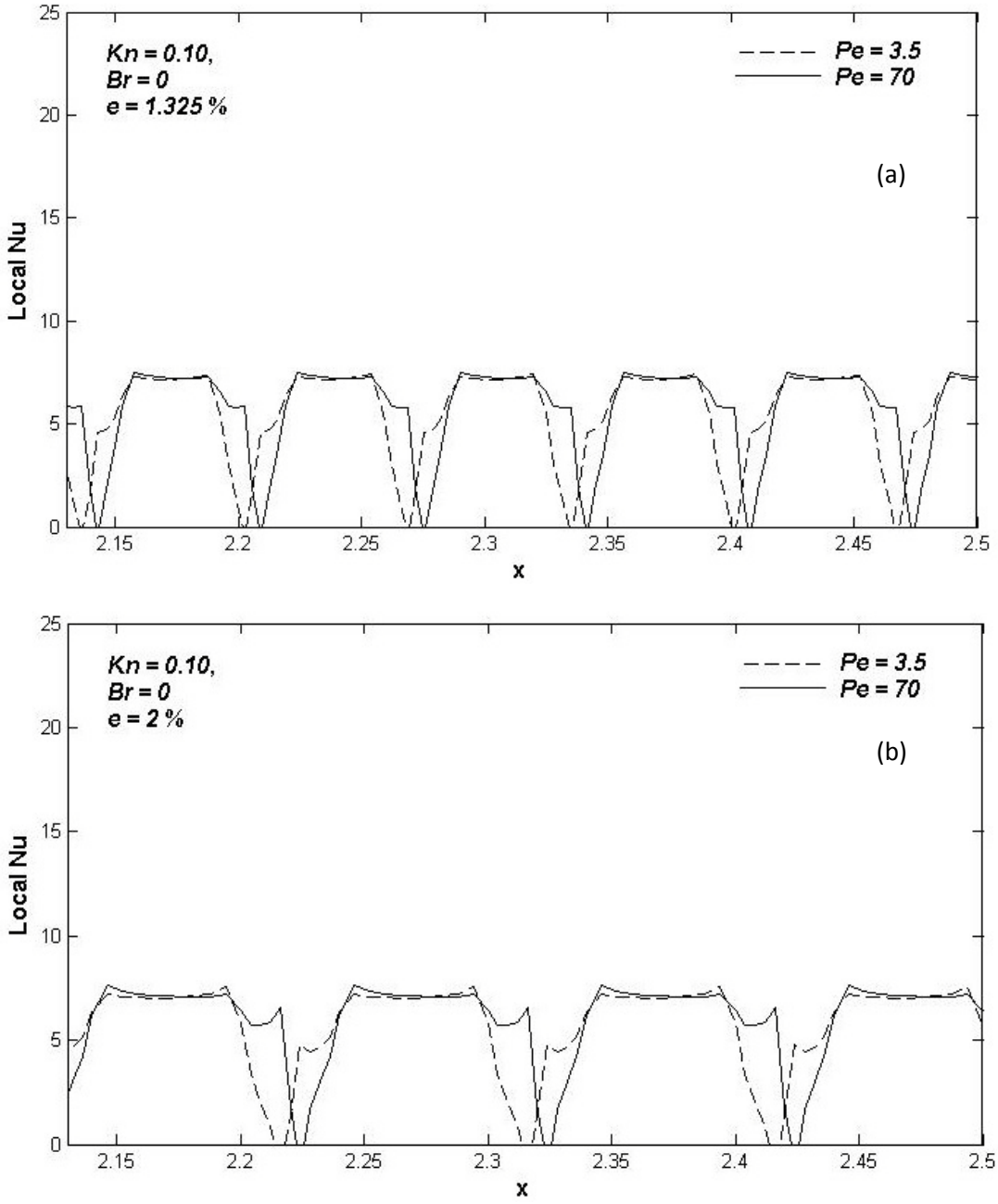


Figure 4.19: Change of local *Nu* with *Pe* and relative roughness of the channel for *Kn* = 0.10 (a) ε = 1.325 %, (b) ε = 2.0 %.

To be more specific, local *Nu* obtained for the rough channel are averaged over the channel according the formula

$$Nu_{Av} = \frac{1}{L}\int Nu_x \, dx \tag{4.1}$$

where $Nu_{Av}$ is the average *Nu*, $Nu_x$ is the local *Nu*, and *L* is the length of the channel. Then, average *Nu* values obtained for the rough channel are compared with smooth channel fully developed *Nu* values by calculating the percent difference between them according to,

$$\%\, Difference = \frac{Nu_{Av,R} - Nu_S}{Nu_{Av,R}} \times 100 \tag{4.2}$$

where $Nu_{Av,R}$ is the average *Nu* for the rough channel, and $Nu_S$ is the *Nu* for the smooth channel.

When axial conduction is included and viscous dissipation is neglected, average *Nu* in the rough channel decreases at most about 6% for *Kn* = 0 case with respect to smooth channel values. In these cases, local *Nu* takes the maximum values at the peaks of the roughness elements and this value is far greater than the corresponding smooth channel value. However, reduction in local *Nu* values between the roughness elements is dominant and peak value cannot compensate this reduction. Thus, overall *Nu* reduces as the relative roughness height increases. A similar result is achieved in Refs. [50, 51] for microtubes with triangular roughness elements. On the other hand, in the presence of rarefaction effect, an increase in the overall *Nu* with respect to smooth channel values is observed. In this case, increase is up to 24% and more obvious at low *Kn* values and less

pronounceable at high *Kn* values. Also average *Nu* values increases slightly with increasing *Pe* and relative surface roughness height when rarefaction is considered which is shown graphically in Fig. (4.20). Average *Nu* and percent differences with respect to smooth cases where axial conduction included and viscous dissipation neglected are summarized in Table (4.5).

In microchannels, length to height ratio of the channel is high and viscous heating should become important. When viscous dissipation is considered with axial conduction, existence of surface roughness reduces the average *Nu* for $Kn = 0$ case up to 6.3 % with respect to smooth channel value. Similar to the previous case, when rarefaction effect is considered, surface roughness increases the average *Nu* up to 43% at low *Kn* with respect to smooth channel value. Average *Nu* values for various *Kn* and *Pe* values are shown graphically in Fig. (4.21). Also, average *Nu* values and percent differences with respect to smooth cases where axial conduction and viscous dissipation included are summarized in Table (4.6).

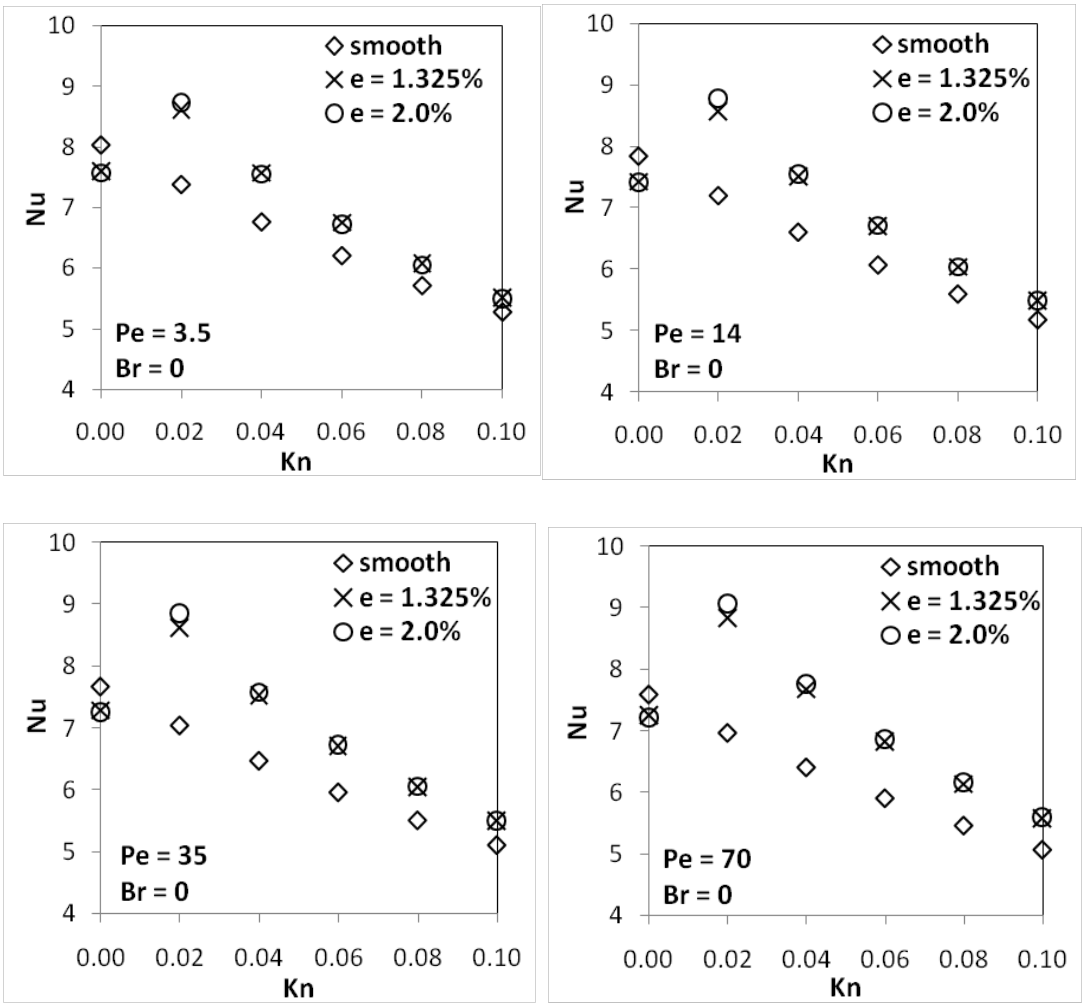


Figure 4.20: Channel averaged *Nu* for various *Kn* and *Pe* values when axial conduction included and viscous dissipation neglected.

Table 4.5: Channel averaged *Nu* compared with fully developed smooth channel values when axial conduction included and viscous dissipation neglected.

| *Pe* | *Kn* | *With Axial Conduction (Br = 0)* | | | | |
|---|---|---|---|---|---|---|
| | | *Nu* | | | Difference (ε = 1.325%) | Difference (ε = 2.0%) |
| | | Smooth | Rough 1.325% | Rough 2.0% | | |
| 3.5 | 0 | 8.030 | 7.600 | 7.578 | -5.661 | -5.971 |
| | 0.02 | 7.378 | 8.613 | 8.746 | 14.343 | 15.644 |
| | 0.04 | 6.762 | 7.565 | 7.561 | 10.612 | 10.563 |
| | 0.06 | 6.206 | 6.746 | 6.728 | 8.010 | 7.762 |
| | 0.08 | 5.713 | 6.071 | 6.051 | 5.903 | 5.591 |
| | 0.10 | 5.278 | 5.508 | 5.489 | 4.168 | 3.837 |
| 7 | 0 | 7.955 | 7.534 | 7.511 | -5.581 | -5.906 |
| | 0.02 | 7.307 | 8.651 | 8.762 | 15.535 | 16.602 |
| | 0.04 | 6.701 | 7.544 | 7.551 | 11.179 | 11.258 |
| | 0.06 | 6.154 | 6.730 | 6.719 | 8.560 | 8.406 |
| | 0.08 | 5.669 | 6.060 | 6.045 | 6.450 | 6.215 |
| | 0.10 | 5.241 | 5.500 | 5.485 | 4.710 | 4.447 |
| 14 | 0 | 7.841 | 7.436 | 7.411 | -5.453 | -5.799 |
| | 0.02 | 7.200 | 8.587 | 8.786 | 16.148 | 18.049 |
| | 0.04 | 6.607 | 7.520 | 7.543 | 12.139 | 12.409 |
| | 0.06 | 6.075 | 6.710 | 6.709 | 9.461 | 9.451 |
| | 0.08 | 5.603 | 6.046 | 6.038 | 7.321 | 7.205 |
| | 0.10 | 5.186 | 5.491 | 5.482 | 5.557 | 5.400 |
| 35 | 0 | 7.668 | 7.294 | 7.267 | -5.134 | -5.512 |
| | 0.02 | 7.041 | 8.633 | 8.863 | 18.437 | 20.557 |
| | 0.04 | 6.470 | 7.531 | 7.585 | 14.092 | 14.704 |
| | 0.06 | 5.961 | 6.715 | 6.737 | 11.223 | 11.513 |
| | 0.08 | 5.509 | 6.051 | 6.061 | 8.960 | 9.114 |
| | 0.10 | 5.109 | 5.500 | 5.505 | 7.103 | 7.197 |
| 70 | 0 | 7.586 | 7.250 | 7.223 | -4.642 | -5.029 |
| | 0.02 | 6.966 | 8.838 | 9.084 | 21.180 | 23.319 |
| | 0.04 | 6.408 | 7.672 | 7.772 | 16.472 | 17.547 |
| | 0.06 | 5.909 | 6.818 | 6.880 | 13.336 | 14.112 |
| | 0.08 | 5.467 | 6.134 | 6.179 | 10.880 | 11.519 |
| | 0.10 | 5.076 | 5.570 | 5.606 | 8.877 | 9.454 |

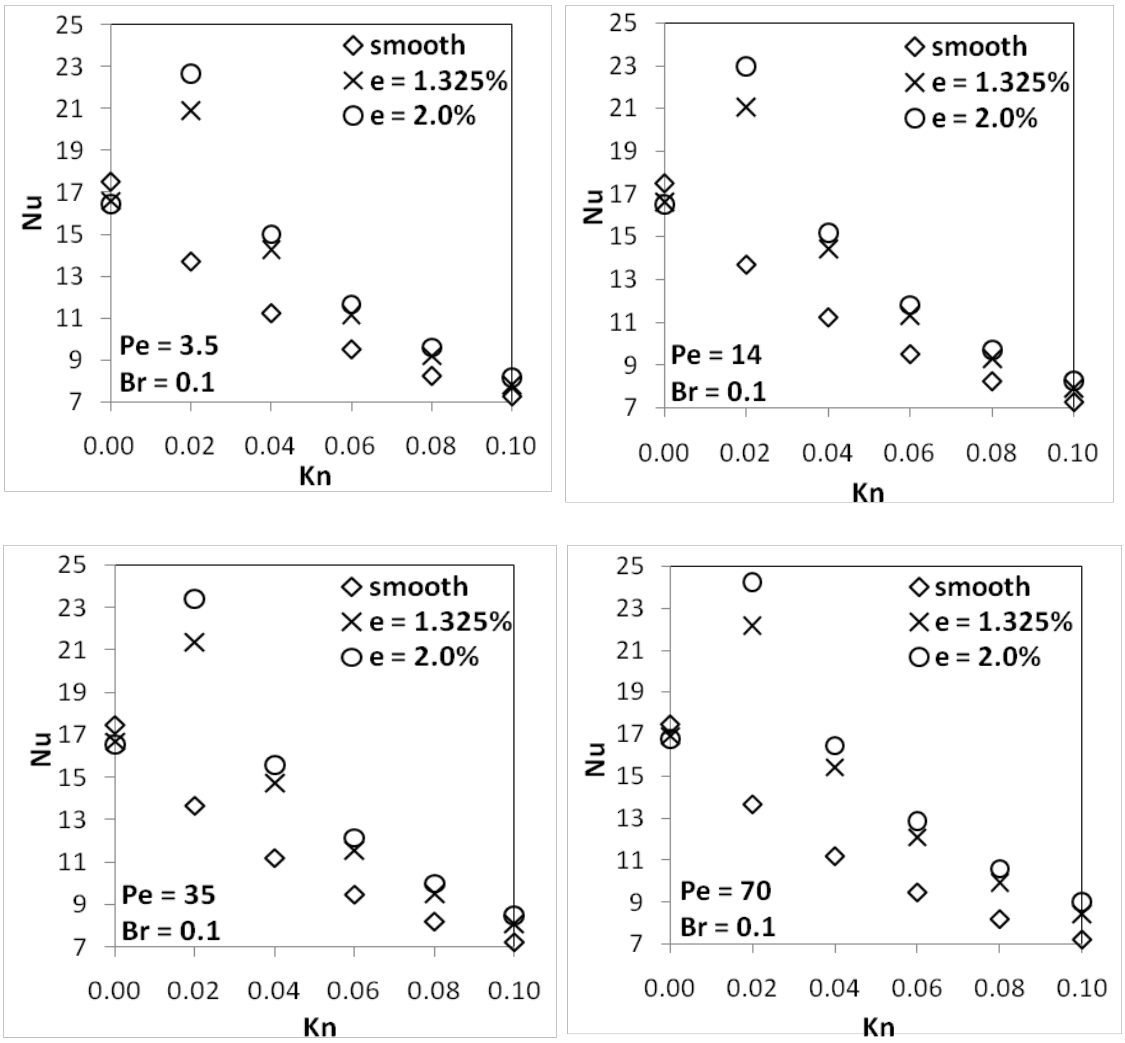


Figure 4.21: Channel averaged *Nu* for various *Kn* and *Pe* values when axial conduction and viscous dissipation included.

Table 4.6: Channel averaged *Nu* compared with fully developed smooth channel values when axial conduction and viscous dissipation included.

| *Pe* | *Kn* | *With Axial Conduction (Br = 0.1)* | | | | |
|---|---|---|---|---|---|---|
| | | *Nu* | | | Difference (ε = 1.325%) | Difference (ε = 2.0%) |
| | | Smooth | Rough 1.325% | Rough 2.0% | | |
| 3.5 | 0 | 17.485 | 16.582 | 16.445 | -5.448 | -6.323 |
| | 0.02 | 13.679 | 20.897 | 22.677 | 34.541 | 39.678 |
| | 0.04 | 11.215 | 14.267 | 14.982 | 21.392 | 25.143 |
| | 0.06 | 9.493 | 11.173 | 11.643 | 15.037 | 18.468 |
| | 0.08 | 8.224 | 9.201 | 9.569 | 10.615 | 14.052 |
| | 0.10 | 7.251 | 7.815 | 8.123 | 7.219 | 10.733 |
| 7 | 0 | 17.485 | 16.595 | 16.458 | -5.363 | -6.237 |
| | 0.02 | 13.679 | 21.215 | 22.772 | 35.522 | 39.930 |
| | 0.04 | 11.215 | 14.316 | 15.042 | 21.663 | 25.443 |
| | 0.06 | 9.493 | 11.212 | 11.694 | 15.329 | 18.823 |
| | 0.08 | 8.224 | 9.232 | 9.611 | 10.917 | 14.435 |
| | 0.10 | 7.251 | 7.841 | 8.159 | 7.528 | 11.134 |
| 14 | 0 | 17.485 | 16.621 | 16.485 | -5.198 | -6.067 |
| | 0.02 | 13.679 | 21.052 | 22.951 | 35.024 | 40.400 |
| | 0.04 | 11.215 | 14.419 | 15.171 | 22.219 | 26.076 |
| | 0.06 | 9.493 | 11.292 | 11.802 | 15.928 | 19.564 |
| | 0.08 | 8.224 | 9.297 | 9.702 | 11.537 | 15.232 |
| | 0.10 | 7.251 | 7.895 | 8.237 | 8.159 | 11.967 |
| 35 | 0 | 17.485 | 16.707 | 16.567 | -4.660 | -5.542 |
| | 0.02 | 13.679 | 21.420 | 23.436 | 36.138 | 41.633 |
| | 0.04 | 11.215 | 14.759 | 15.606 | 24.014 | 28.138 |
| | 0.06 | 9.493 | 11.558 | 12.164 | 17.864 | 21.955 |
| | 0.08 | 8.224 | 9.512 | 10.005 | 13.539 | 17.799 |
| | 0.10 | 7.251 | 8.074 | 8.496 | 10.198 | 14.653 |
| 70 | 0 | 17.485 | 16.887 | 16.746 | -3.544 | -4.411 |
| | 0.02 | 13.679 | 22.147 | 24.236 | 38.235 | 43.559 |
| | 0.04 | 11.215 | 15.397 | 16.437 | 27.161 | 31.769 |
| | 0.06 | 9.493 | 12.059 | 12.849 | 21.280 | 26.116 |
| | 0.08 | 8.224 | 9.921 | 10.580 | 17.101 | 22.271 |
| | 0.10 | 7.251 | 8.417 | 8.991 | 13.850 | 19.349 |

When axial conduction and viscous dissipation are neglected, different behavior of average *Nu*, compared to previous cases, are observed. It is seen in Fig. (4.9) that neglecting axial conduction term in rough channel should yield different results than including axial conduction. In this case, surface roughness generally decreases average *Nu* at low *Pe* and high *Kn*, where axial conduction becomes important and also increasing rarefaction should reduce the collision rate of molecules. As *Pe* increases, surface roughness tends to increase the average *Nu*. Similar to the previous cases, increase is more obvious at low *Kn*. When viscous dissipation is included, surface roughness reduces the *Nu* up to moderate *Pe* except low rarefied cases, and then the effect is in increasing way. Again at low *Kn* values, surface roughness increases the average *Nu* with increasing roughness height. Channel averaged *Nu* values for various *Kn* and *Pe* values are shown graphically in Fig. (4.22) for axial conduction and viscous dissipation neglected cases, and in Fig. (4.23) for the cases where axial conduction neglected but viscous dissipation included. Also, summary of average *Nu* values when axial conduction and viscous dissipation neglected are given in Table (4.7), while axial conduction neglected and viscous dissipation added cases are given in Table (4.8).

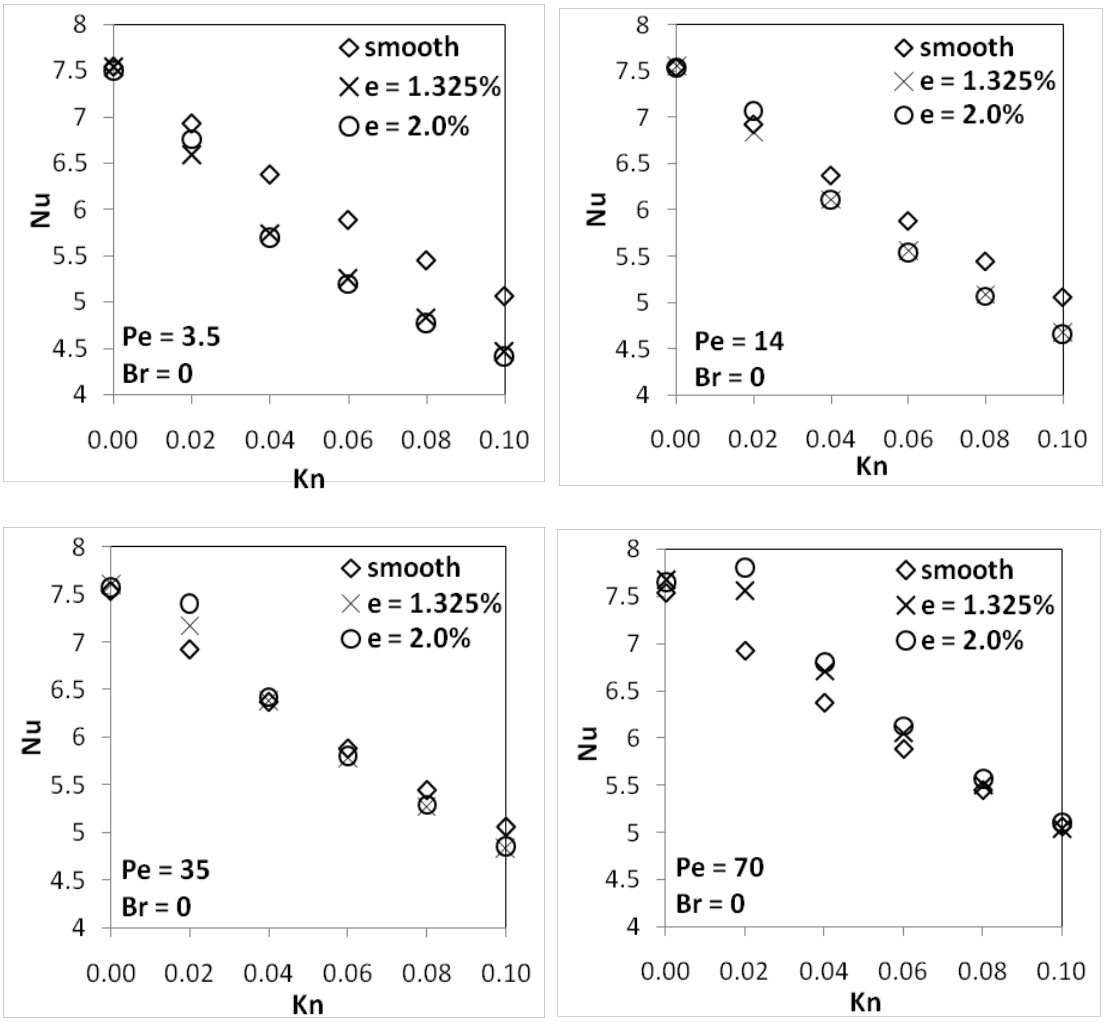


Figure 4.22: Channel averaged *Nu* for various *Kn* and *Pe* values when axial conduction and viscous dissipation neglected.

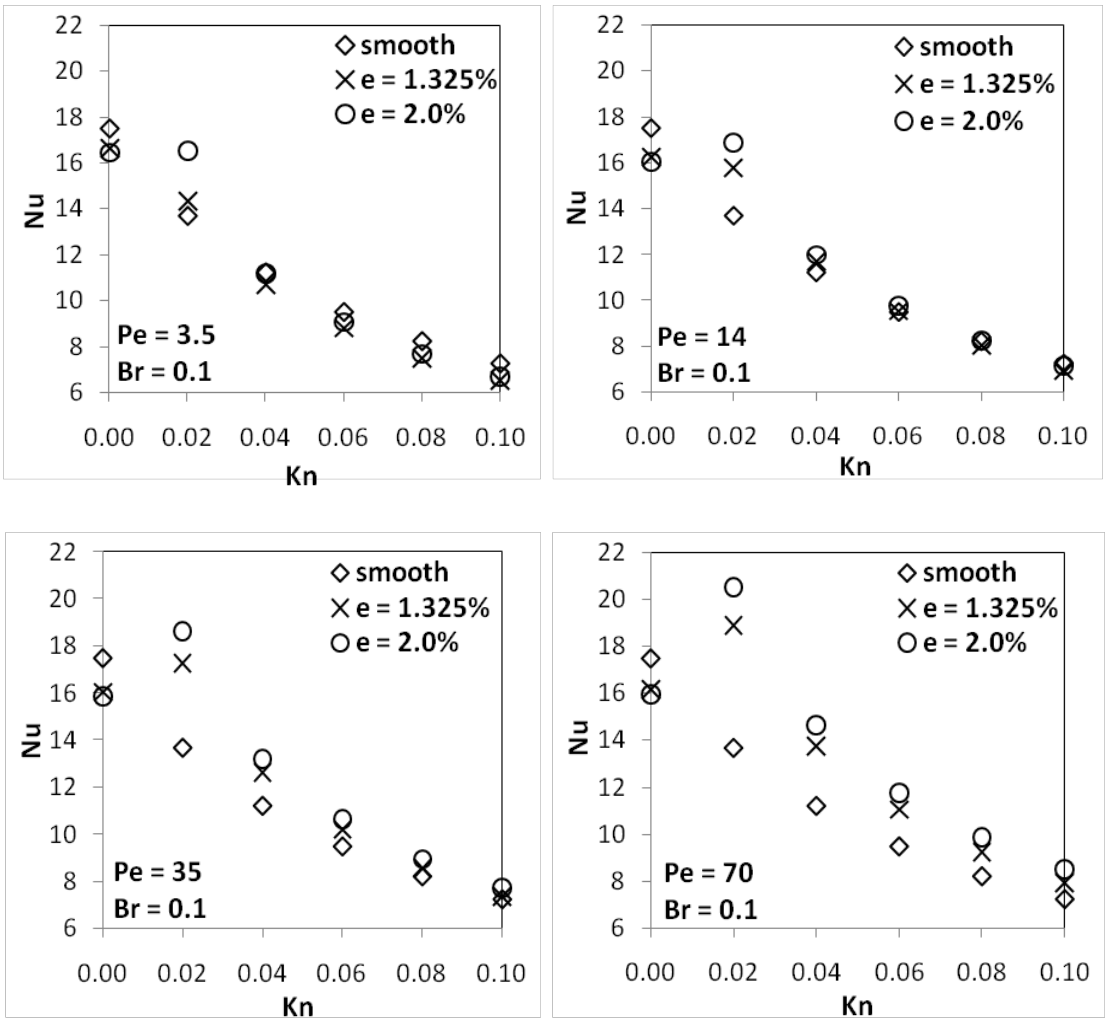


Figure 4.23: Channel averaged *Nu* for various *Kn* and *Pe* values when axial conduction neglected and viscous dissipation included.

Table 4.7: Channel averaged *Nu* compared with fully developed smooth channel values when axial conduction and viscous dissipation neglected.

| *Pe* | *Kn* | *Without Axial Conduction (Br = 0)* | | | | |
|---|---|---|---|---|---|---|
| | | *Nu* | | | Difference (ε = 1.325%) | Difference (ε = 2.0%) |
| | | Smooth | Rough 1.325% | Rough 2.0% | | |
| 3.5 | 0 | 7.541 | 7.539 | 7.511 | -0.027 | -0.398 |
| | 0.02 | 6.926 | 6.586 | 6.764 | -5.159 | -2.394 |
| | 0.04 | 6.374 | 5.737 | 5.696 | -11.095 | -11.908 |
| | 0.06 | 5.883 | 5.255 | 5.196 | -11.951 | -13.212 |
| | 0.08 | 5.446 | 4.832 | 4.774 | -12.708 | -14.085 |
| | 0.10 | 5.059 | 4.460 | 4.406 | -13.422 | -14.810 |
| 7 | 0 | 7.541 | 7.545 | 7.519 | 0.048 | -0.294 |
| | 0.02 | 6.926 | 6.708 | 6.813 | -3.255 | -1.664 |
| | 0.04 | 6.374 | 5.934 | 5.899 | -7.419 | -8.061 |
| | 0.06 | 5.883 | 5.415 | 5.362 | -8.646 | -9.711 |
| | 0.08 | 5.446 | 4.966 | 4.914 | -9.670 | -10.817 |
| | 0.10 | 5.059 | 4.574 | 4.527 | -10.615 | -11.742 |
| 14 | 0 | 7.541 | 7.560 | 7.534 | 0.246 | -0.091 |
| | 0.02 | 6.926 | 6.836 | 7.066 | -1.317 | 1.984 |
| | 0.04 | 6.374 | 6.114 | 6.109 | -4.253 | -4.339 |
| | 0.06 | 5.883 | 5.563 | 5.537 | -5.748 | -6.251 |
| | 0.08 | 5.446 | 5.089 | 5.061 | -7.006 | -7.598 |
| | 0.10 | 5.059 | 4.678 | 4.653 | -8.148 | -8.730 |
| 35 | 0 | 7.541 | 7.605 | 7.579 | 0.838 | 0.505 |
| | 0.02 | 6.926 | 7.169 | 7.405 | 3.388 | 6.466 |
| | 0.04 | 6.374 | 6.385 | 6.423 | 0.166 | 0.763 |
| | 0.06 | 5.883 | 5.786 | 5.801 | -1.677 | -1.411 |
| | 0.08 | 5.446 | 5.277 | 5.287 | -3.210 | -3.001 |
| | 0.10 | 5.059 | 4.838 | 4.849 | -4.566 | -4.324 |
| 70 | 0 | 7.541 | 7.678 | 7.653 | 1.787 | 1.465 |
| | 0.02 | 6.926 | 7.560 | 7.814 | 8.382 | 11.363 |
| | 0.04 | 6.374 | 6.703 | 6.805 | 4.904 | 6.333 |
| | 0.06 | 5.883 | 6.050 | 6.126 | 2.756 | 3.969 |
| | 0.08 | 5.446 | 5.502 | 5.570 | 1.013 | 2.226 |
| | 0.10 | 5.059 | 5.035 | 5.100 | -0.481 | 0.811 |

Table 4.8: Channel averaged *Nu* compared with fully developed smooth channel values when axial conduction neglected and viscous dissipation included.

| *Pe* | *Kn* | *Without Axial Conduction (Br = 0.1)* | | | | |
|---|---|---|---|---|---|---|
| | | *Nu* | | | Difference (ε = 1.325%) | Difference (ε = 2.0%) |
| | | Smooth | Rough 1.325% | Rough 2.0% | | |
| 3.5 | 0 | 17.485 | 16.655 | 16.444 | -4.983 | -6.329 |
| | 0.02 | 13.679 | 14.330 | 16.535 | 4.545 | 17.273 |
| | 0.04 | 11.215 | 10.716 | 11.165 | -4.658 | -0.446 |
| | 0.06 | 9.493 | 8.821 | 9.049 | -7.613 | -4.908 |
| | 0.08 | 8.224 | 7.508 | 7.666 | -9.539 | -7.272 |
| | 0.10 | 7.251 | 6.530 | 6.658 | -11.043 | -8.905 |
| 7 | 0 | 17.485 | 16.455 | 16.248 | -6.258 | -7.616 |
| | 0.02 | 13.679 | 15.069 | 16.066 | 9.226 | 14.855 |
| | 0.04 | 11.215 | 11.133 | 11.366 | -0.734 | 1.324 |
| | 0.06 | 9.493 | 9.141 | 9.278 | -3.855 | -2.313 |
| | 0.08 | 8.224 | 7.757 | 7.876 | -6.018 | -4.413 |
| | 0.10 | 7.251 | 6.729 | 6.843 | -7.753 | -5.964 |
| 14 | 0 | 17.485 | 16.257 | 16.052 | -7.553 | -8.925 |
| | 0.02 | 13.679 | 15.775 | 16.889 | 13.289 | 19.005 |
| | 0.04 | 11.215 | 11.711 | 12.001 | 4.233 | 6.550 |
| | 0.06 | 9.493 | 9.545 | 9.757 | 0.540 | 2.702 |
| | 0.08 | 8.224 | 8.057 | 8.250 | -2.069 | 0.310 |
| | 0.10 | 7.251 | 6.962 | 7.143 | -4.158 | -1.511 |
| 35 | 0 | 17.485 | 16.067 | 15.866 | -8.825 | -10.206 |
| | 0.02 | 13.679 | 17.308 | 18.641 | 20.966 | 26.618 |
| | 0.04 | 11.215 | 12.656 | 13.194 | 11.385 | 14.996 |
| | 0.06 | 9.493 | 10.213 | 10.639 | 7.048 | 10.775 |
| | 0.08 | 8.224 | 8.563 | 8.942 | 3.957 | 8.031 |
| | 0.10 | 7.251 | 7.362 | 7.709 | 1.505 | 5.936 |
| 70 | 0 | 17.485 | 16.130 | 15.946 | -8.398 | -9.648 |
| | 0.02 | 13.679 | 18.885 | 20.507 | 27.569 | 33.295 |
| | 0.04 | 11.215 | 13.735 | 14.621 | 18.347 | 23.295 |
| | 0.06 | 9.493 | 11.018 | 11.755 | 13.845 | 19.239 |
| | 0.08 | 8.224 | 9.202 | 9.859 | 10.629 | 16.582 |
| | 0.10 | 7.251 | 7.889 | 8.489 | 8.091 | 14.580 |

If *Nu* is averaged over only the rough sections of the channels, they will indicate the average *Nu* values of channels with completely rough walls from inlet to outlet. In this case, average *Nu* takes slightly higher values except *Kn* = 0 cases, where reduction in local *Nu* between roughness elements is dominant. However, general trend is similar as the channel averaged cases. Rough section averaged *Nu* for various *Kn* and *Pe* values when axial conduction included and viscous dissipation neglected cases are shown graphically in Fig. (4.24), while axial conduction and viscous dissipation included cases are shown in Fig. (4.25). Also, comparison of rough section averaged *Nu* with fully developed smooth channel values when axial conduction included and viscous dissipation neglected cases are summarized in Table (4.9), and comparison of rough section averaged *Nu* with fully developed smooth channel values for axial conduction and viscous dissipation included cases are summarized in Table (4.10). Moreover, in Figs. (4.26) and (4.27), rough section averaged *Nu* for various *Kn* and *Pe* values when axial conduction and viscous dissipation neglected cases and axial conduction neglected but viscous dissipation included cases are shown graphically, respectively. Summaries of these cases are also given in Tables (4.11) and (4.12), respectively.

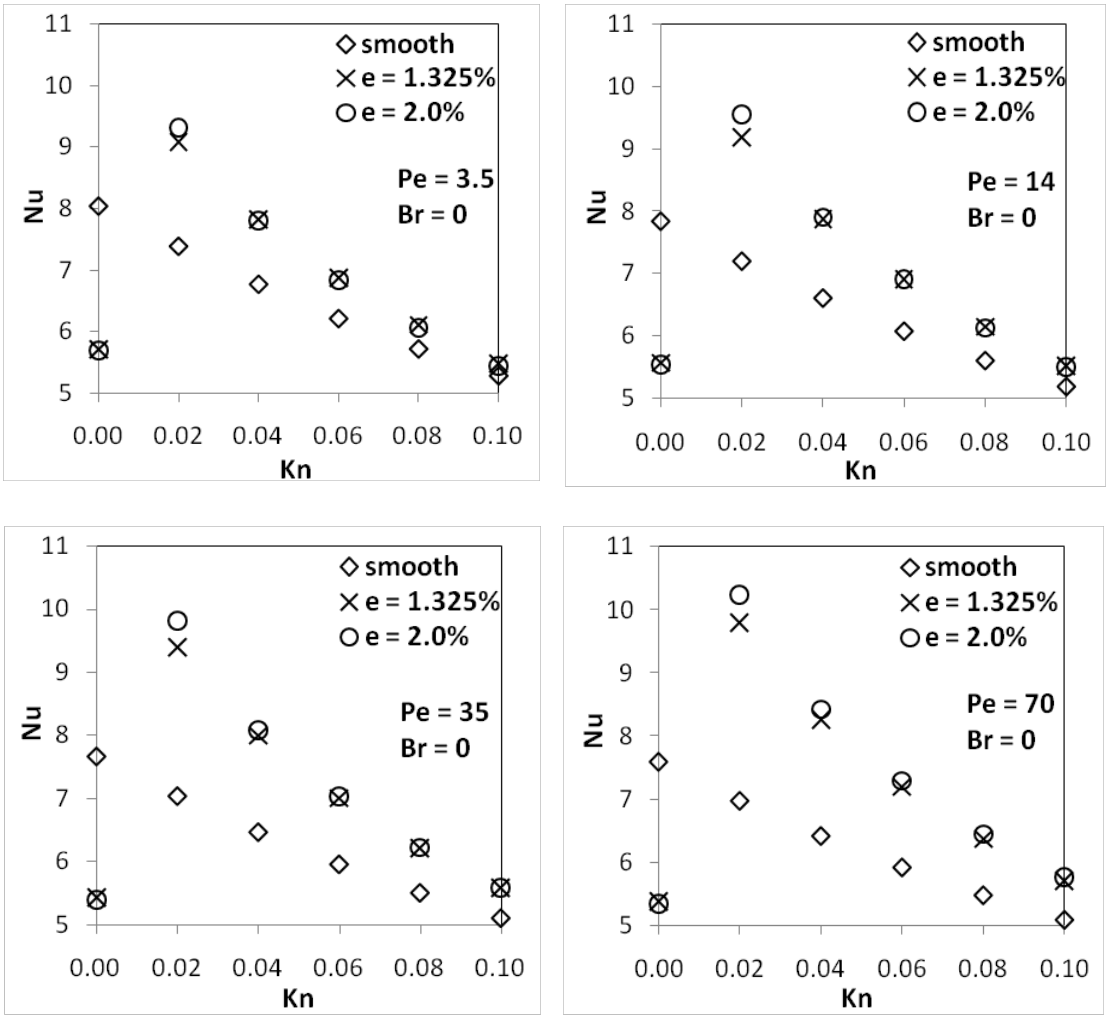


Figure 4.24: Rough section averaged *Nu* for various *Kn* and *Pe* values when axial conduction included and viscous dissipation neglected.

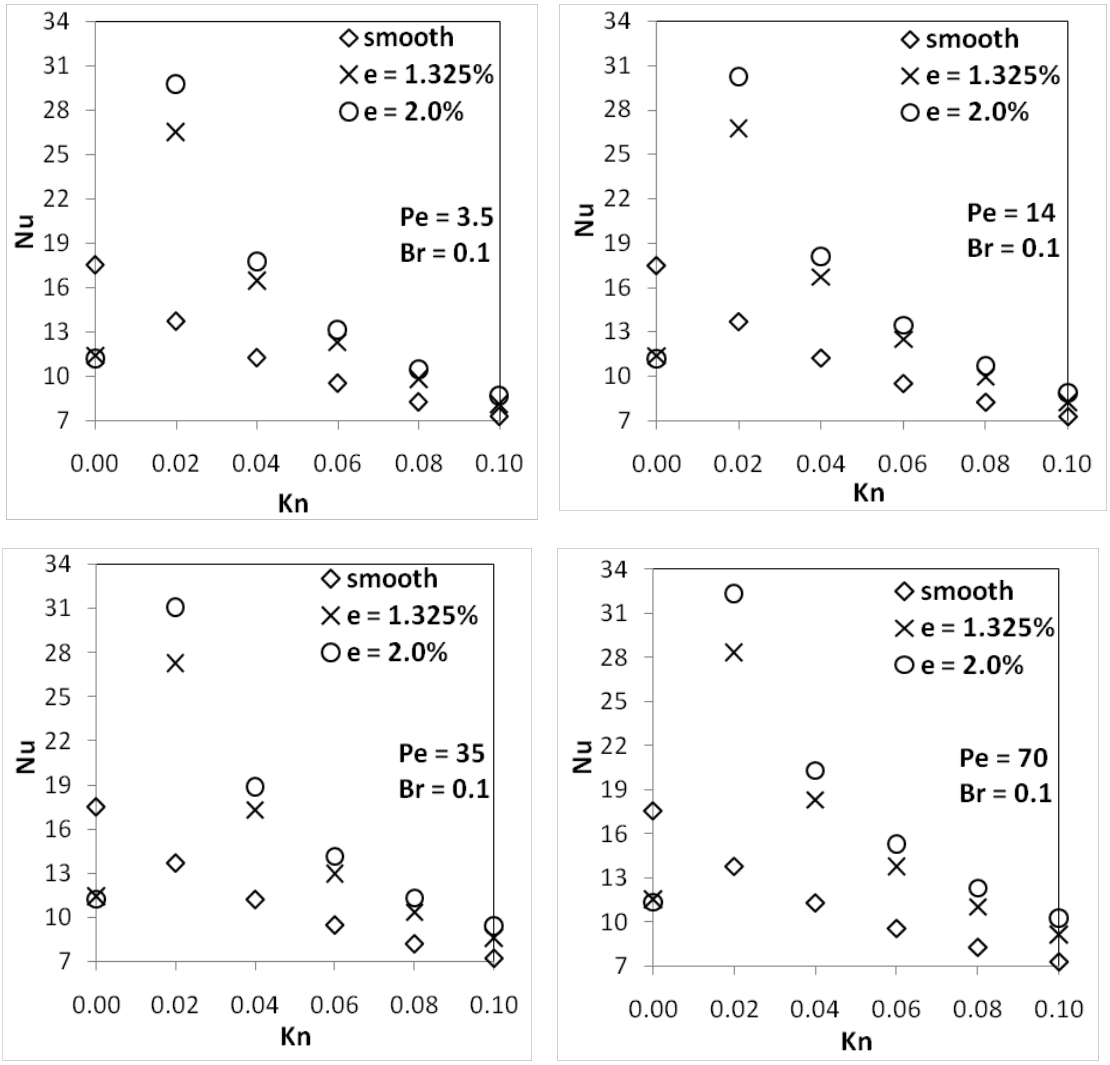


Figure 4.25: Rough section averaged *Nu* for various *Kn* and *Pe* values when axial conduction and viscous dissipation included.

Table 4.9: Rough section averaged *Nu* compared with fully developed smooth channel values when axial conduction included and viscous dissipation neglected.

| *Pe* | *Kn* | *With Axial Conduction (Br = 0)* | | | | |
|---|---|---|---|---|---|---|
| | | *Nu* | | | Difference (ε = 1.325%) | Difference (ε = 2.0%) |
| | | Smooth | Rough 1.325% | Rough 2.0% | | |
| 3.5 | 0 | 8.030 | 5.712 | 5.680 | -40.591 | -41.374 |
| | 0.02 | 7.378 | 9.082 | 9.318 | 18.767 | 20.823 |
| | 0.04 | 6.762 | 7.825 | 7.798 | 13.582 | 13.290 |
| | 0.06 | 6.206 | 6.874 | 6.824 | 9.719 | 9.059 |
| | 0.08 | 5.713 | 6.105 | 6.054 | 6.419 | 5.630 |
| | 0.10 | 5.278 | 5.474 | 5.427 | 3.583 | 2.752 |
| 7 | 0 | 7.955 | 5.654 | 5.621 | -40.703 | -41.535 |
| | 0.02 | 7.307 | 9.218 | 9.408 | 20.727 | 22.336 |
| | 0.04 | 6.701 | 7.839 | 7.833 | 14.514 | 14.452 |
| | 0.06 | 6.154 | 6.887 | 6.850 | 10.647 | 10.166 |
| | 0.08 | 5.669 | 6.119 | 6.078 | 7.361 | 6.728 |
| | 0.10 | 5.241 | 5.490 | 5.451 | 4.537 | 3.851 |
| 14 | 0 | 7.841 | 5.566 | 5.530 | -40.884 | -41.789 |
| | 0.02 | 7.200 | 9.185 | 9.546 | 21.612 | 24.577 |
| | 0.04 | 6.607 | 7.870 | 7.896 | 16.051 | 16.321 |
| | 0.06 | 6.075 | 6.914 | 6.897 | 12.129 | 11.919 |
| | 0.08 | 5.603 | 6.146 | 6.119 | 8.829 | 8.434 |
| | 0.10 | 5.186 | 5.517 | 5.490 | 5.997 | 5.533 |
| 35 | 0 | 7.668 | 5.433 | 5.394 | -41.135 | -42.162 |
| | 0.02 | 7.041 | 9.399 | 9.817 | 25.084 | 28.277 |
| | 0.04 | 6.470 | 7.994 | 8.076 | 19.067 | 19.890 |
| | 0.06 | 5.961 | 7.004 | 7.030 | 14.894 | 15.208 |
| | 0.08 | 5.509 | 6.221 | 6.228 | 11.442 | 11.548 |
| | 0.10 | 5.109 | 5.584 | 5.586 | 8.504 | 8.532 |
| 70 | 0 | 7.586 | 5.369 | 5.328 | -41.296 | -42.393 |
| | 0.02 | 6.966 | 9.804 | 10.244 | 28.948 | 32.000 |
| | 0.04 | 6.408 | 8.261 | 8.423 | 22.433 | 23.926 |
| | 0.06 | 5.909 | 7.193 | 7.289 | 17.854 | 18.933 |
| | 0.08 | 5.467 | 6.366 | 6.434 | 14.119 | 15.036 |
| | 0.10 | 5.076 | 5.702 | 5.759 | 10.983 | 11.859 |

Table 4.10: Rough section averaged *Nu* compared with fully developed smooth channel values when axial conduction and viscous dissipation included.

| *Pe* | *Kn* | *With Axial Conduction (Br = 0.1)* | | | | |
|---|---|---|---|---|---|---|
| | | *Nu* | | | Difference | Difference |
| | | Smooth | Rough 1.325% | Rough 2.0% | (ε = 1.325%) | (ε = 2.0%) |
| 3.5 | 0 | 17.484 | 11.389 | 11.175 | -53.516 | -56.454 |
| | 0.02 | 13.680 | 26.499 | 29.783 | 48.376 | 54.068 |
| | 0.04 | 11.216 | 16.450 | 17.768 | 31.818 | 36.875 |
| | 0.06 | 9.494 | 12.289 | 13.160 | 22.744 | 27.854 |
| | 0.08 | 8.225 | 9.782 | 10.466 | 15.915 | 21.406 |
| | 0.10 | 7.252 | 8.090 | 8.662 | 10.355 | 16.278 |
| 7 | 0 | 17.484 | 11.390 | 11.176 | -53.507 | -56.444 |
| | 0.02 | 13.681 | 27.058 | 29.955 | 49.440 | 54.329 |
| | 0.04 | 11.217 | 16.533 | 17.876 | 32.158 | 37.255 |
| | 0.06 | 9.495 | 12.356 | 13.254 | 23.157 | 28.361 |
| | 0.08 | 8.226 | 9.838 | 10.546 | 16.385 | 22.003 |
| | 0.10 | 7.253 | 8.138 | 8.732 | 10.875 | 16.947 |
| 14 | 0 | 17.485 | 11.396 | 11.183 | -53.438 | -56.357 |
| | 0.02 | 13.683 | 26.741 | 30.285 | 48.832 | 54.820 |
| | 0.04 | 11.219 | 16.708 | 18.114 | 32.854 | 38.065 |
| | 0.06 | 9.497 | 12.497 | 13.458 | 24.007 | 29.432 |
| | 0.08 | 8.228 | 9.955 | 10.721 | 17.353 | 23.259 |
| | 0.10 | 7.254 | 8.238 | 8.885 | 11.945 | 18.355 |
| 35 | 0 | 17.497 | 11.448 | 11.235 | -52.840 | -55.730 |
| | 0.02 | 13.701 | 27.300 | 31.144 | 49.815 | 56.008 |
| | 0.04 | 11.235 | 17.289 | 18.914 | 35.017 | 40.600 |
| | 0.06 | 9.511 | 12.970 | 14.145 | 26.667 | 32.757 |
| | 0.08 | 8.240 | 10.351 | 11.311 | 20.392 | 27.150 |
| | 0.10 | 7.264 | 8.577 | 9.399 | 15.303 | 22.711 |
| 70 | 0 | 17.547 | 11.585 | 11.384 | -51.458 | -54.132 |
| | 0.02 | 13.775 | 28.354 | 32.332 | 51.419 | 57.396 |
| | 0.04 | 11.298 | 18.330 | 20.324 | 38.363 | 44.412 |
| | 0.06 | 9.563 | 13.820 | 15.345 | 30.805 | 37.683 |
| | 0.08 | 8.280 | 11.062 | 12.340 | 25.143 | 32.898 |
| | 0.10 | 7.295 | 9.184 | 10.295 | 20.569 | 29.144 |

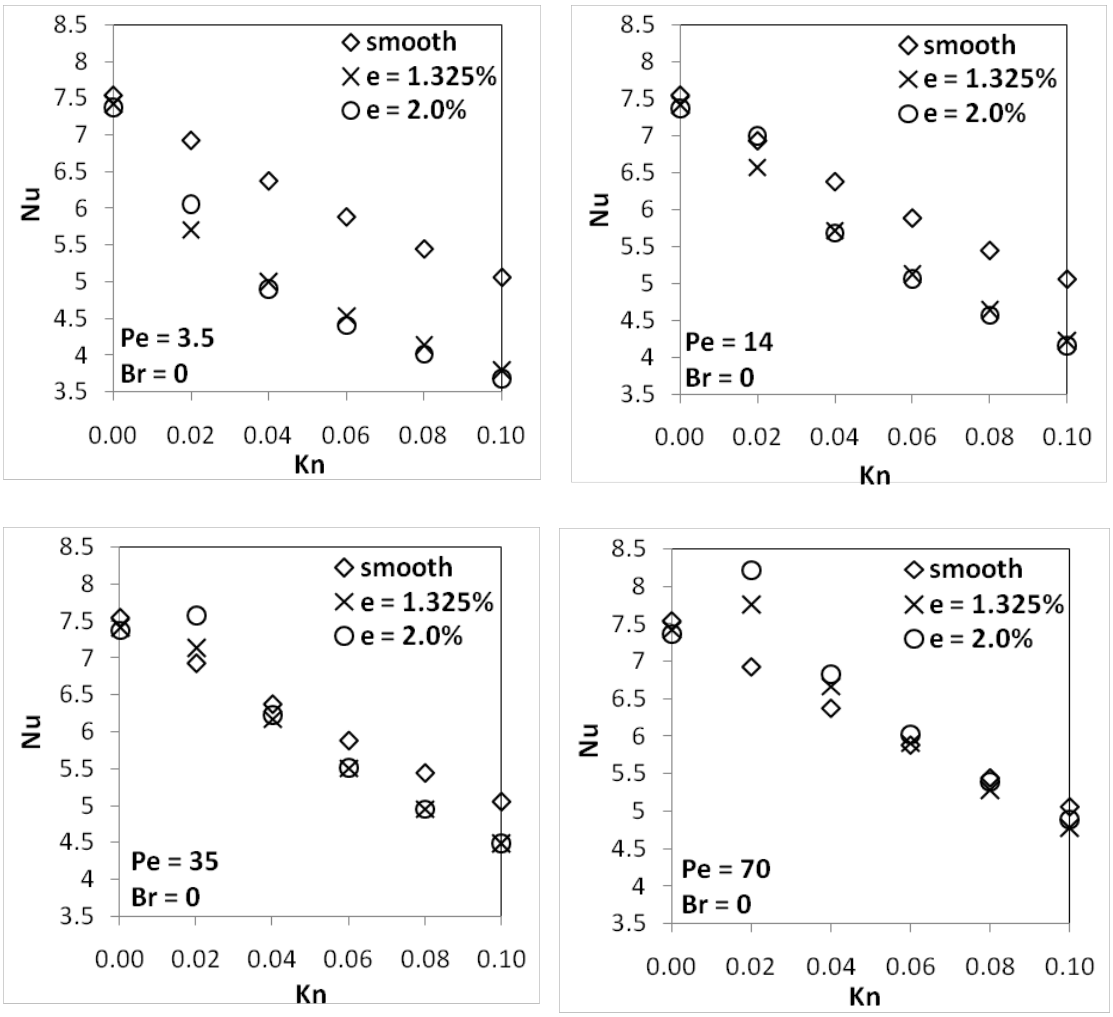


Figure 4.26: Rough section averaged *Nu* for various *Kn* and *Pe* values when axial conduction and viscous dissipation neglected.

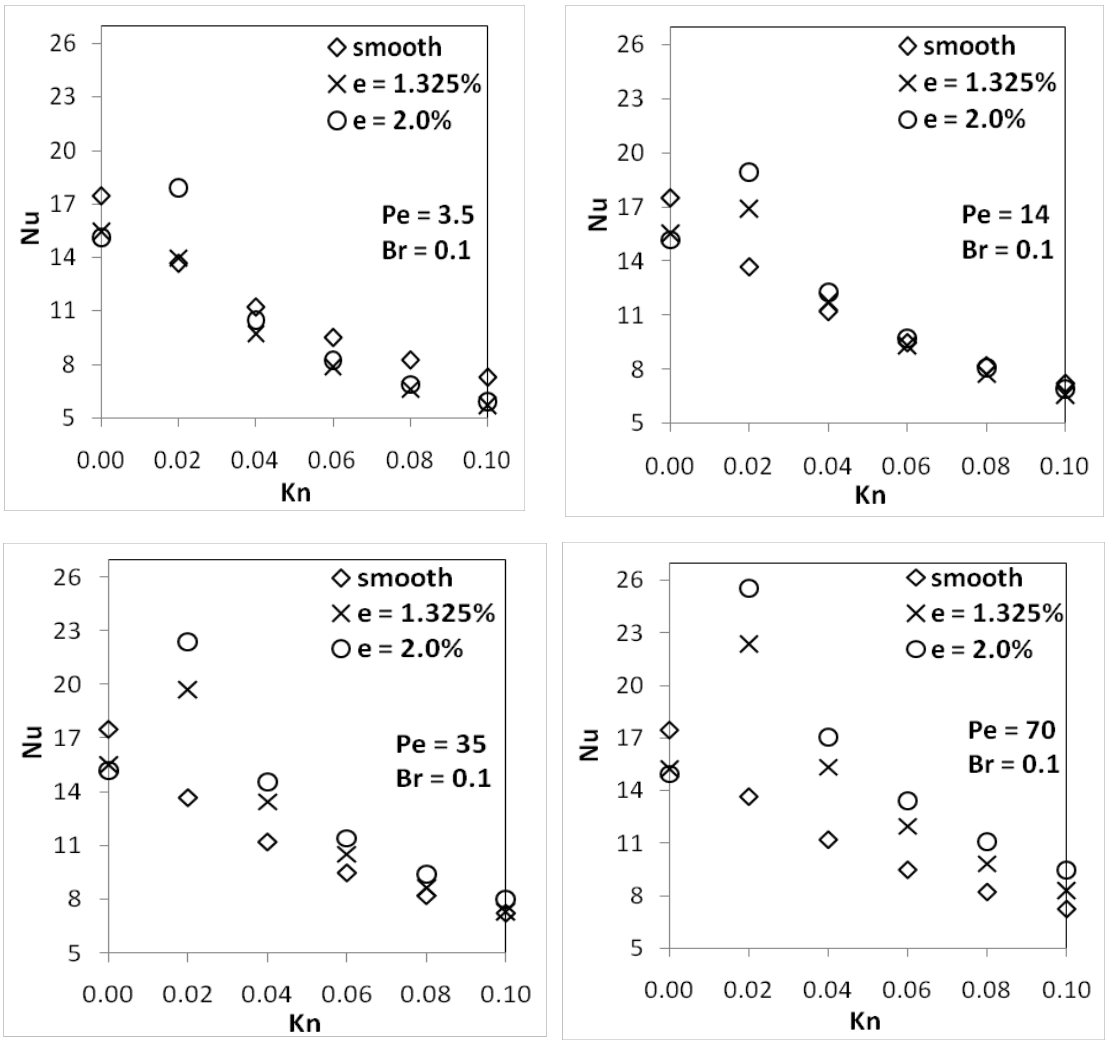


Figure 4.27: Rough section averaged *Nu* for various *Kn* and *Pe* values when axial conduction neglected and viscous dissipation included.

Table 4.11: Rough section averaged *Nu* compared with fully developed smooth channel values when axial conduction and viscous dissipation neglected.

| *Pe* | *Kn* | *Without Axial Conduction (Br = 0)* | | | | |
|---|---|---|---|---|---|---|
| | | *Nu* | | | Difference (ε = 1.325%) | Difference (ε = 2.0%) |
| | | Smooth | Rough 1.325% | Rough 2.0% | | |
| 3.5 | 0 | 7.541 | 7.421 | 7.370 | -1.617 | -2.316 |
| | 0.02 | 6.926 | 5.710 | 6.049 | -21.301 | -14.493 |
| | 0.04 | 6.374 | 5.003 | 4.904 | -27.407 | -29.986 |
| | 0.06 | 5.883 | 4.539 | 4.409 | -29.603 | -33.427 |
| | 0.08 | 5.446 | 4.144 | 4.016 | -31.433 | -35.608 |
| | 0.10 | 5.059 | 3.799 | 3.682 | -33.163 | -37.403 |
| 7 | 0 | 7.541 | 7.417 | 7.371 | -1.667 | -2.306 |
| | 0.02 | 6.926 | 6.337 | 6.519 | -9.290 | -6.247 |
| | 0.04 | 6.374 | 5.375 | 5.289 | -18.586 | -20.521 |
| | 0.06 | 5.883 | 4.849 | 4.731 | -21.333 | -24.338 |
| | 0.08 | 5.446 | 4.403 | 4.290 | -23.687 | -26.939 |
| | 0.10 | 5.059 | 4.019 | 3.918 | -25.892 | -29.135 |
| 14 | 0 | 7.541 | 7.418 | 7.372 | -1.659 | -2.290 |
| | 0.02 | 6.926 | 6.567 | 6.995 | -5.470 | 0.989 |
| | 0.04 | 6.374 | 5.708 | 5.681 | -11.666 | -12.189 |
| | 0.06 | 5.883 | 5.122 | 5.057 | -14.848 | -16.333 |
| | 0.08 | 5.446 | 4.631 | 4.564 | -17.601 | -19.319 |
| | 0.10 | 5.059 | 4.211 | 4.151 | -20.151 | -21.865 |
| 35 | 0 | 7.541 | 7.418 | 7.373 | -1.654 | -2.282 |
| | 0.02 | 6.926 | 7.138 | 7.576 | 2.973 | 8.585 |
| | 0.04 | 6.374 | 6.167 | 6.222 | -3.351 | -2.441 |
| | 0.06 | 5.883 | 5.498 | 5.511 | -7.009 | -6.757 |
| | 0.08 | 5.446 | 4.944 | 4.952 | -10.149 | -9.986 |
| | 0.10 | 5.059 | 4.477 | 4.488 | -12.989 | -12.716 |
| 70 | 0 | 7.541 | 7.416 | 7.370 | -1.688 | -2.319 |
| | 0.02 | 6.926 | 7.762 | 8.224 | 10.770 | 15.780 |
| | 0.04 | 6.374 | 6.662 | 6.831 | 4.329 | 6.692 |
| | 0.06 | 5.883 | 5.900 | 6.025 | 0.291 | 2.361 |
| | 0.08 | 5.446 | 5.283 | 5.398 | -3.085 | -0.890 |
| | 0.10 | 5.059 | 4.771 | 4.885 | -6.041 | -3.556 |

Table 4.12: Rough section averaged *Nu* compared with fully developed smooth channel values when axial conduction neglected and viscous dissipation included.

| *Pe* | *Kn* | *Without Axial Conduction (Br = 0.1)* | | | | |
|---|---|---|---|---|---|---|
| | | *Nu* | | | Difference (ε = 1.325%) | Difference (ε = 2.0%) |
| | | Smooth | Rough 1.325% | Rough 2.0% | | |
| 3.5 | 0 | 17.485 | 15.491 | 15.116 | -12.869 | -15.674 |
| | 0.02 | 13.679 | 13.989 | 17.901 | 2.218 | 23.584 |
| | 0.04 | 11.215 | 9.715 | 10.468 | -15.446 | -7.137 |
| | 0.06 | 9.493 | 7.839 | 8.208 | -21.102 | -15.656 |
| | 0.08 | 8.224 | 6.585 | 6.841 | -24.895 | -20.217 |
| | 0.10 | 7.251 | 5.666 | 5.875 | -27.972 | -23.426 |
| 7 | 0 | 17.485 | 15.495 | 15.125 | -12.844 | -15.605 |
| | 0.02 | 13.679 | 15.463 | 17.134 | 11.537 | 20.165 |
| | 0.04 | 11.215 | 10.569 | 10.930 | -6.115 | -2.610 |
| | 0.06 | 9.493 | 8.492 | 8.709 | -11.783 | -8.999 |
| | 0.08 | 8.224 | 7.096 | 7.294 | -15.891 | -12.748 |
| | 0.10 | 7.251 | 6.076 | 6.272 | -19.334 | -15.602 |
| 14 | 0 | 17.485 | 15.521 | 15.159 | -12.653 | -15.347 |
| | 0.02 | 13.679 | 16.906 | 18.925 | 19.090 | 27.719 |
| | 0.04 | 11.215 | 11.716 | 12.245 | 4.276 | 8.411 |
| | 0.06 | 9.493 | 9.298 | 9.699 | -2.096 | 2.124 |
| | 0.08 | 8.224 | 7.698 | 8.070 | -6.834 | -1.914 |
| | 0.10 | 7.251 | 6.545 | 6.899 | -10.794 | -5.101 |
| 35 | 0 | 17.485 | 15.544 | 15.201 | -12.487 | -15.028 |
| | 0.02 | 13.679 | 19.754 | 22.390 | 30.753 | 38.905 |
| | 0.04 | 11.215 | 13.474 | 14.559 | 16.766 | 22.968 |
| | 0.06 | 9.493 | 10.551 | 11.425 | 10.030 | 16.910 |
| | 0.08 | 8.224 | 8.656 | 9.436 | 4.996 | 12.844 |
| | 0.10 | 7.251 | 7.313 | 8.025 | 0.845 | 9.644 |
| 70 | 0 | 17.485 | 15.241 | 14.950 | -14.723 | -16.954 |
| | 0.02 | 13.679 | 22.379 | 25.551 | 38.875 | 46.464 |
| | 0.04 | 11.215 | 15.320 | 17.062 | 26.796 | 34.270 |
| | 0.06 | 9.493 | 11.961 | 13.418 | 20.631 | 29.250 |
| | 0.08 | 8.224 | 9.796 | 11.098 | 16.049 | 25.896 |
| | 0.10 | 7.251 | 8.268 | 9.454 | 12.298 | 23.305 |

Theoretically, as roughness heights in the channels decreases, average *Nu* values should become closer to the smooth channel values. In Table (4.13), channel averaged and rough section averaged *Nu* values are summarized for all relative roughnesses considered in this study for *Kn* = 0 and *Kn* = 0.10 when axial conduction is included. In is observed that as the relative surface roughness reduces, average *Nu* values become closer to the corresponding smooth channel values both for no-slip and slip conditions.

Table 4.13: Summary of channel and rough section averaged *Nu* for *Kn* = 0 and *Kn* = 0.10 (axial conduction included).

| | | Channel Averaged *Nu* | | | | |
|---|---|---|---|---|---|---|
| Kn | Smooth Fully Developed | ε = 0.1% | ε = 0.5% | ε = 1.325% | ε = 2.0% | ε = 10% |
| 0 | 7.586 | 7.545 | 7.327 | 7.250 | 7.223 | 6.804 |
| 0.10 | 5.076 | 5.097 | 5.418 | 5.570 | 5.606 | 5.451 |
| | | Rough Section Averaged *Nu* | | | | |
| Kn | Smooth Fully Developed | ε = 0.1% | ε = 0.5% | ε = 1.325% | ε = 2.0% | ε = 10% |
| 0 | 7.586 | 7.269 | 5.483 | 5.369 | 5.328 | 5.311 |
| 0.10 | 5.076 | 5.095 | 5.401 | 5.702 | 5.759 | 5.450 |

# CHAPTER – 5

# SUMMARY, CONCLUSIONS, AND SUGGESTIONS FOR FUTURE WORK

In this study the effect of roughness on convective heat transfer and fluid flow in microchannels with uniform inlet fluid velocity and constant wall temperature boundary condition is investigated. For this purpose, single-phase, incompressible, laminar and constant property fluid flow between parallel plates at steady state and in the slip-flow regime is considered.

Roughness effect is simulated by adding triangular obstructions along the channel wall. Since the flow is in the slip-flow regime, the Navier-Stokes and energy equations are solved numerically by imposing velocity slip and temperature jump to boundary conditions. Also, since the fluid is assumed to have constant thermo-physical properties, Navier-Stokes and energy equations are decoupled. Therefore, Navier-Stokes equations are first solved along the channel, and then the velocities found are used in the energy equation to obtain the temperature profile and local Nusselt numbers along the channel. Numerical calculations are carried out both by taking the axial conduction and the viscous dissipation effects into account, and by neglecting their effects. Reduced integration penalty FEM is used as the numerical method for the hydraulic part and standard Galerkin FEM for the energy part of the problem. The computer code is written in MATLAB by the author. The written code is verified by comparing the results obtained from analytical solutions for simplified smooth channel cases.

Air is used as the working fluid where $Pr$ = 0.7. Calculations are carried out for $Re$ values of 5, 10, 20, 50, and 100 which yields $Pe$ values of 3.5, 7, 14, 35, and 70. $Kn$ range from 0.0 to 0.10, and considered $Br$ values are -0.1, 0.0, and 0.1. Roughness is considered as triangular shape geometrical obstructions placed over the bottom plate of smooth channel and investigated relative roughness values are 1.325%, 2.0%, and 2.65%.

Under the specified assumptions, following general conclusions can be obtained from this study.

For the smooth case,

1) Rarefaction decreases the velocity gradient at the wall which will reduce the friction factor.
2) As $Kn$ increases, local and fully developed $Nu$ decreases compared to the continuum case.
3) Axial conduction plays an important role especially at low $Pe$ and at the inlet section, and should not be neglected for slow flows.
4) In the presence of viscous heating, there is significant increase in fully developed $Nu$ values. Due to high length to diameter ratio of microchannels, viscous heating should be considered in the analysis.

For the rough case,

1) When rarefaction effect is neglected, presence of surface roughness decreases the $Nu$ compared to smooth channel fully developed values. Magnitude of the decrease depends on the flow parameters and the effects included such as axial conduction and viscous dissipation. However, decrease in magnitude increase slightly with increasing relative roughness.

2) As *Kn* increases, increase in *Nu* is observed with respect to corresponding smooth channel value. However the increase reduces as the rarefaction increases.
3) Magnitude of the relative roughness affects the overall *Nu* values more at low *Kn* values in the considered relative roughness values.
4) In the presence of viscous dissipation, *Nu* increases similar to the smooth case and this increase is more in high relative roughness.
5) Increase in *Pe* increases the maximum value of local *Nu* at low *Kn*, however there is not any significant difference at high *Kn*.
6) When axial conduction term is neglected, surface roughness tends to decrease the average *Nu* at low *Pe* values, except low *Kn*.
7) Surface roughness is found to be more effective at relatively low rarefied flows.

Surface roughness properties of microchannels in a micro-flow device, such as a micro heat exchanger or a micro heat sink, depend on the manufacturing processes of these channels, as well as the materials used; such as silicon, steel, or copper. Most commonly and widely used method is the photolithographic process. This method is mostly related to the silicon wafers and cross-sections of the channels that can be obtained by this method are limited to the crystallographic morphology of the silicon used. These cross-sections are rectangular, triangular, and trapezoidal. Among the others, silicon microchannels with trapezoidal cross-sections are preferred more due to ease of production. In the photolithographic process, surface roughness also depends on the concentration and temperature of the etching solution, and the duration that the solution is applied in addition to the crystallographic morphology of the silicon used. In widely used trapezoidal channels, roughness occurs at the base of the channel rather than at the side walls, and they resemble conical or triangular prisms because of the morphology of the silicon.

Cases considered in this study showed that effect of surface roughness on heat transfer is more obvious at low rarefied flow between parallel plates. Similar simulations should also be repeated with different channel geometries such as circular, rectangular, triangular or trapezoidal cross-sections to verify this general result found for parallel plates. Thus, surface roughness could be considered and used in real micro applications. If the purpose is heat transfer enhancement in micro applications such as in micro heat exchanger or heat sink composed of trapezoidal silicon microchannels, the goal can be achieved by arranging the flow in the channel to a low rarefied state since surface roughness is inevitable (due to the production method). In this study, an optimum value of $Kn$ = 0.02 is determined for maximum heat transfer, among the considered $Kn$ value. However, it should be kept in mind that lower $Kn$ values, which are beyond the scope of this study, could increase heat transfer more.

It is known from the literature that, geometrical properties of channels and roughness elements in such numerical simulations yields different results. Also, there is very little numerical data about roughness effect on heat transfer in microchannels, especially with rarefaction effect, compared to other subjects. Thus, various simulations should be done with different geometries and different conditions to clarify the roughness effect and to construct a database regarding roughness effect. It should also be noted that, such two dimensional simulations should yield overestimated results. Thus three-dimensional simulations are needed and should give more accurate results.

It is also known from literature that, surface roughness causes high pressure drop in microchannels. When high pressure drop is combined with large length to diameter ratio, compressibility effect becomes important. Thus, this work can be expanded by taking compressibility into account. Moreover, other important

factors such as; temperature dependent fluid properties, conduction at solid boundaries, and different boundary conditions such as constant heat flux or varying temperature profile at solid boundaries, can be investigated together with surface roughness.

# REFERENCES


[1] Mohamed Gad-el-Hak, Edit., The MEMS Handbook: Introduction and Fundamentals, 2nd Ed., Taylor & Francis, 2005.

[2] George Karniadakis, Ali Beskok, Narayan Aluru, Microflows and Nanoflows, Fundamentals and Simulation, Springer, 2005.

[3] Sergey Edward Lyshevski, Nano- and Micro-Electromechanical Systems, Fundamentals of Nano- and Microengineering, 2nd Ed., CRC Press, 2004.

[4] Richard P. Feynman, There's plenty of room at the bottom, Journal of Microelectromechanical Systems, Vol. 1, No. 1, March 1992.

[5] Richard P. Feynman, Infinitesimal machinery, Journal of Microelectromechanical Systems, Vol. 2, No. 1, March 1993.

[6] Çetin, B., Analysis of single phase convective heat transfer in microtubes and microchannels, M.Sc. Thesis, METU, 2005.

[7] Zhuomin M. Zhang, Nano / Microscale Heat Transfer, McGraw-Hill, 2007.

[8] G.L.Morini, Single-phase convective heat transfer in microchannels: a review of experimental results, International Journal of Thermal Sciences 43 (2004) 631-651.

[9] Y.Yener, S.Kakac, M.Avelino, and T.Okutucu, Single-phase forced convection in microchannels – A State-of-the-art-review, in: S.Kakac, L.Vasiliev, Y.Bayazitoglu, Y.Yener (Edits), Microscale Heat Transfer-Fundamentals and Applications in Biological Systems and MEMS, Kluwer Academic Publishers, The Netherlands, 2005.

[10] Y.Bayazitoglu, and S.Kakac, Flow regimes in microchannel single-phase gaseous fluid flow, in: S.Kakac, L.Vasiliev, Y.Bayazitoglu, Y.Yener (Edits), Microscale Heat Transfer-Fundamentals and Applications in Biological Systems and MEMS, Kluwer Academic Publishers, The Netherlands, 2005.

[11] Y.Bayazitoglu, G.Tunc, K.Wilson, and I.Tjahjono, Convective heat transfer for single-phase gases in microchannel slip-flow: Analytical solutions, in: S.Kakac, L.Vasiliev, Y.Bayazitoglu, Y.Yener (Edits), Microscale Heat Transfer-Fundamentals and Applications in Biological Systems and MEMS, Kluwer Academic Publishers, The Netherlands, 2005.

[12] N.T.Obot, Toward a better understanding of friction and heat/mass transfer in microchannels–A literature review, Microscale Thermophysical Engineering 6 (2002) 155-173.

[13] C.B.Sobhan, and S.V.Garimella, A comparative analysis of studies on heat transfer and fluid flow in microchannels, Microscale Thermophysical Engineering 5 (2001) 293-311.

[14] G.Hetsroni, A.Mosyak, E.Pogrebnyak, and L.P.Yarin, Fluid flow in micro-channels, International Journal of Heat and Mass Transfer 48 (2005) 1982-1998.

[15] G.Hetsroni, A.Mosyak, E.Pogrebnyak, and L.P.Yarin, Heat transfer in micro-channels: Comparison of experiments with theory and numerical results, International Journal of Heat and Mass Transfer 48 (2005) 5580-5601.

[16] H.P.Kavehpour, M.Faghri, and Y.Asako, Effects of compressibility and rarefaction on gaseous flows in microchannels, Numerical Heat Transfer, Part A, 32 (1997) 677-696.

[17] N.G.Hadjiconstantinou, and O.Simek, Nusselt number in micro and nano channels under conditions of constant wall temperature, Proceedings of IMECE 2001, November 11-16, 2001, New York, NY.

[18] N.G.Hadjiconstantinou, and O.Simek, Constant-wall-temperature Nusselt number in micro and nano-channels, Transactions of the ASME, vol. 124, April, 2002.

[19] O.Aydin, and M.Avci, Analysis of laminar heat transfer in micro-Poiseuille flow, International Journal of Thermal Sciences 46 (2007) 30-37.

[20] Y.Asako, T.Pi, S.E.Turner, and M.Faghri, Effect of compressibility on gaseous flows in micro-channels, International Journal of Heat and Mass Transfer 46 (2003) 3041-3050.

[21] H-E.Jeong, and J-T.Jeong, Extended Graetz problem including streamwise conduction and viscous dissipation in microchannel, International Journal of Heat and Mass Transfer 49 (2006) 2151-2157.

[22] G.Tunc, and Y.Bayazitoglu, Heat transfer in microtubes with viscous dissipation, International Journal of Heat and Mass Transfer 44 (2001) 2395-2403.

[23] F.E.Larrodé, C.Housiadas, and Y.Drossinos, Slip-flow heat transfer in circular tubes, International Journal of Heat and Mass Transfer 43 (2000) 2669-2680.

[24] B.Cetin, H.Yuncu, and S.Kakac, Gaseous flow in microconduits with viscous dissipation, International Journal of Transport Phenomena 8 (2006) 297-315.

[25] B.Cetin, A.G.Yazicioglu, and S.Kakac, Fluid flow in microtubes with axial conduction including rarefaction and viscous dissipation, International Communications in Heat and Mass Transfer 35 (2008) 535-544.

[26] W.Sun, S.Kakac, and A.G.Yazicioglu, A numerical study of single-phase convective heat transfer in microtubes for slip flow, International Journal of Thermal Sciences 46 (2007) 1084-1094.

[27] O.Aydin, and M.Avci, Heat and fluid flow characteristics of gases in micropipes, International Journal of Heat and Mass Transfer 49 (2006) 1723-1730.

[28] J.Koo, and C.Kleinstreuer, Viscous dissipation effects in microtubes and microchannels, International Journal of Heat and Mass Transfer 47 (2004) 3159-3169.

[29] S.Yu, and A.Ameel, Slip-flow heat transfer in rectangular microchannels, International Journal of Heat and Mass Transfer 44 (2001) 4225-4234.

[30] G.Tunc, and Y.Bayazitoglu, Heat transfer in rectangular microchannels, International Journal of Heat and Mass Transfer 45 (2002) 765-773.

[31] S-S.Hsieh, H-H.Tsai, C-Y.Lin,C-F.Huang, and C-M.Chien, Gas flow in a long microchannel, International Journal of Heat and Mass Transfer 47 (2004) 3877-3887.

[32] P-S.Lee, S.V.Garimella, and D.Liu, Investigation of heat transfer in rectangular microchannels, International Journal of Heat and Mass Transfer 48 (2005) 1688-1704.

[33] M.Renksizbulut, H.Niazmand, and G.Tercan, Slip-flow and heat transfer in rectangular microchannels with constant wall temperature, International Journal of Thermal Sciences 45 (2006) 870-881.

[34] G.L.Morini, M.Spiga, and P.Tartarini, The rarefaction effect on the friction factor of gas flow in microchannels, Superlattices and Microstructures 35 (2004) 587-599.

[35] B.Cao, G.W.Chen, and Q.Yuan, Fully developed laminar flow and heat transfer in smooth trapezoidal microchannel, International Communications in Heat and Mass Transfer 32 (2005) 1211-1220.

[36] L.Kuddusi, and E.Çetegen, Thermal and hydrodynamic analysis of gaseous flow in trapezoidal silicon microchannels, International Journal of Thermal Sciences 48 (2009) 353-362.

[37] R.W.Barber, Y.Sun, X.J.Gu, and D.R.Emerson, Isothermal slip flow over curved surfaces, Vacuum 76 (2004) 73-81.

[38] N.Dongari, A.Agrawal, and A.Agrawal, Analytical solution of gaseous slip flow in long microchannels, International Journal of Heat and Mass Transfer 50 (2007) 3411-3421.

[39] Gh.M.Mala, and D.Li, Flow characteristics of water in microtubes, International Journal of Heat and Fluid Flow 20 (1999) 142-148.

[40] W.Qu, Gh.M.Mala, and D.Li, Pressure-driven water flows in trapezoidal silicon microchannels, International Journal of Heat and Mass Transfer 43 (2000) 353-364.

[41] W.Qu, Gh.M.Mala, and D.Li, Heat transfer for water flow in trapezoidal silicon microchannels, International Journal of Heat and Mass Transfer 43 (2000) 3925-3936.

[42] S.G.Kandlikar, S.Joshi, and S.Tian, Effect of surface roughness on heat transfer and fluid flow characteristics at low Reynolds numbers in small diameter tubes, Heat Transfer Engineering 24(3) (2003) 4-16.

[43] H.Sun, and M.Faghri, Effect of surface roughness on nitrogen flow in a microchannel using the direct simulation Monte Carlo method, Numerical Heat Transfer, Part A 43 (2003) 1-8.

[44] Y.Hu, C.Werner, and D.Li, Influence of three-dimensional roughness on pressure-driven flow through microchannels, Journal of Fluids Engineering, Vol. 125 (2003) 871-879.

[45] R.Baviére, G.Gamrat, M.Favre-Marinet, and S.L.Person, Modeling of laminar flows in rough-wall microchannels, Journal of Fluids Engineering, Vol. 128 (2006) 734-741.

[46] H.Y.Wu, and P.Cheng, An experimental study of convective heat transfer in silicon microchannels with different surface conditions, International Journal of Heat and Mass Transfer 46 (2003) 2547-2556.

[47] C.Kleinstreuer, and J.Koo, Computational analysis of wall roughness effect for liquid flow in micro-conduits, Journal of Fluids Engineering, Vol. 126 (2004) 1-9.

[48] J.Koo, and C. Kleinstreuer, Analysis of surface roughness effects on heat transfer in micro-conduits, International Journal of Heat and Mass Transfer 48 (2005) 2625-2634.

[49] S.E.Turner, L.C.Lam, M.Faghri, and O.J.Gregory, Experimental investigation of gas flow in microchannels, Journal of Heat Transfer, Vol. 126 (2004) 753-761.

[50] G.Croce, P.D'Agaro, Numerical analysis of roughness effect on microtube heat transfer, Superlattices and Microstructures 35 (2004) 601-616.

[51] G.Croce, P.D'Agaro, Numerical simulation of roughness effect on microchannel heat transfer and pressure drop in laminar flow, Journal of Physics D: Applied Physics 38 (2005) 1518-1530.

[52] H.Wang, Y.Wang, and J.Zhang, Influence of ribbon structure rough wall on the microscale Poiseuille flow, Journal of Fluids Engineering, Vol. 127 (2005) 1140-1145.

[53] S.G.Kandlikar, D.Schmitt, A.L.Carrano, J.B.Taylor, Characterization of surface roughness effects on pressure drop in single-phase flow in minichannels, Physics of Fluids 17, 100606 (2005) 1-11.

[54] J.B.Taylor, A.L.Carrano, S.G.Kandlikar, Characterization of the effect of surface roughness and texture on fluid flow – past, present, and future, International Journal of Thermal Sciences 45 (2006) 962-968.

[55] G.P.Celata, M.Cumo, S.McPhail, and G.Zummo, Characterization of fluid dynamic behavior and channel wall effects in microtube, International Journal of Heat and Fluid Flow 27 (2006) 135-143.

[56] A.S.Rawool, S.K.Mitra, and S.G.Kandlikar, Numerical simulation of flow through microchannels with designed roughness, Microfluid Nanofluid 2 (2006) 215-221.

[57] S.Shen, J.L.Xu, J.J.Zhou, and Y.Chen, Flow and heat transfer in microchannels with rough wall surface, Energy Conversion and Management 47 (2006) 1311-1325.

[58] Y.Ji, K.Yuan, and J.N.Chung, Numerical simulation of wall roughness on gaseous flow and heat transfer in a microchannel, International Journal of Heat and Mass Transfer 49 (2006) 1329-1339.

[59] B-Y.Cao, M.Chen, and Z-Y.Guo, Effect of surface roughness on gas flow in microchannels by molecular dynamics simulation, International Journal of Engineering Science 44 (2006) 927-937.

[60] G.H.Tang, Z.Li, Y.L.He, and W.Q.Tao, Experimental study of compressibility, roughness and rarefaction influences on microchannel flow, International Journal of Heat and Mass Transfer 50 (2007) 2282-2295.

[61] H.Wang, and Y.Wang, Influence of three-dimensional wall roughness on the laminar flow in microtube, International Journal of Heat and Fluid Flow 28 (2007) 220-228.

[62] H.Wang, and Y.Wang, Flow in microchannels with rough walls: flow pattern and pressure drop, Journal of Micromechanics and Microengineering 17 (2007) 586-596.

[63] G.Croce, P.D'Agaro, and C.Nonini, Three-dimensional roughness effect on microchannel heat transfer and pressure drop, International Journal of Heat and Mass Transfer 50 (2007) 5249-5259.

[64] G.Croce, P.D'Agaro, and A.Filippo, Compressibility and rarefaction effects on pressure drop in rough microchannels, Heat Transfer Engineering 28(8-9) (2007) 688-695.

[65] J.N.Reddy, An Introduction to the Finite Element Method, 3rd Ed., McGraw-Hill, 2006.

[66] J.N.Reddy, and D.K.Gartling, The Finite Element Method in Heat Transfer and Fluid Dynamics, 2nd Ed., CRC Press, 2000.

[67] I.M.Smith, and D.V.Griffiths, Programming the Finite Element Method, 3rd Ed., John Wiley&Sons, 1998.

[68] B.Bulut, B.Çetin, A.G.Yazıcıoğlu, S.Kakaç, and H.Yüncü, Mikrokanallar ve Mikrotüplerde Tek Fazlı Isı Akışında Eksenel Isı İletimi Etkisinin Analizi, ULIBTK'07 16.Ulusal Isı Bilimi ve Tekniği Kongresi, 30 Mayıs – 2 Haziran 2007, Kayseri.

[69] University of Missouri Electron Microscopy Core Facility, Training, Courses-Student Projects, Scanning Electron Microscope (SEM) View of Silicon Microchannels, Rosalynn M.Manor, www.emc.missouri.edu/Manor.htm, 01.12.2008.

[70] R. D. Present, Kinetic Theory of Gases, McGraw-Hill Book Company, Inc., 1958.